

NASA CR-174,838

NASA Contractor Report 174838

NASA-CR-174838
19850007419

The Structure of Dilute Combusting Sprays

J.-S. Shuen, A.S.P. Solomon, and G.M. Faeth

The Pennsylvania State University
University Park, Pennsylvania

January 1985

LIBRARY COPY

SEP 20 1985

LANGLEY RESEARCH CENTER
LIBRARY, NASA
HAMPTON, VIRGINIA

Prepared for

NATIONAL AERONAUTICS AND SPACE ADMINISTRATION
Lewis Research Center
Under Grant NAG 3-190

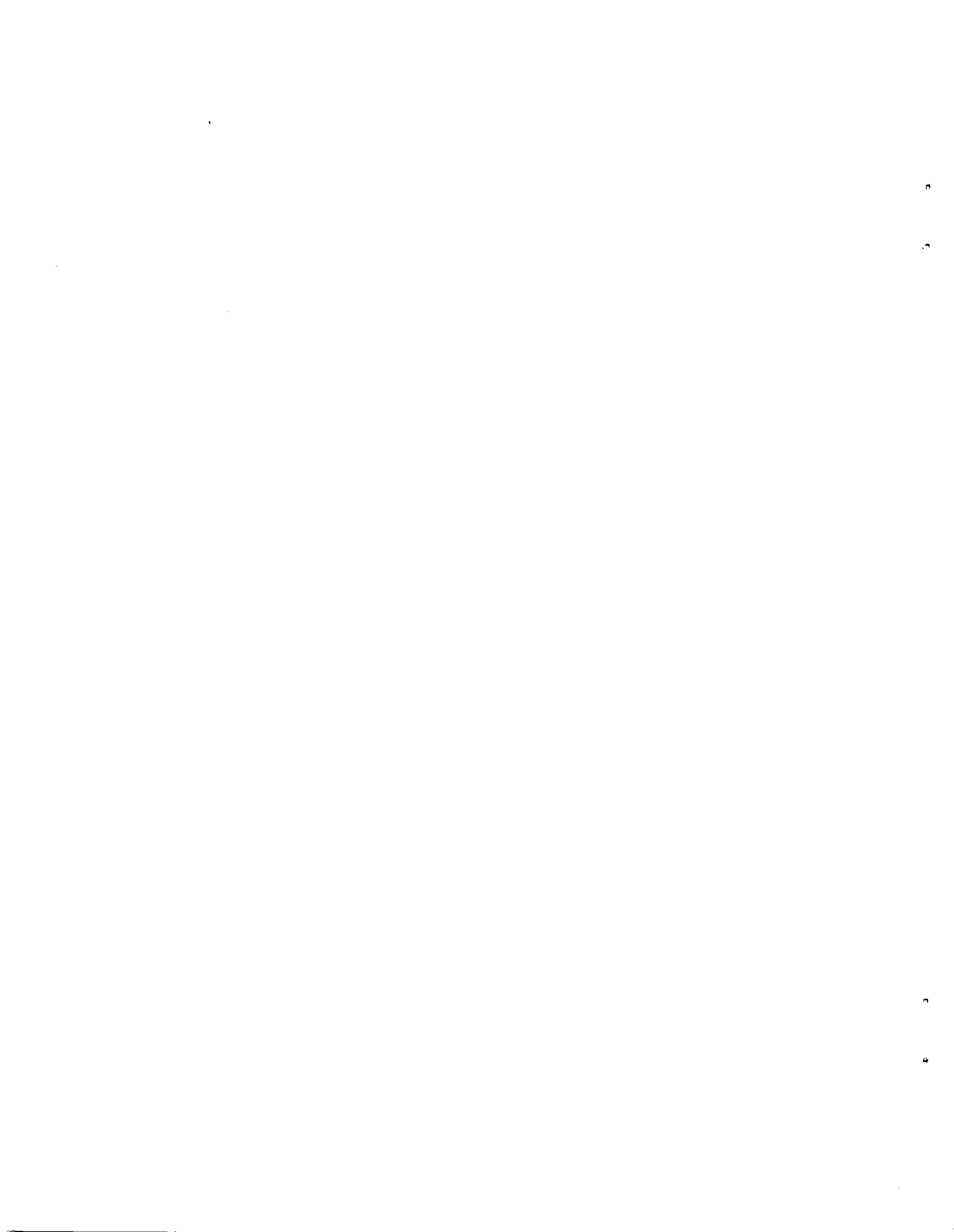


TABLE OF CONTENTS

	<u>Page</u>
NOMENCLATURE.	iii
SUMMARY	1
1. INTRODUCTION.	2
2. EXPERIMENTAL METHODS.	4
2.1 Test Arrangement	4
2.2 Test Conditions.	7
2.3 Instrumentation.	10
2.3.1 Gas Velocity.	10
2.3.2 Drop Velocity	10
2.3.3 Drop-Size Distributions	12
2.3.4 Drop Number Flux.	14
2.3.5 Mean Gas Temperature.	14
3. THEORY.	18
3.1 General Description.	18
3.2 Continuous-Phase Analysis.	18
3.2.1 Governing Equations	18
3.2.2 State Relationships	22
3.2.3 Computations.	26
3.3 Drop Transport	26
3.3.1 Drop Transport Analysis	26
3.3.2 Drop Transport Calibrations	32
3.4 Deterministic Separated Flow Model	35
3.5 Stochastic Separated Flow Model.	36
4. RESULTS AND DISCUSSION.	38
4.1 Introduction	38
4.2 Initial Conditions	39
4.3 Scalar Structure of the Test Flame	39
4.4 Structure of the Spray Flames.	47
4.4.1 Mean Phase Velocities	47
4.4.2 Fluctuating Phase Velocities.	52
4.4.3 Drop Number Flux.	54
4.4.4 Drop-Size Distributions	61
5. SUMMARY AND CONCLUSIONS	61
5.1 Summary.	61
5.2 Conclusions.	64
APPENDIX A: EXPERIMENTAL UNCERTAINTIES	66
A.1 Phase Velocities	66
A.2 Drop-Size Distribution	69
A.3 Drop Number Fluxes	71
A.4 Mean Gas Temperatures.	72

APPENDIX B: DROP NUMBER FLUX MEASUREMENTS.	74
B.1 Pulse Counter.	74
B.2 Calibration of Measuring Area.	74
APPENDIX C: CORRECTION OF TEMPERATURE MEASUREMENTS FOR RADIATION.	77
APPENDIX D: DROP TRANSPORT PROPERTIES.	79
D.1 Mixture Thermal Conductivity	79
D.2 Mixture Viscosity.	79
D.3 Mixture Mass Diffusivity	79
D.4 Mixture Specific Heat.	80
D.5 Properties of Methanol	80
APPENDIX E: DROP TRANSPORT CALIBRATION	83
E.1 Experimental Method.	83
E.2 Drop-Life-History Data	86
APPENDIX F: FLAME STRUCTURE DATA	87
F.1 Mean Gas Temperatures.	87
F.2 Gas Velocities	90
F.3 Drop Velocities.	95
F.4 Drop Number Fluxes	105
F.5 Drop Size Distributions.	109
REFERENCES.	113

NOMENCLATURE

<u>Symbol</u>	<u>Description</u>
a	acceleration of gravity
A	total surface area of drops in a sample
A_F	cross-sectional area of drop number flux measuring volume
B_0, B_y	mass transfer driving potentials, Eqs. (3.20) and (3.21)
C_D	drag coefficient
C_i	parameters in turbulence model
C_p	specific heat at constant pressure
d	injector diameter
d_i	diameter of i'th drop
d_k	$k = 1, 2, \text{ etc.}$, moments of drop-size distribution, Eq. (A.10)
d_p	drop diameter
d_{tc}	diameter of thermocouple junction
D	mean mass diffusivity
D_{ij}	binary diffusivity
e	fluctuating signal amplitude
E	signal amplitude
f	mixture fraction
g	square of mixture fraction fluctuations
h	heat transfer coefficient
h_i	enthalpy of species i
h_{fg}	enthalpy of vaporization
h_{fgT}	total enthalpy of gasification, Eq. (3.27)
k	turbulence kinetic energy
k'	Boltzman constant, Appendix D
K	LDA calibration factor, Eq. (A.5)
ℓ	half-width of LDA measuring volume
L	distance between drop generator and burner exit, length of drop number flux measuring volume
L_e	dissipation length scale
m	drop mass
\dot{m}	mass flow rate
\dot{m}''	mass flux at drop surface
M_i, M	molecular weight of species i, of mixture
n	number of drop groups, total number of drops sampled
\dot{n}	total drop count rate
\dot{n}_i	number of drops per unit time in group i
\dot{n}''	drop number flux
N_p, N_S	convection correction, Eq. (3.24)
p	pressure
p_v	vapor pressure
$P(f), \bar{P}(f)$	time- and Favre-averaged probability density function of f
PDF	probability density function
Pr	Prandtl number
Q_r	lower heat of reaction per mass of oxygen
r	radial distance
R	ideal gas constant
Re	Reynolds number

Sc	Schmidt number
S_ϕ	source term
SMD	Sauter mean diameter
t	time
t_e	eddy lifetime
T	temperature
T_{cr}	critical temperature
T_r	reference state
u	axial velocity
u_p	drop velocity vector
v	radial velocity
v_i	generic quantity, Appendix A
V	generic function, Appendix A; total drop volume in a sample
V_j	volume of computational cell j
w	tangential velocity
W	width of drop number flux measuring volume
x	axial distance
x_p	drop position vector
X_i	mole fraction of species i
Y_i	mass fraction of species i
α	average property factor, Eq. (3.28)
Δx_p	path length of drops in an eddy
Δt	residence time of drops in an eddy
ϵ	rate of dissipation of turbulence kinetic energy, gray-body emissivity
ϵ'	characteristic molecular energy, Appendix D
λ	thermal conductivity
μ	laminar viscosity, location of maximum probability
μ_t	turbulent viscosity
ν	kinematic viscosity
ν_{FO}	stoichiometric mass of fuel per mass of oxygen
ρ	density
σ	standard deviation of PDF, Stephan-Boltzman constant
σ'	characteristic molecular length, Appendix D
σ_{dp}	standard deviation of drop-size distribution
σ_i	turbulent Prandtl/Schmidt number
ϕ	generic quantity, fuel-equivalence ratio
ϕ_c	critical fuel-equivalence ratio
ϕ_{ij}	property interaction parameter, Appendix D

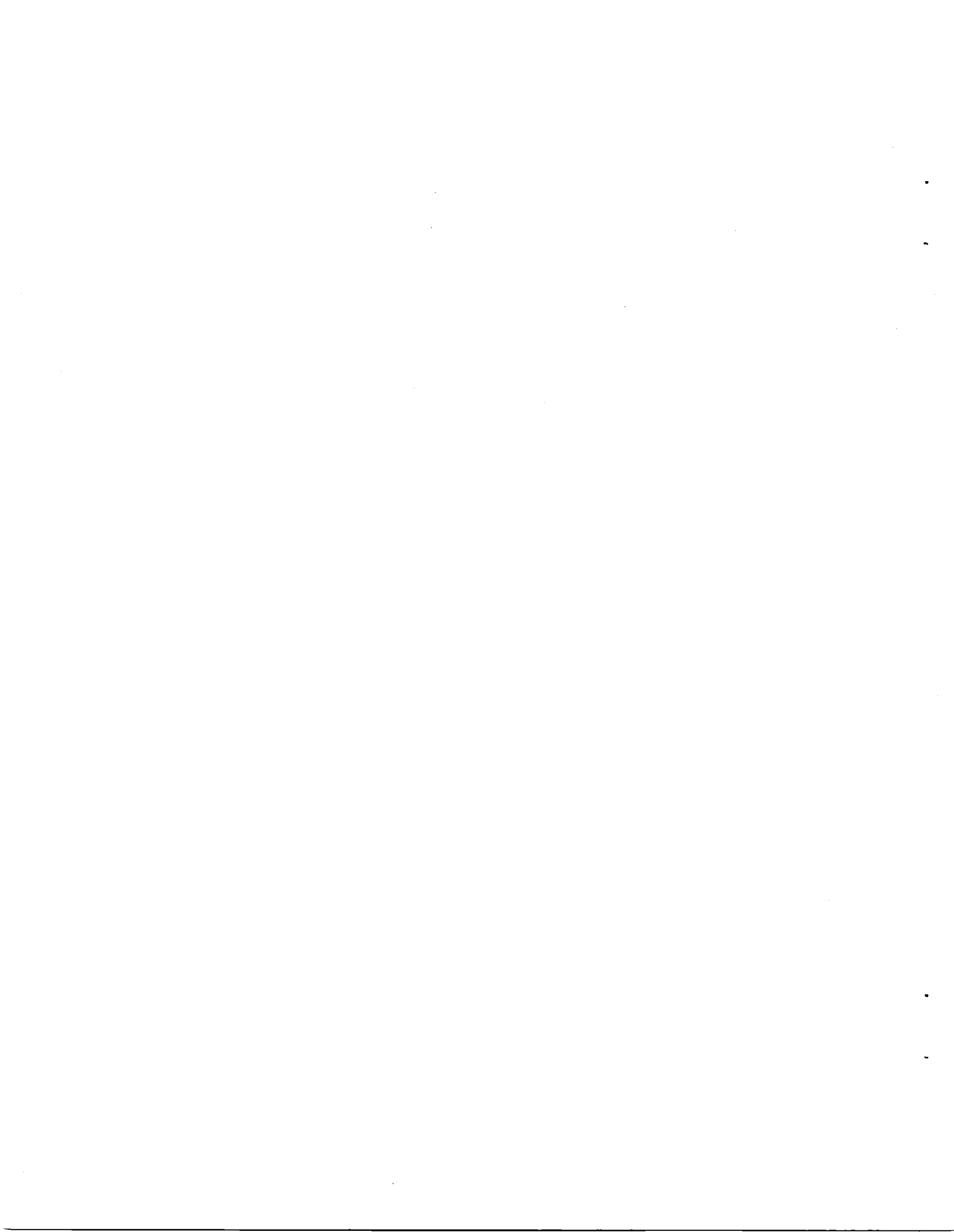
Subscripts

a	air
avg	average value
bf	bulk liquid
c	centerline quantity
f	flame property, reference property
F	fuel
g	gas-phase property
i	drop group or coordinate direction
o	burner exit condition

p drop property
s drop surface condition
t measured value of a property
tc thermocouple
∞ ambient condition

Superscripts

($\bar{\quad}$) time-averaged quantity
($\bar{\quad}$)' time-averaged fluctuating quantity
($\tilde{\quad}$) Favre-averaged quantity
($\tilde{\quad}$)" Favre-averaged fluctuating quantity
($\vec{\quad}$) vector quantity



SUMMARY

A theoretical and experimental study of dilute combusting sprays is described. The objective of the work was to assist development of spray combustion models by providing data for well-defined experimental conditions; and initiating evaluation of models of combusting sprays, typical of current practice, using the new measurements. Both test conditions and analysis were chosen to emphasize effects of interphase transport of mass, momentum and energy as well as drop-turbulence interactions.

Measurements considered ultra-dilute combusting sprays to minimize uncertainties in continuous-phase properties and experimental results. The test arrangement was a turbulent, methane-fueled diffusion flame burning in still air. Monodisperse (initial diameters of 105 and 180 μm) streams of methanol drops were injected along the axis of the flame, at its base. Drop mass flow rates were low so that flame structure was not influenced significantly by drop combustion and the mean and turbulent properties of the flame were known from earlier work. Present structure measurements included: mean and fluctuating phase velocities, mean drop number flux distributions, drop-size distributions and mean gas temperatures. Initial conditions were known from measurements at the burner exit, while ambient conditions of the flame were well-defined. The transport properties of individual drops were calibrated by auxiliary measurements using drops supported in the post-flame region of a flat-flame burner.

Analysis of the combusting sprays was undertaken to help interpret the measurements and to initiate evaluation of models of the process. Two approaches were considered: (1) a deterministic separated flow model, where effects of finite interphase transport rates are considered but drop-turbulence interactions are ignored; and (2) a stochastic separated flow model, where effects of finite interphase transport rates and drop-turbulence interactions are considered using random sampling for turbulence properties and random-walk computations for drop motion. Drop combustion was also treated by taking limits, either considering or ignoring the presence of envelope flames around individual drops.

The deterministic separated flow model was not very successful for present test conditions, since neglect of drop-turbulence interactions caused drop spread rates to be underestimated. The stochastic separated flow model yielded encouraging predictions with all empirical parameters either fixed from earlier work in noncombusting flows or set by the independent calibration tests. The distinction between the presence or absence of envelope flames did not influence predictions appreciably, since the drops primarily evaporated in the core of the flow where oxygen concentrations are low. The present experiment was useful for studying drop transport and drop-turbulence interactions and should be considered by others. The parabolic flow facilitates numerically--closed computations, initial conditions are readily measured, boundary conditions are well-defined, and flow properties are conducive to reasonably accurate measurements.

1. INTRODUCTION

The primary objective of this investigation was to complete new measurements of the structure of dilute combustng sprays, useful for evaluating models of the process. Model evaluation was also initiated, considering several methods typical of current combustng spray analysis. This research was motivated by the widespread application of combustng sprays in aircraft and rocket propulsion systems. The availability of reliable models of spray combustion processes would be of great value in reducing the need for costly and time-consuming, cut-and-try testing during combustor development.

Past work on spray flames, and related processes of particle-laden jets, was recently reviewed by one of us; therefore, the details will not be repeated here [1,2].* It was concluded that the most pressing current need was for additional data to support spray model development--particularly for test conditions where boundary conditions can be well-defined and initial conditions for both phases can be specified. The present study is the final phase of an investigation which sought to contribute information of this nature. Earlier phases of the study considered particle-laden jets [3-7], nonevaporating sprays [8-11] and evaporating sprays [12]. A brief report of current findings for combustng sprays can be found in Ref. [13]. More complete details and complete tabulations of data for noncombusting flows, can be found in previous reports and theses issued as part of this study [14-19]. The present report presents similar results for the combustng sprays.

Experience during earlier phases of this study showed that it is very difficult to provide adequate data using practical spray injectors--even in very simple flow situations, such as sprays injected into stagnant air. The main difficulty involves the dense-spray region near the injector, where current instrumentation is difficult to apply due to obscuration by drops, the presence of liquid sheets and ligaments, and the small dimensions of the region which causes problems in obtaining adequate spatial resolution. Furthermore, it is difficult to present results for polydisperse sprays, even in regions where reliable measurements can be made. The information required to characterize the flow is vast, including all continuous-phase properties, drop-size distributions, and both mean and fluctuating velocities as a function of drop size, among others.

In order to obtain a more tractable experiment, the present test configuration was simplified considerably. This involved creating the combustion environment with a methane-fueled diffusion flame burning in still air. Ultra-dilute sprays were studied in this environment by injecting monodisperse streams of drops (105 and 180 μm initial diameter) at the base of the flame--along the axis. The flow was lightly-loaded with drops; therefore, flame structure was controlled by

*Numbers in brackets denote references.

methane combustion and could be studied once-and-for-all with no drops present. This same flame configuration was studied during earlier work in this laboratory; therefore, a detailed picture of its structure was known, e.g., profiles of mean and fluctuating velocities, mean temperatures, and the mean concentrations of major gas species [20-22]. A portion of these measurements were repeated during the present investigation to provide more detail in the drop-containing region, e.g., mean and fluctuating velocities and mean gas temperatures. In addition, the following measurements of drop properties were made: mean and fluctuating drop velocities, drop number flux distributions, and drop-size distributions. Present measurements included careful characterization of the properties of both phases at the burner exit; therefore, the test results should be useful for evaluating models of sprays.

The experimental results were analyzed to help interpret the measurements and to initiate evaluation of spray models. Two methods typical of current practice were considered: (1) a deterministic separated flow (DSF) model, where effects of finite interphase transport rates are considered but drop-turbulence interactions are ignored; and (2) a stochastic separated flow (SSF) model, where both finite interphase transport rates and drop-turbulence interactions are considered using random-walk computations for drop motion and transport. The former method is typical of most current spray models [1]. The latter method is based on a proposal by Gosman and Ioannides [23], which yielded encouraging results during the earlier phases of this investigation considering noncombusting flows [1-19].

During past work [1-19], the locally homogeneous flow (LHF) approximation for spray analysis was also examined. With this approach, transport rates between the phases are assumed to be infinitely fast, which implies that drop and gas velocities are the same and that local thermodynamic equilibrium is maintained in the flow. The LHF approximation, however, is only useful when drop diameters are small--generally less than 10 μm in diameter [1]. Since present test conditions were chosen to provide significant effects of finite interphase transport, it was not worthwhile to pursue LHF calculations in this study.*

All turbulent sprays and particle-laden flows have the potential for interesting drop (particle)-turbulence interactions. A new element appearing in combusting flows, however, is the possible existence of envelope flames around individual drops when they contact oxygen-containing regions in a turbulent flame environment [1]. This problem was studied during the present investigation by conducting calculations for the limiting conditions where envelope flames are either considered or ignored. Analysis of single-drop transport was

*In a sense, results for the gas phase are equivalent to LHF results, since the drop loading was very small during present tests.

calibrated for both conditions, using data from drops supported in the post-flame region of a flat-flame burner.

In the following, experimental and theoretical methods are described first. The structure of the diffusion flame is then considered. The report concludes with discussion of spray flame predictions and measurements. All data are tabulated in the Appendix.

2. EXPERIMENTAL METHODS

2.1 Test Arrangement

A sketch of the test apparatus appears in Fig. 1. The burner flow is directed vertically upward. The combustion products are removed near the ceiling of the test cell using a hood and blower. The test-cell dimensions were: 5 m wide, 7 m long, and 5 m high.

The flame was contained within a screened enclosure to minimize effects of room disturbances. The enclosure dimensions were 1 m square cross-section, 2.5 m high, with a single layer of screen (630 wires/m, square pattern, 0.25 mm wire diameter). Rigidly-mounted optical instrumentation was used for some measurements; therefore, the entire cage assembly was traversed, using a bearing track, to measure radial profiles. Vertical traversing was accomplished by another track in conjunction with a jack. Transverse motion, largely used to trim the position to find the centerline, was accomplished using a linear positioner. Transverse positions could be located within 0.10 mm, while vertical positions could be located within 0.25 mm.

The burner assembly was a modified version of the design of Jeng and coworkers [20-22]. The burner had provision for attaching the flame at the burner exit and for injecting the drops vertically into the base of the flow. A sketch of the burner appears in Fig. 2. The burner was constructed of brass. The top surface of the burner was coated with a radiation-absorbing paint (Rust-Oleum, type 4279) having an emissivity of 0.96. A mixture of methane and natural gas entered a baffled chamber at the bottom of the burner passed along the exit port of the drop generator, and then flowed out of the burner through a contraction section. The diameter at the inlet of the contraction was 25 mm and the burner exit diameter was 5 mm. The contraction was shaped according to the prescription of Smith and Wang [24], in order to obtain a uniform exit velocity.

The top surface of the burner was cooled with water which flowed through a passage (not shown in Fig. 2) concentric with the burner exit. Water flow rate was adjusted to keep the top surface of the burner within 0.5 K of the room temperature, in order to avoid the formation of a natural convection plume which would disturb the flame flow field. The temperature of the top surface of the burner was measured using 26 gauge chromel/alumel thermocouples, which were cemented directly to the surface.

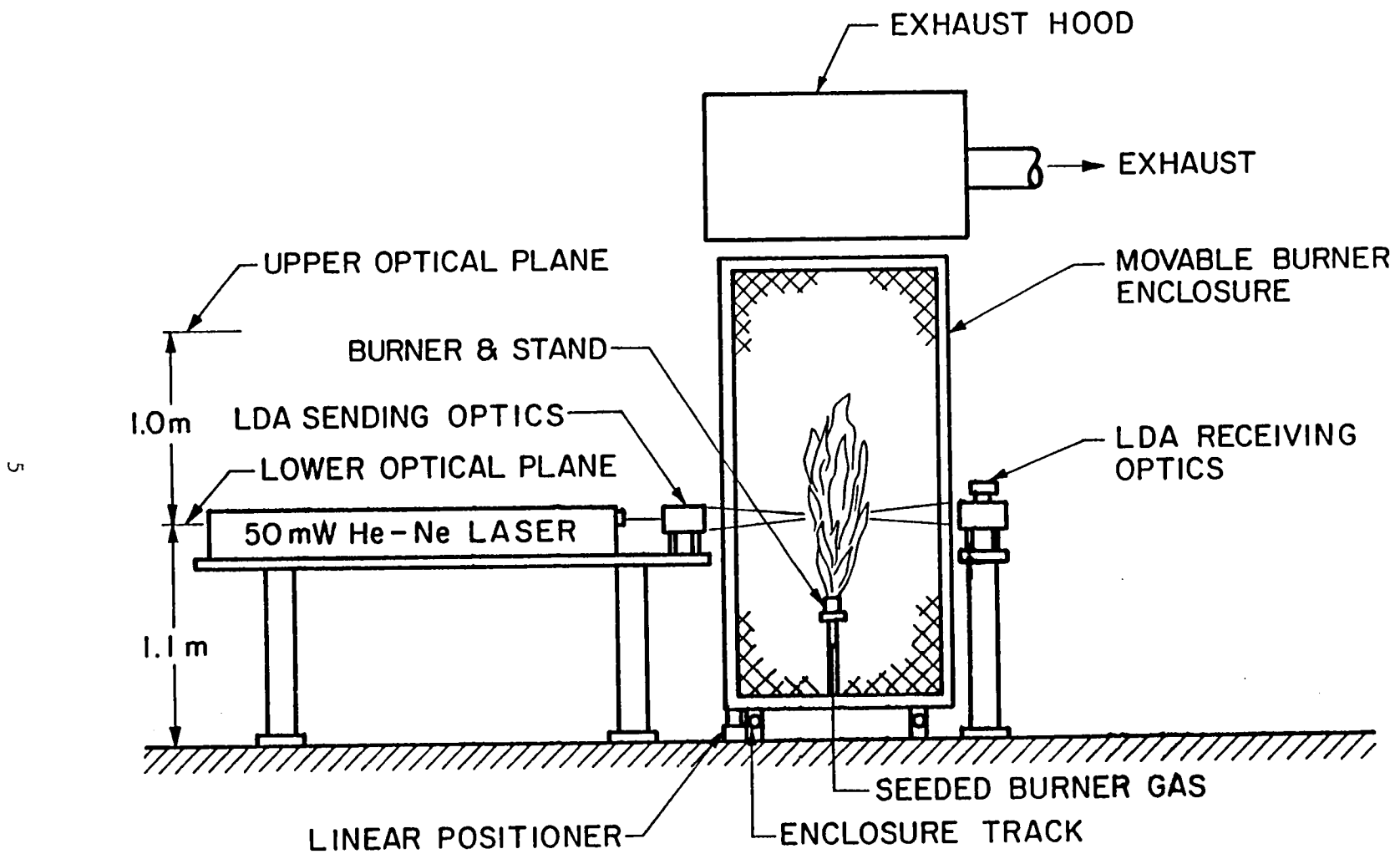


Fig. 1. Sketch of the test apparatus.

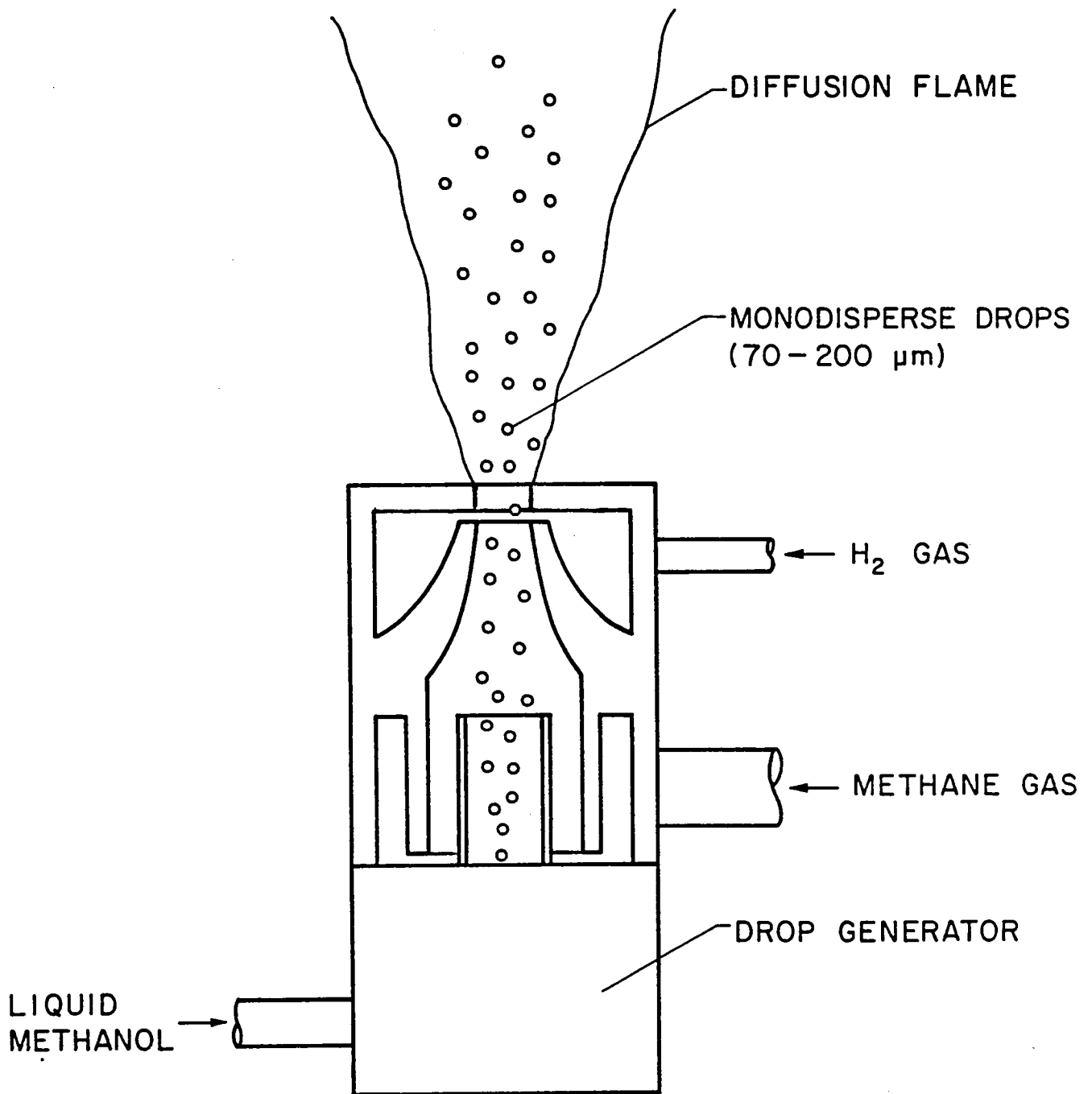


Fig. 2. Sketch of the burner assembly.

The flame was stabilized at the burner exit using a small annular flow of hydrogen. The hydrogen entered the flow through a 2 mm high slot, whose upper edge was 1.2 mm below the burner exit.

The monodisperse stream of drops was produced using a commercial vibrating orifice Berglund-Liu monodisperse drop generator (TSI, model 3050). The generator was removed from the manufacturer's cabinet and mounted directly on the lower end of the burner, with an adaptor which could be adjusted to center the generator orifice. A dispersing gas flow of methane was supplied to the generator, to eliminate coalescence of the drop stream. The stream of drops and dispersing gas flowed up a cylindrical tube (9.5 mm outside diameter, 1.8 mm wall thickness, 19 mm long) which ended 6.4 mm below the inlet of the contraction section.

Operation of the drop generator was checked using the flash photography system of Solomon [19]. This was a useful check since small errors in generator settings resulted in drop coalescence which destroyed drop uniformity.

The flow rate of methanol was obtained directly by timing the motion of the syringe pump used to feed the fuel to the generator. The flow rate of natural gas was measured using a laminar flow element (Merriam, model 50MW20-1) which was calibrated according to its pressure drop (which was measured with an inclined manometer). The flow rate of methane dispersing gas was measured using a Matheson model 603 rotameter. A second methane flow rate was used to provide seeding particles in the burner flow during gas velocity measurements; this flow was measured with a Matheson model 604 rotameter. The flow rate of hydrogen was measured using a Matheson model 603 rotameter. All gas flow instruments were calibrated using Precision Scientific Company wet-test meters (0.10 and 1.0 cu. ft. per revolution).

2.2 Test Conditions

The properties of the test gases are summarized in Table 1. The natural gas composition is only typical and can vary depending on the product mix of the supplier. Since the natural gas contained nearly 95% methane, and was supplemented with additional methane flows for the drop generator dispersing gas and the particle seeder, the fuel will be referred to as methane in the following.

The turbulent flame test conditions are summarized in Table 2. Only one burner gas flow condition was considered; corresponding to the highest Reynolds number flame studied by Jeng and coworkers [20-22]. This flame had an initial Reynolds number of 11,700 and was fully turbulent over its length with the region of luminosity extending 400-600 mm. Effects of buoyancy were also relatively small over the luminous region of the flame [20-22], which corresponded to the region of interest for the present multiphase flow tests. The hydrogen stabilizing flow was 2.8% (by mass) of the burner flow; therefore, flame properties were primarily those of a methane-fueled flame in the absence of drops (although the flame would be lifted without the hydrogen flow).

Table 1. Composition of Test Gases

Species	Source	Percent by Volume
Methane	Matheson, Commercial Purity	99.0
Hydrogen	Matheson, Extra-Dry Purity	99.9
Natural Gas	Columbia Gas Co., Typical Composition	
Methane		94.863
Ethane		3.753
Propane		0.266
iso-Butane		0.039
n-Butane		0.047
iso-Pentane		0.019
mono-Sulfur		0.009
di-Sulfur		0.012
Mercaptans		0.016
n-Pentane		0.016
Hexane		0.084
Nitrogen		0.408
Carbon Dioxide		0.423
neo-Pentane		0.006
Hydrogen Sulfide		0.019
Hydrogen		0.020

Table 2. Summary of Turbulent Flame Test Conditions

Nominal Drop Diameter (μm)	105	180
Liquid Volume Flow Rate ($\mu\text{l/s}$) ^b	12.21	24.48
Generator Frequency (kHz)	20	7.96
Generator Orifice Diameter (μm)	50	100

^aNatural gas and hydrogen flow rates of 520 and 14.6 mg/s; burner exit diameter of 5 mm; initial Reynolds number of 11,700; initial centerline velocity ($x/d = 1$) of 52.8 m/s; ambient temperature and pressure of 300 ± 2 K and 97 kPa.

^bMethanol (laboratory grade).

Two spray conditions were examined, corresponding to initial drop diameters of 105 and 180 μm . The maximum mass flow rate of methanol was less than 0.004% of the burner gas; therefore, the methane flame was influenced by the drops to a negligible degree.

2.3 Instrumentation

2.3.1 Gas Velocity

Present structure measurements included: phase velocities, drop-number flux, drop-size distributions, and mean gas temperatures. Each of these measuring systems will be described in the following.

Mean and fluctuating velocities were measured using a dual-beam, single-channel, frequency-shifted laser Doppler anemometer (LDA). The components of the LDA are summarized in Table 3. Two sets of sending and receiving optics were used yielding measuring volume dimensions of 100, 120 μm ($x/d \leq 1$) and 247, 720 μm ($x/d > 1$).

The LDA actually measures the velocity of small seeding particles in the flow. Aluminum oxide particles having a nominal diameter of 0.5 μm were employed for seeding. Both the burner gas and the air surroundings were seeded using reverse-cyclone seeders described by Glass and Kennedy [25]. Operation of the seeders yielded particle densities on the order of 10^9 particles/ m^3 .

Mean and fluctuating velocity components of the gas phase were measured at various axial and radial locations in the test flame. An integration period of one minute or more was used to determine the mean quantities. Radial profiles were obtained in a single traverse across the flow and components of mean and fluctuating velocities were recorded by employing different beam orientations at each radial location. Measurements of the tangential component of the fluctuating velocity ($\overline{w'^2}$)¹² were made with a separate traverse in the third direction. Reynolds stress measurements were made near the centerline in order to find the flow axis (since Reynolds stress is zero at the centerline and doesn't exhibit the broad maxima encountered for other variables).

Potential errors and uncertainties in the LDA measurements are discussed in Appendix A. Uncertainties (95% confidence interval) in mean and fluctuating velocity components were 5% while uncertainties in k were 10%. All measurements were repeatable within these limits.

2.3.2 Drop Velocity

Drop velocities were measured using the same LDA arrangement as the gas velocity measurements. In this case, gain settings of the photomultiplier and counter were set to low values so that only strong scattering signals from large particles were recorded. The processor output was collected with a MINC 11/23 minicomputer and processed to yield mean and fluctuating drop velocities (finding number-averaged velocities). When these tests were run, the gas phase was not seeded, to reduce the potential for bias errors with small drops. Various

Table 3. Summary of LDA Components

Component	Manufacturer	Model	Specification/Function
Helium-Neon Laser	Spectra Physics	125A	TEM ₀₀ mode, 632.8 nm wavelength, 2.0 mm beam diameter, 50 mW power
Polarization Rotator	TSI	9102-2	
Beam Splitter	TSI	9115-2	50 mm beam spacing
Frequency Shifter	TSI	9180-2	Bragg cell, 2 kHz - 40 MHz shift frequency
Transmitting Lens ^a	TSI	9118	241 & 600 mm focal length, 60 mm clear aperture
Receiving Assembly	TSI	9140	
Detector Lens	TSI	920	200 mm focal length 60 mm clear aperture
Photodetector	TSI	9160	photomultiplier with 0.25 mm diameter aperture
Filter	TSI	9157	632.8 nm central wavelength, 10 nm bandwidth, 60% peak transmittance
Dual Beam Oscilloscope	Tektronix	912	
Frequency Tracker	TSI	1090-1A	2 kHz - 50 MHz bandwidth
Burst Counter	TSI	1980-A	100 MHz bandwidth
Digital/Analog Converter	TSI	1988	used for analog output from burst counter
True RMS Voltmeter	TSI	1076	
Integrating Digital Voltmeter	Hewlett-Packard	240IC	

^aOnly one set having equal focal lengths for focusing and collecting used at a time.

components of drop velocity were measured in the same manner as the gas phase.

Errors and uncertainties in mean and fluctuating drop velocities were the same as to the gas velocity measurements, cf. Appendix A. These measurements were also repeatable within these limits during the period of testing.

2.3.3 Drop-Size Distributions

The sprays were so dilute that flash photography was not effective for determining drop-size distributions, e.g., the number of in-focus drops on each photograph was too small to make this method economically feasible. As an alternative, the slide impaction method of Shearer et al. [26] was used, similar to earlier phases of the present investigation [10,11].

Figure 3 is a sketch of the slide impactor. Small glass slides, coated with a layer of magnesium oxide, were exposed to the flow for a timed period. The drops leave a crater in the coating upon impact, which can be related to initial drop size even though they subsequently evaporate.

May [27] presents results indicating that the crater diameter varies with slide and drop properties; therefore, the ratio between crater and drop diameters was calibrated. Streams of drops, having various initial diameters, were produced by the monodisperse drop generator and impacted on the slides. The initial drop size was measured using the flash photography system of Solomon [19], while crater size was measured using a microscope (the general practice for data reduction from the slides). It was found that the crater diameter varied with both drop diameter and velocity; therefore, a calibration of these effects was used to reduce present measurements.

The raw drop-size distribution is influenced by the collection efficiency of the impactor, which varies with both drop size and velocity [28]. For present tests, the drop size ranges at a point were relatively narrow since the drops were initially monodisperse; therefore, the correction factors of the distribution were essentially unity (or zero). As a result, the distributions were not corrected and are reported as measured. This practice is adequate, except in regions where drops are small ($SMD < 30$) where present SMD values are biased upward since small drops were not collected.

The slide impactor required long sampling times to gather drops since the spray was very dilute. Therefore, SMD was evaluated using roughly 200 drops in the sample. While this sample is small, in comparison to drop counts used for SMD in polydisperse sprays, the uncertainty in SMD was comparable since the drops were initially monodisperse and drop-size distributions were relatively narrow, except at the flame tip. Errors and uncertainties of the slide impactor are discussed in Appendix A. For SMD values greater than $30 \mu\text{m}$, the uncertainty in SMD (95% confidence interval) was less than 10%.

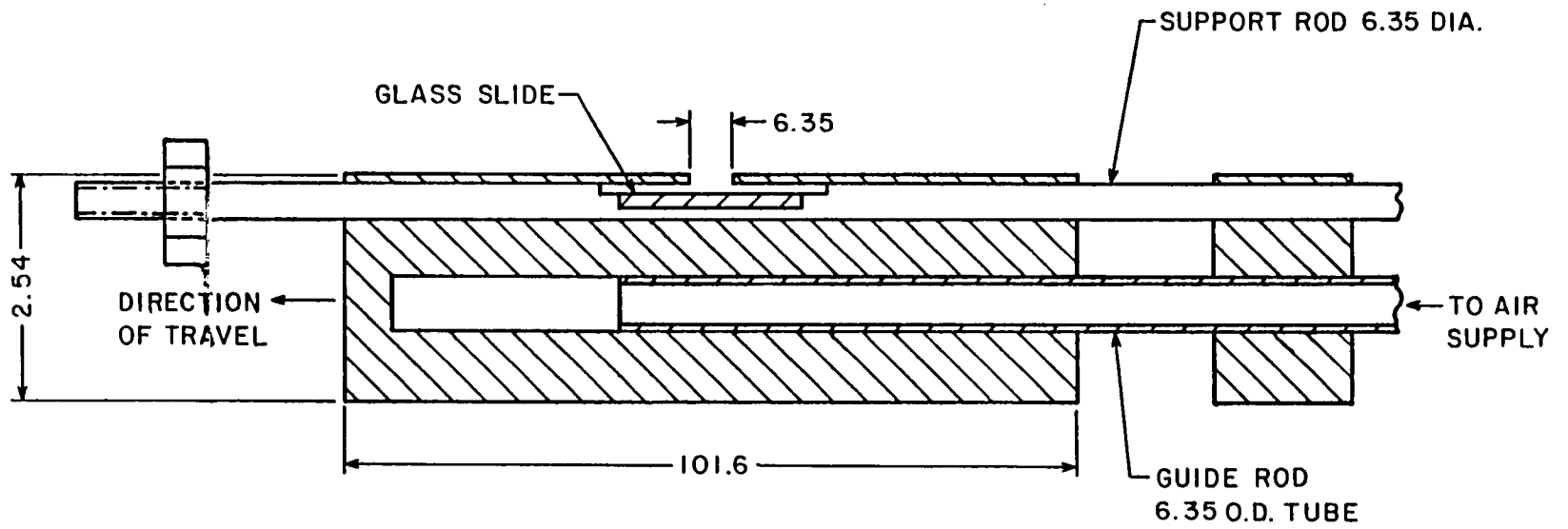


Fig. 3. Sketch of the slide impactor.

2.3.4 Drop Number Flux

Drop number fluxes were measured using the Mie-scattering system illustrated in Fig. 4. The equipment list for this system appears in Table 4. The beam from a 50 mW HeNe laser was passed through a beam expander and round-hole aperture to yield a relatively uniform-intensity beam. Aperture dimensions were varied to increase spatial resolution near the burner exit and to reduce sampling times in regions of low drop concentrations far from the burner exit. A cylindrical lens system then focussed the beam into a flat (waist height 78-156 μm , depending on the aperture used) sheet whose plane was normal to the streamwise direction.

Drops passing through the light sheet generated scattered-light pulses which were observed from an angle of 90° to the laser beam in the plane of the light sheet. The collecting and detector lenses and the aperture of the photodetector defined the measuring area. A laser-line filter was placed in the path of observation, to reduce effects of flame luminosity and increase signal-to-noise ratios.

The output of the photodetector was observed on an oscilloscope. Each drop passing through the measuring volume yielded a light pulse which was recorded and counted using a pulse counter constructed in this laboratory, cf. Appendix B for a description of the pulse counter. Generally, more than 1000 drops were counted in order to obtain the mean number flux.

The cross-sectional area of observation varied with drop size. This effect was calibrated over the size range of interest and the different aperture sizes--as described in Appendix B. The maximum cross-sectional areas of observation were for 180 μm diameter drops, as follows: 0.2 mm^2 for $x/d \leq 12$ and 2.9 mm^2 for $x/d > 12$. The raw data was corrected for the drop-size effect, using the measured drop-size distributions.

Uncertainty analysis for these measurements is described in Appendix A. The major source of uncertainty was the calibration of the cross-sectional area of observation as a function of drop size. Estimated uncertainty in drop number flux measurements is less than 15% (95% confidence interval).

2.3.5 Mean Gas Temperature

The thermocouple probe used for mean gas temperature measurements is illustrated in Fig. 5. The thermocouple junction was constructed by butt-welding 75 μm diameter Pt/Pt-10% Rh wires. The wires were attached to heavier lead wires of the same materials, having diameters of 750 μm and spaced 12.7 mm apart. The wires were coated with silica, to eliminate catalytic effects. The thermocouple probe was mounted in a linear positioner, accurate to 1 mm.

The output of the thermocouple was sampled and processed using a DEC MINC 11-23 minicomputer to yield time-averaged mean temperatures.

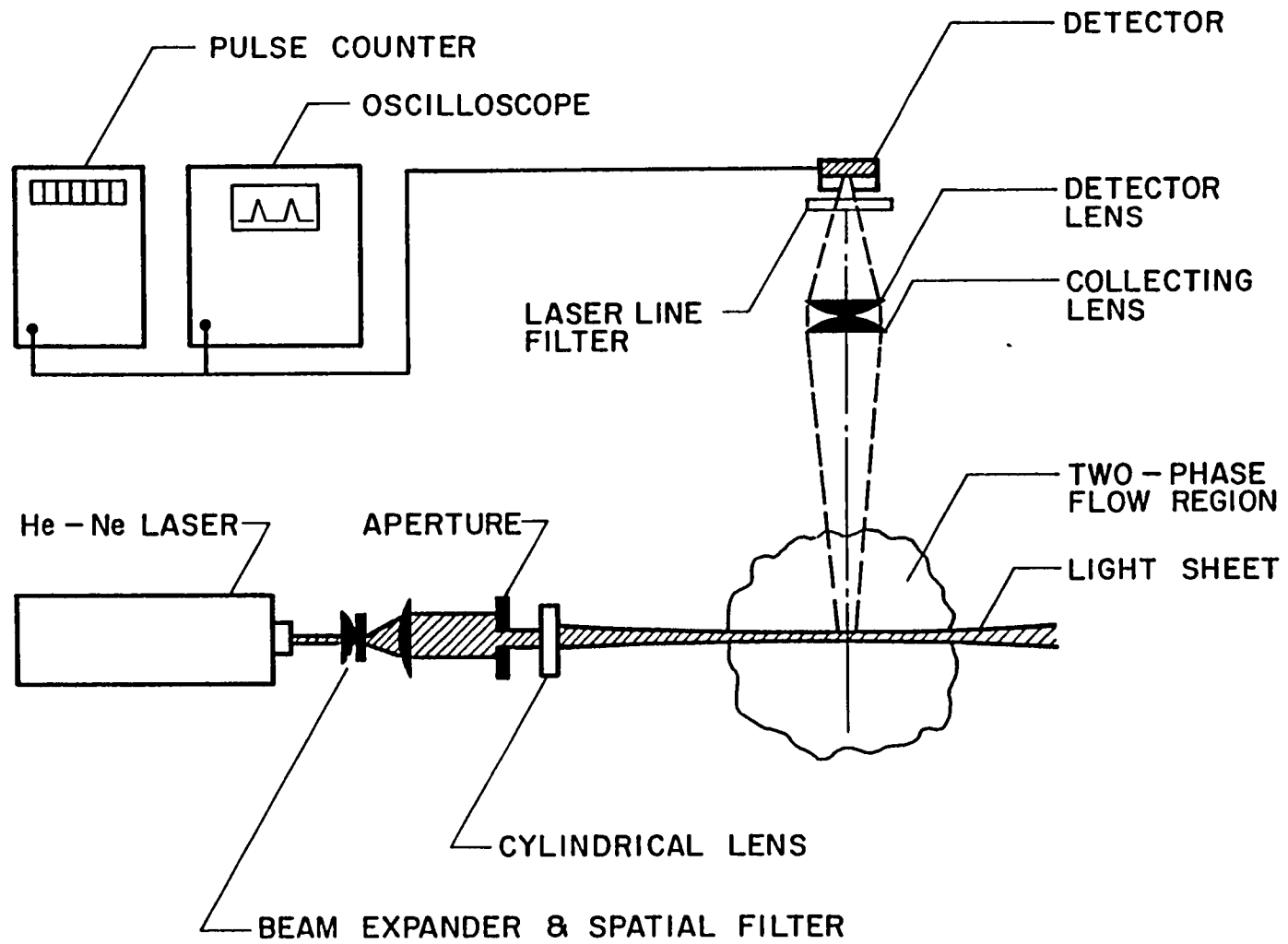


Fig. 4. Sketch of the drop number flux system.

Table 4. Summary of Drop Number Flux Components

Component	Manufacturer	Model	Specification/Function
Helium-Neon Laser	Spectra Physics	125A	TEM ₀₀ mode, 632.8 nm wavelength, 2.0 mm beam diameter, 50 mW power
Beam Expander	Spectra Physics		15 mm output beam diameter
Aperture ^a	in-house	--	3.1 and 6.2 mm diameter apertures
Cylindrical Lens	unknown	--	600 mm focal length
Collecting Lens	TSI	9119	595 mm focal length 60 mm clear aperture
Detector Lens	TSI	920	200 mm focal length 60 mm clear aperture
Filter	TSI	9157	632.8 central wavelength, 10 nm bandwidth, 60% peak transmittance
Digital Oscilloscope	Nicolet	Explorer III	20 MHz sampling rate
Photodetector	TSI	9160	photomultiplier with 0.25 mm diameter aperture
Pulse Counter	in-house	--	12 V max voltage, 2 V threshold adjust, 1 MHz response

^aSmall aperture for $x/d \leq 12$, large aperture otherwise.

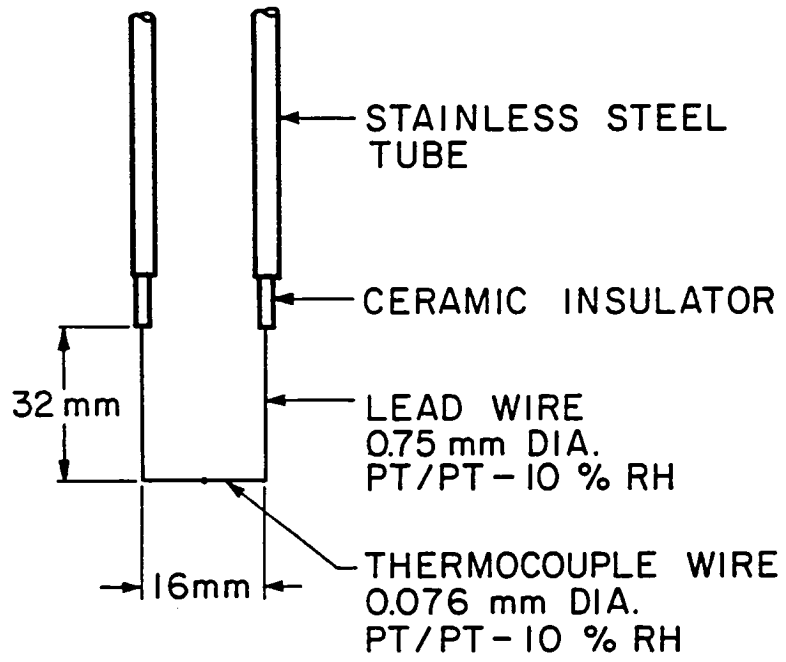


Fig. 5. Sketch of the temperature probe.

The raw data was corrected for radiation errors following the procedure described in Appendix C. The uncertainty of these measurements is estimated to be less than 5% of the local mean temperature difference between the gas and the surroundings, cf. Appendix A.

3. THEORY

3.1 General Description

Two theoretical models of spray processes were considered: (1) a deterministic separated flow (DSF) model, where finite interphase transport rates are considered, but effects of drop-turbulence interactions are ignored, i.e., the drops are only assumed to interact with the mean flow; and (2) a stochastic separated flow (SSF) model, where effects of finite interphase transport rates and drop-turbulence interactions are treated using random sampling for turbulence properties in conjunction with random-walk computations for particle motion. In both cases, analysis follows past work in this laboratory on noncombusting particle-laden jets and sprays [1-19]. The main theoretical extension of the present investigation involves treating effects of combustion with respect to both the drops and the gas phase.

Since the sprays were extremely dilute, the structure of the gas phase turbulent diffusion flame was not appreciably influenced by drops; therefore, source terms due to drops and the volume of the drops were ignored in the governing equations of the continuous phase. The continuous-phase analyses employed a k - ϵ - g turbulence analysis, since this approach has been effective during earlier work in this laboratory [1-22].

We average over flow variations on the scale of drops and consider analysis of drop transport in the flame environment. Given the results of the gas phase analysis, drop motion and transport is computed over the lifetime of a drop using a Lagrangian formulation.

In the following, the gas phase solution is described first. Then drop transport calculations and their calibration with single-drop experiments are discussed. The section concludes with descriptions of the DSF and SSF models.

3.2 Continuous-Phase Analysis

3.2.1 Governing Equations

The continuous-phase analysis treats a steady, axisymmetric turbulent diffusion flame in an infinite stagnant environment. The analysis follows procedures proposed by Lockwood and Naguib [29], but with extensions due to Bilger [30,31] and Liew et al. [32]. This involves solution of the mass-weighted (Favre)-averaged governing equations using a k - ϵ - g turbulence closure. Scalar properties are found from the conserved-scalar (mixture fraction) formalism, in conjunction with the laminar flamelet technique for prescribing instantaneous scalar properties. This approach has provided encouraging predictions of the structure of turbulent, gas-fueled, diffusion flames (including the current test flame) during recent work

in this laboratory [20-22,33]. Agreement with measurements was obtained using fixed empirical parameters in the turbulence model--based on measurements in noncombusting constant and variable density jets.

Major assumptions of the continuous-phase analysis were: boundary layer approximations apply; since gas velocities were low, viscous dissipation and the kinetic energy of the mean flow were ignored; typical of most turbulence models, the exchange coefficients of all species and heat were assumed to be the same; the contribution of buoyancy to turbulence quantities was neglected, since this approximation yielded reasonably good predictions of mean and turbulent flame structure in the present slightly-buoyant flame in the past [20-22]; and effects of radiation were neglected, since the present flame only lost roughly 14% of its chemical energy release by this mechanism.

Under these assumptions, the gas-phase flow structure can be found by solving governing equations for conservation of mass, mean momentum, mean mixture fraction, turbulent kinetic energy, rate of dissipation of turbulent kinetic energy and the square of mixture fraction fluctuations, as follows:

$$\frac{\partial}{\partial x} (\bar{\rho} \bar{u} \phi) + \frac{1}{r} \frac{\partial}{\partial r} (r \bar{\rho} \bar{v} \phi) = \frac{1}{r} \frac{\partial}{\partial r} (r \mu_{\text{eff}, \phi} \frac{\partial \phi}{\partial r}) + S_{\phi} \quad (3.1)$$

where

$$\bar{\phi} = \overline{\rho \phi} / \bar{\rho} \quad (3.2)$$

is a Favre-averaged quantity. ϕ is a generic quantity denoting 1 (for conservation of mass), \bar{u} , \bar{f} , k , ϵ or g . The expressions for $\mu_{\text{eff}, \phi}$ and S_{ϕ} appearing in Eq. (3.1) are summarized in Table 5, along with the appropriate empirical constants. The turbulent viscosity, μ_t , is calculated from the turbulent kinetic energy and its rate of dissipation, as follows:

$$\mu_t = C_{\mu} \bar{\rho} k^2 / \epsilon \quad (3.3)$$

The boundary conditions for Eqs. (3.1) are

$$r = 0, \quad \frac{\partial \phi}{\partial r} = 0; \quad r \rightarrow \infty, \quad \phi = 0 \quad (3.4)$$

The condition at $r = 0$ is only applied beyond the end of the potential core.

Initial conditions were specified by assuming uniform properties across the burner exit, except for a shear layer having a thickness equal to 1% of the jet radius. For the present flame, \bar{u}_0 and k_0 were measured, while ϵ_0 was estimated by matching the variation of k in

Table 5. Source Terms in Equation (3.1)

$\bar{\phi}$	$\mu_{eff, \phi}$	S_{ϕ}
1	--	0
\bar{u}	$\mu + \mu_t$	$a (\rho_{\infty} - \bar{\rho})$
\bar{f}	$(\mu/Sc) + (\mu_t/\sigma_f)$	0
k	$\mu + (\mu_t/\sigma_k)$	$\mu_t \left(\frac{\partial \bar{u}}{\partial r}\right)^2 - \bar{\rho} \epsilon$
ϵ	$\mu + (\mu_t/\sigma_{\epsilon})$	$(C_{\epsilon 1} \mu_t \left(\frac{\partial \bar{u}}{\partial r}\right)^2 - C_{\epsilon 2} \bar{\rho} \epsilon)(\epsilon/k)$
g	$(\mu/Sc) + (\mu_t/\sigma_g)$	$C_{g1} \mu_t \left(\frac{\partial \bar{f}}{\partial r}\right)^2 - C_{g2} \bar{\rho} g \epsilon / k$

C_{μ}	$C_{\epsilon 1}$	C_{g1}	$C_{\epsilon 2} = C_{g2}$	σ_k	σ_{ϵ}	$\sigma_f = \sigma_g$	Sc
0.09	1.44	2.8	1.87	1.0	1.3	0.7	0.7

the potential core (noting that all radial gradients of flow properties are zero in this region). Furthermore, $\tilde{f}_0 = 1$ and $g_0 = 0$, by definition. Thus the initial condition for the major portion of the flow is as follows:

$$x = 0, \quad 2r/d \leq 0.99;$$

$$\tilde{u}_0, k_0 = \text{measured}, \quad \epsilon_0 = \text{matched}, \quad \tilde{f}_0 = 1, \quad g_0 = 0 \quad (3.5)$$

Flow properties in the shear layer were found from the governing equations after neglecting convection and diffusion terms. Subsequent boundary conditions along the inner edge of the shear layer were determined by solving the transport equations within the potential core.

The conserved scalar formalism was used to find $\bar{\rho}$, needed to solve Eqs. (3.1), as well as other scalar properties, e.g., mean temperature and mean mass fractions of major gaseous species (CH_4 , O_2 , N_2 , CO , CO_2 , H_2O and H_2). Under present assumptions, the instantaneous values of all scalar properties are only functions of the instantaneous mixture fraction--termed the state relationships. Specification of state relationships, $\phi(f)$, will be considered in the next section; for the present, these quantities will be assumed to be known.

Given the $\phi(f)$, the Favre-averaged mean and variance of scalar flow properties are found from the mass-averaged probability density function (PDF) of f , $\tilde{P}(f)$, as follows [30]

$$\tilde{\phi} = \frac{\overline{\rho\phi}}{\bar{\rho}} = \int_0^1 \phi(f) \tilde{P}(f) df \quad (3.6)$$

$$\overline{\phi'^2} = \frac{\overline{\rho\phi'^2}}{\bar{\rho}} = \int_0^1 (\phi(f) - \tilde{\phi})^2 \tilde{P}(f) df \quad (3.7)$$

In the same manner, Bilger [30], shows that time-averaged means and variances are:

$$\bar{\phi} = \bar{\rho} \int_0^1 (\phi(f)/\rho(f)) \tilde{P}(f) df \quad (3.8)$$

$$\overline{\phi'^2} = \bar{\rho} \int_0^1 \frac{1}{\rho(f)} (\phi(f) - \bar{\phi}(f))^2 \tilde{P}(f) df \quad (3.9)$$

The value of $\bar{\rho}$ can be found by setting $\phi = 1$ in Eq. (3.8).

A functional form must be assumed for $\tilde{P}(f)$, although predictions have a relatively weak sensitivity to the specific form

chosen. Following past practice [21-23,33] a clipped-Gaussian function was used for $\tilde{P}(f)$. This function has two parameters which must be specified: μ , its most probable value; and σ , its standard deviation. These quantities can be found by noting [29]:

$$\bar{f} = \int_0^1 f \tilde{P}(f) df \quad (3.10)$$

$$g = \int_0^1 (f - \bar{f})^2 \tilde{P}(f) df \quad (3.11)$$

Both \bar{f} and g are known from solving Eq. (3.1); therefore, Eqs. (3.10) and (3.11) provide two implicit equations to find μ and σ . These computations can be time-consuming; therefore, Eqs. (3.10) and (3.11) were solved once the results tabulated as a functions of f and g to facilitate a table look-up procedure on the computer, cf. Shearer et al. [26].

Given $\tilde{P}(f)$ and $\phi(f)$, time- and Favre-averaged values of all scalar properties can be found by solving Eqs. (3.6) and (3.8).

3.2.2 State Relationships

Methods for constructing state relationships required by the conserved-scalar approach have received a great deal of attention. The earliest methods assumed local thermodynamic equilibrium [1,21,11,16,19,30,34,35]. Under present assumptions, this implies that the properties of the flow at each mixture fraction are equivalent to the properties of an adiabatic flame having the same mixture ratio and initial conditions of the fuel and air streams. With this approach, state relationships can be constructed routinely, using a standard chemical equilibrium computer package routine, e.g., CEC76 described by Gordon and McBride [36].

The thermodynamic equilibrium method yields reasonably good results for mixture fractions corresponding to lean fuel-air ratios, but yields large errors at fuel-rich conditions. For rich mixture ratios, low gas temperatures cause slow rates of chemical reaction which prevents equilibration of the mixture. A "partial equilibrium" method has been proposed to rectify this problem [1].* The partial equilibrium assumes thermodynamic equilibrium only up to a critical mixture fraction, f_c , or critical fuel equivalence ratio, ϕ_c . For higher fuel equivalence ratios, mixture properties are found assuming adiabatic mixing of the pure fuel stream and the equilibrium mixture at ϕ_c . The approach is useful to the extent that ϕ_c is relatively universal, in fact, evidence to date suggests $\phi_c = 1.2$ provides reasonably good results [22].

*This is poor choice of terminology and does not correspond to conventional use of the term "partial equilibrium" in the chemical kinetics literature, where it implies that a portion of the reversible reactions at a point are in equilibrium.

Most flames exchange energy by radiation, however, this is not very significant for typical combustion chamber conditions; therefore, radiation effects are generally treated as a perturbation. The state relationships are then obtained by allowing for the loss of a fixed fraction of the combustion energy release by radiation.*

A more recent approach for constructing state relationships, which was adopted here, is the laminar flamelet method first proposed by Bilger [31] and subsequently developed by Liew et al. [32]. This follows from the observation that measurements of temperature and the concentration of major gas species provide nearly universal functions of mixture fraction for a wide range of shear rates and positions in laminar flames. State relationships are then found directly from these correlations, assuming that properties in a turbulent flame are the result of a succession of laminar flamelets sweeping past a given position. This implies a wrinkled-flame picture of a turbulent flame as well as a quasi-equilibrium structure for diffusion flames which is invariant for both laminar and turbulent conditions. Regions of attachment of laminar flames, where such invariance is not observed, cannot be used for constructing state relationships. Furthermore, turbulence scales must not be too small in comparison to the characteristic diffusion flame thickness. Finally, radiant heat loss fractions must be roughly the same for both the laminar and turbulent flame, a condition which must be checked on a case-by-case basis. In spite of these limitations, however, the laminar flamelet technique has provided reasonably good predictions of mean scalar properties in turbulent flames [20,22,32,33,37,38] and it represents the best approach currently available to treat turbulent diffusion flames.

State relationships for methane diffusion flames burning in air (both initially at normal temperature and pressure) are illustrated in Figs. 6 and 7. The temperature and mass fraction of major gas species (CH_4 , O_2 , N_2 , CO_2 , H_2O , CO and H_2) are plotted as a function of local fuel equivalence ratio for both the laminar flamelet and partial equilibrium ($\phi_C = 1.2$) methods. The laminar flame data of Tsuji and Yamaoka [39-41] and Mitchell et al. [42] are shown on the figures. These results involve rather different flame configurations: Tsuji and Yamaoka considering an opposed flow diffusion flame; Mitchell et al. considering coflowing streams of methane and air. Clearly, nearly universal correlations of the data are obtained as a function of mixture ratio. Use of $\phi_C = 1.2$ in the partial-equilibrium method yields results which are comparable to the measurements.** Similar results have been obtained for propane/air [20,33] and n-heptane/air [31] diffusion flames. Current work in this laboratory suggests that

*The radiant heat loss fraction of the flame must be found by other means. Methods of computing this loss for nonluminous flames are discussed by Jeng and coworkers [20,37,38].

**The partial-equilibrium method is mainly useful for the many instances where laminar flame data are not available for direct correlation.

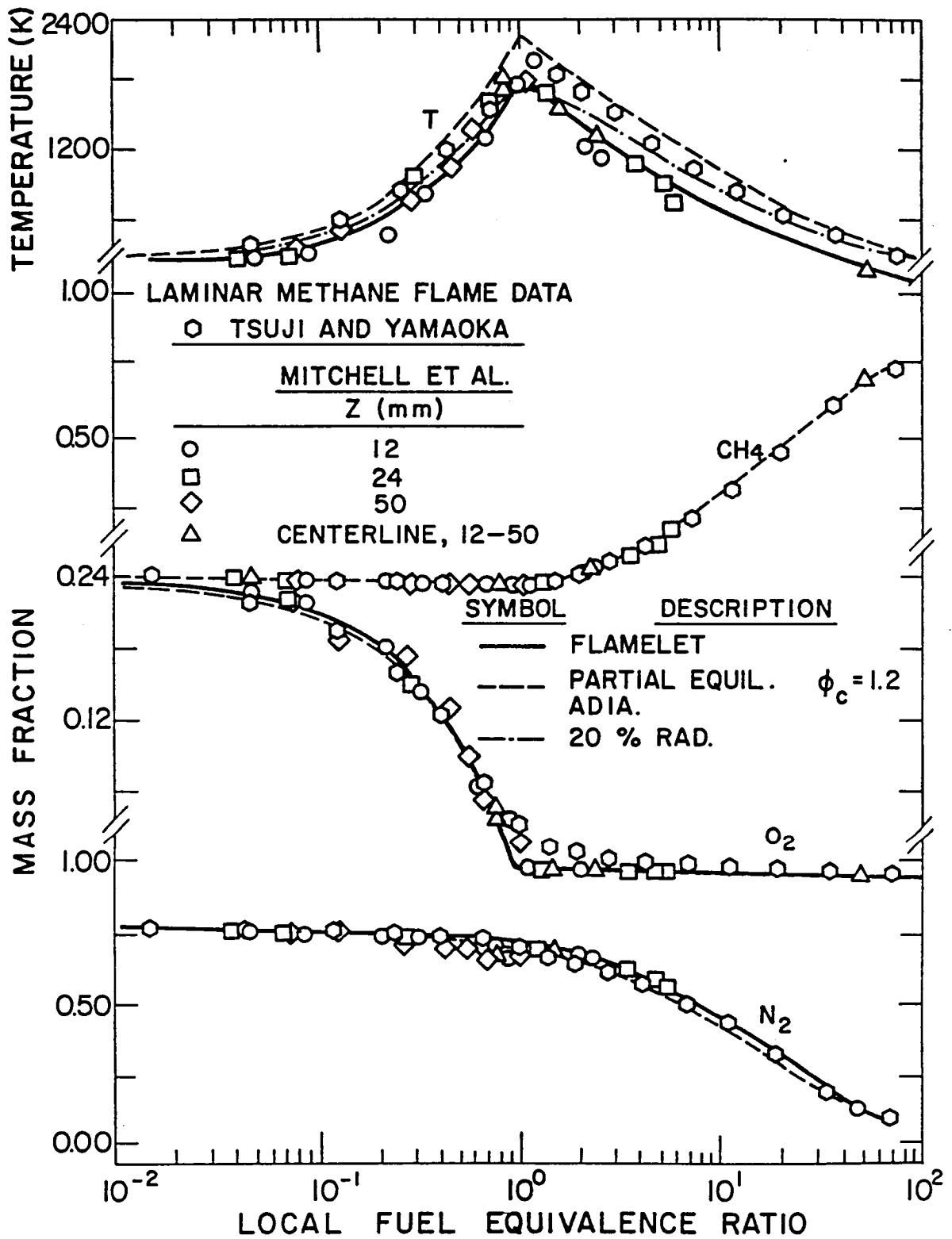


Fig. 6. State relationships for methane/air diffusion flames.

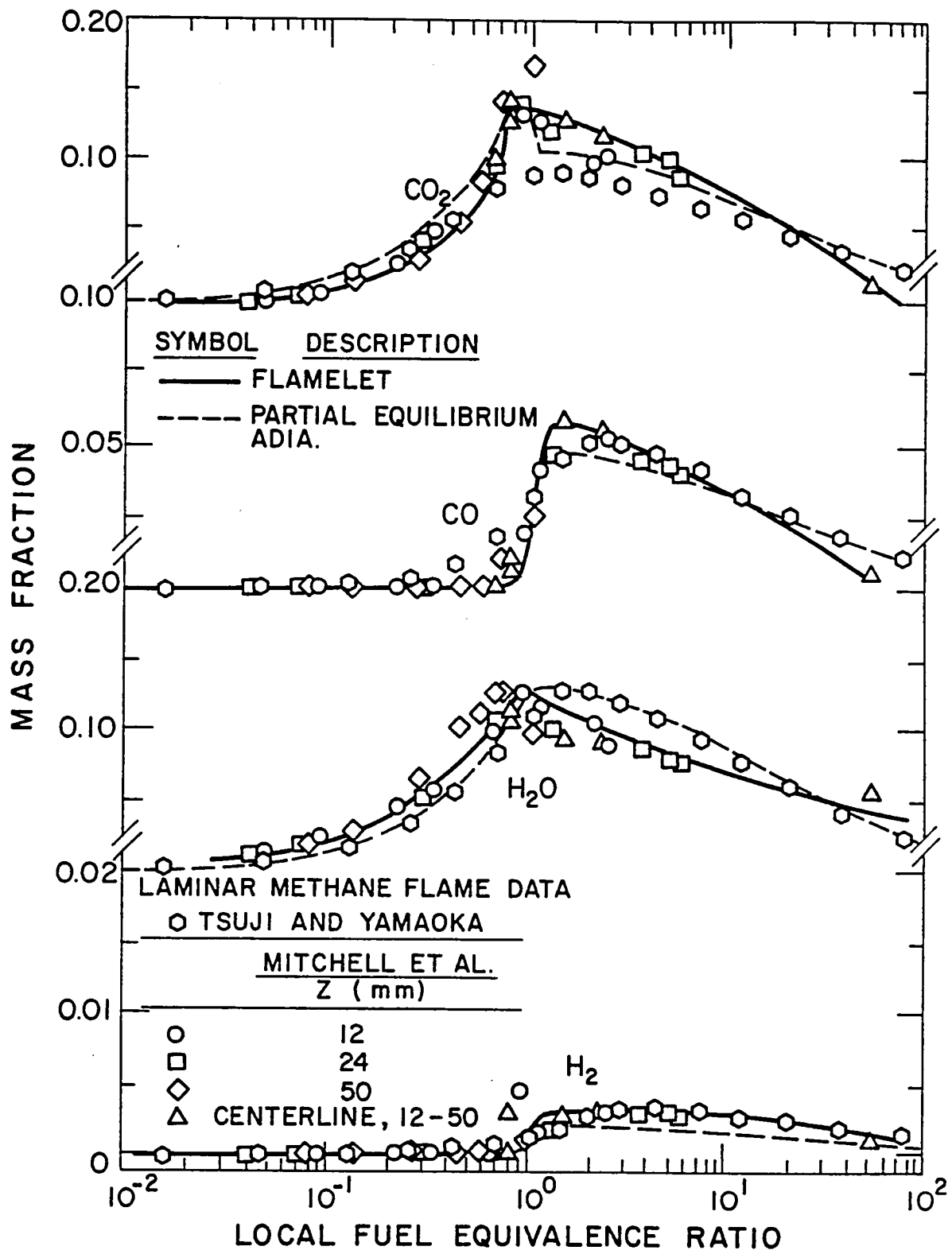


Fig. 7. State relationships for methane/air diffusion flames (continued).

H₂/air and CO/air flames can be correlated as well; therefore, the flamelet technique seems to have sufficient generality for practical use--until such time when problems of predicting chemical reactions in turbulent flames have been resolved.

Natural gas was used to fuel the present burner so that while the fuel was predominantly methane, several other fuel species were involved, cf. Table 1. To allow for this, structure measurements were made in a laminar flame using the local natural gas [43]. The test arrangement involved coflowing streams of fuel and air, similar to Mitchell et al. [42]. The results of these measurements are illustrated in Figs. 8 and 9. Clearly, a nearly universal correlation of the concentrations of major gas species is achieved, which was used for the present state relationships.

3.2.3 Computations

Calculations for the continuous phase were completed using a modified version of GENMIX [44]. The computational grid was similar to past work; 33 cross-stream grid nodes; and streamwise step sizes limited to 6% of the current flow width or an entrainment increase of 5%--whichever was smaller. A convergence check of the numerical solution was performed by comparing the mean mixture fraction flux between the exit of the injector and the downstream positions. If differences were greater than 1%, the calculation was redone using more cross-stream nodes and smaller streamwise steps.

3.3 Drop Transport

3.3.1 Drop Transport Analysis

Methods for calculating transport between drops and the continuous phase have been extensively discussed elsewhere [1]; therefore, the following discussion will be brief since current methods are essentially the same. A major assumption of the analysis is that we integrate over small features like drops; therefore, drop properties are computed by a Lagrangian calculation following their motion, using empirical expressions to evaluate the interphase transport of mass, momentum and energy.

The main assumptions of the drop-trajectory calculations were as follows: dilute spray with drop transport the same as for a single drop in an infinite environment and negligible drop shattering and collisions; quasisteady drop flow field, e.g., transport rates are found from steady flow conditions for the same boundary conditions while the radial velocity of the drop surface, due to evaporation, is neglected; empirical treatment of drag and forced convection; liquid surface in thermodynamic equilibrium with effects of drop curvature and surface tension on equilibrium neglected; negligible radiation; only concentration diffusion with equal binary diffusivities of all species; ideal gas mixture with constant average properties and unity Lewis number; negligible solubility of the ambient gases in the liquid phase; negligible virtual mass and Basset history forces; and transport within the liquid analyzed using the "thin skin" approximation [1]. These

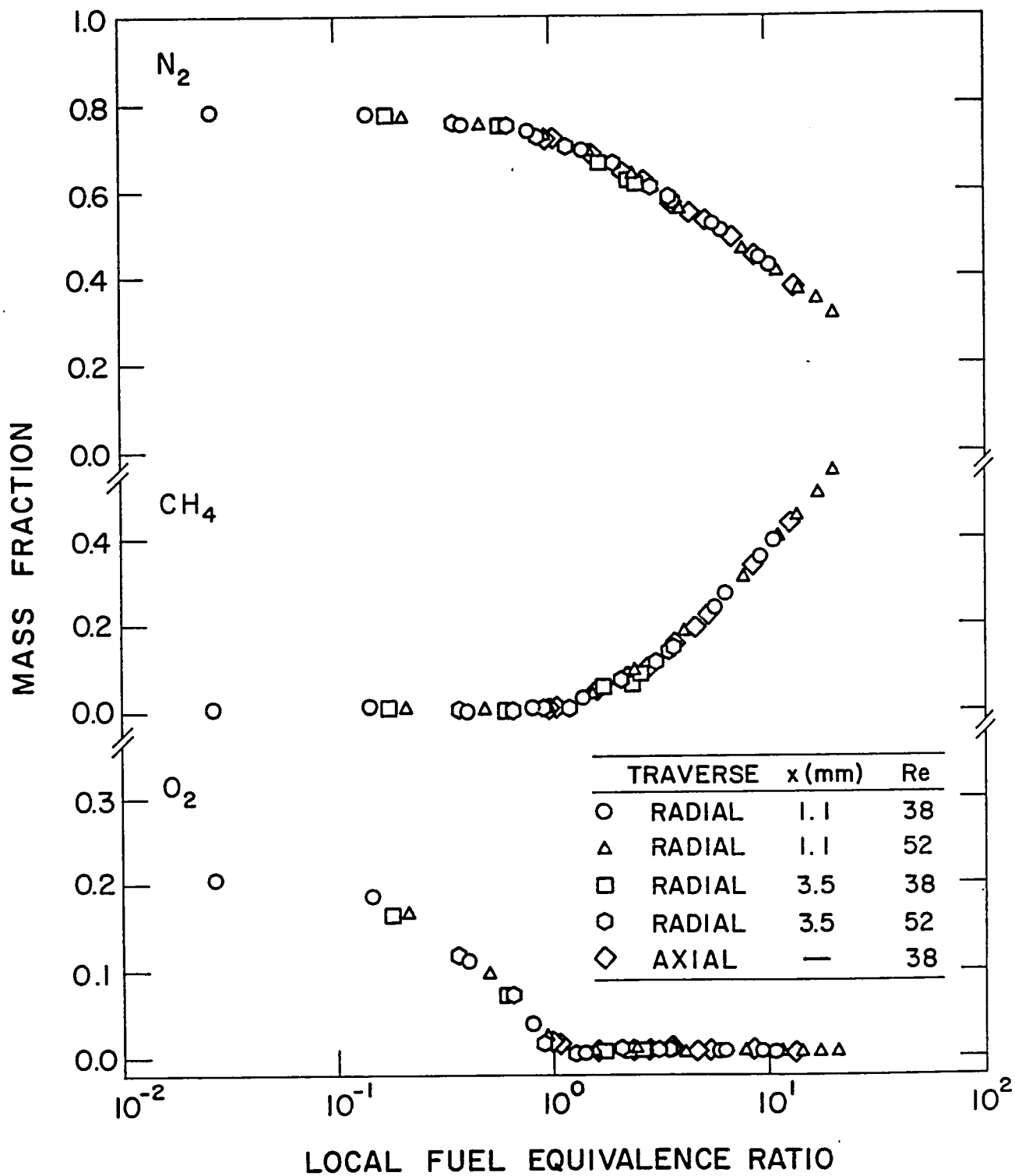


Fig. 8. State relationships for natural gas fueled flames.

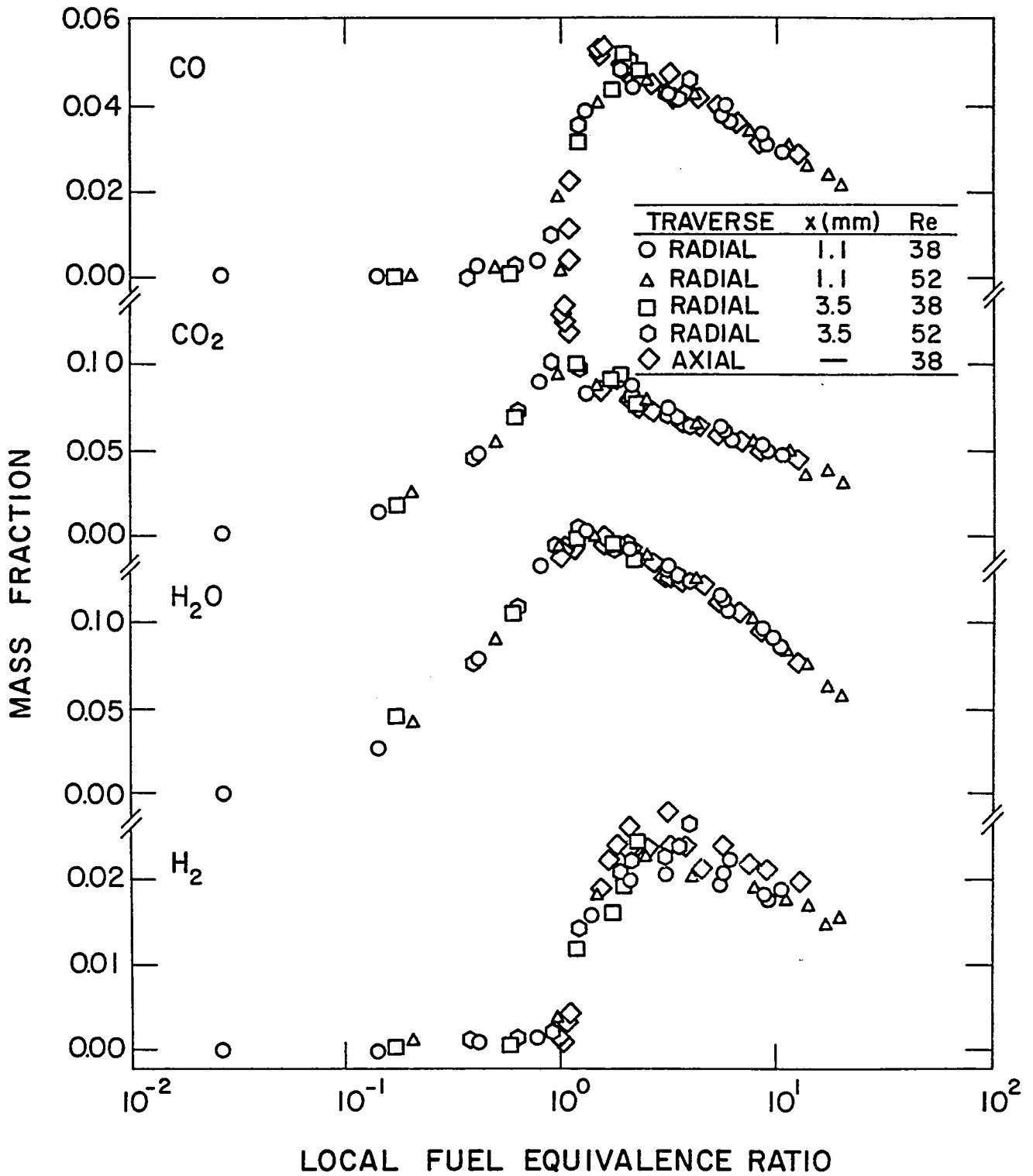


Fig. 9. State relationships for natural gas fueled flames (continued).

assumptions are common to most spray models, their justification and limitations are fully discussed elsewhere [1].

The thin skin approximation was adopted to avoid substantial complications required to treat transport within the drop. This involves the assumption that the drop surface adapts immediately to changes in local ambient conditions, while the bulk liquid remains at its initial state. This approximation yields results for transient drop effects which are comparable to the more widely used uniform drop-temperature approximation [1].

A key issue with respect to combusting sprays concerns the presence or absence of envelope flames around individual drops [1]. This had to be considered, since drops penetrated oxygen-containing regions during the present tests. Existing methods for estimating conditions where envelope flames are present are controversial and don't treat environments representative of turbulent flames [1]. These uncertainties were avoided by considering two limiting cases: (1) ignoring the presence of envelope flames in all regions of the flow; and (2) assuming that envelope flames were present whenever the local environment contained oxygen. Past work in this laboratory suggests that the differences between these two limits is not large until the local fuel equivalence ratio becomes less than 0.9 [45].

Two limits were also adopted with respect to drop-turbulence interactions: (1) the DSF approach, where drop transport is only controlled by local mean properties; and (2) the SSF approach where drops transport is computed for local instantaneous properties (which are estimated by random sampling of the continuous-phase solution). A generic formulation will be used in the following, applicable to both cases, i.e., gas properties will not be designated as either mean or instantaneous since either can apply depending on the spray model.

In both spray analyses, drops leaving the injector are divided into n groups, defined by the initial position, size, velocity and direction. The subsequent motion of each group is given by

$$\vec{x}_{pi} = \vec{x}_{poi} + \int_0^t \vec{u}_{pi} dt, \quad i = 1, 2, 3 \quad (3.12)$$

The mean drop velocity is determined by integrating the equation for conservation of momentum

$$m \frac{du_{pi}}{dt} = - (\pi/8) d_p^2 \rho C_D \left| \vec{u}_p - \vec{u}_i \right| (u_{pi} - u_i) + a_i, \quad i = 1, 2, 3 \quad (3.13)$$

The standard drag coefficient for solid spheres is employed in the calculations, approximated as follows [1]:

$$C_D = \frac{24}{Re} \left(1 + \frac{Re^{2/3}}{6}\right), \quad Re < 1000$$

$$= 0.44, \quad Re > 1000 \quad (3.14)$$

$$\text{where, } Re = \frac{d_p |\vec{u}_p - \vec{u}|}{\nu} \quad (3.15)$$

The size and mass of the drop are related as follows:

$$m = (\pi/6) \rho_{bf} d_p^3 \quad (3.16)$$

where ρ_{bf} is the bulk liquid density, which remains constant at the injected condition under the assumptions of the thin skin model.

The rate of change of drop diameter is given by

$$\frac{d d_p}{dt} = - 2\dot{m}''/\rho_{bf} \quad (3.17)$$

Heat and mass transfer rates to the drop are influenced by the presence or absence of envelope flames. The following expressions can be used for both cases.

$$\dot{m}'' d_p / (\rho D) = 2N_S \ln [(1 + B_Y)(1 + B_O)] \quad (3.18)$$

$$h d_p / \lambda = 2 N_P \ln [(1 + B_Y)(1 + B_O)] / B_Y \quad (3.19)$$

where

$$B_Y = (Y_{FS} - Y_{F\infty}) / (1 - Y_{FS}) \quad (3.20)$$

and

$$B_O = \nu_{FO} Y_{O\infty} \quad (3.21)$$

The stoichiometric parameter, ν_{FO} , is the mass of fuel consumed per unit mass of oxidant at the flame front. The heat transfer coefficient, appearing in Eq. (3.19) is based on the temperature difference between the envelope flame and the drop surface, e.g.,

$$h = \lambda \left(\frac{\partial T}{\partial r}\right)_s / (T_f - T_s) \quad (3.22)$$

Neglecting dissociation in the flame, the flame temperature can be found from

$$\frac{T_f - T_s}{T_\infty - T_s} = \left[1 + \frac{Y_{O_\infty} Q_r}{C_p (T_\infty - T_s)} \right] / \left[1 + \frac{B_O}{B_Y} (B_Y + B_O) \right] \quad (3.23)$$

where Q_r is the chemical energy released by combustion per unit mass of oxidant. The correction factors for \dot{m}'' and h due to forced convection are found from the following expressions:

$$N_P \text{ or } N_S = 1 + \frac{0.276 \text{ Re}^{1/2} (\text{Pr or Sc})^{1/3}}{(1 + 1.232/(\text{Re} (\text{Pr or Sc})^{4/3}))^{1/2}} \quad (3.24)$$

Equations (3.18)-(3.23) are used directly when envelope flames are considered. If $Y_{O_\infty} = 0$ at the current drop position, this formulation becomes equivalent to results for simple drop evaporation in a heated environment without combustion, e.g., $B_O = 0$ from Eq. (3.21) and $T_f = T_\infty$ from Eq. (3.23). Thus, calculations at the limit of no envelope flame present were conducted by the simple expedient of setting $Y_{O_\infty} = 0$ in the formulation, even in regions where finite concentrations of oxygen were present.

In order to complete the solution, the drop surface temperature and the fuel mass fraction at the drop surface must be known. The two equations required to solve for these quantities are provided by the fuel vapor pressure relationship and the energy balance at the liquid surface. The vapor pressure relationship has the form

$$Y_{FS} = f(T_s, p, Y_{is}) \quad (3.25)$$

Applying the thin-skin approximation, the energy balance at the surface becomes

$$h (T_f - T_s) = \dot{m}'' h_{fgT} \quad (3.26)$$

where h_{fgT} allows for both the enthalpy of vaporization and the heat up of the liquid from its initial temperature (the bulk liquid temperature) to the surface temperature

$$h_{fgT} = h_{fg} + C_{pF} (T_s - T_{bf}) \quad (3.27)$$

The vapor pressure relationship and other properties used for the liquid and gas phases, along with mixing rules used, are summarized in Appendix D. Gas-phase transport properties are found at a reference state, representing average conditions for the flow around the drop. The reference state was defined as follows:

$$\phi_{avg} = \alpha \phi_{g_s} + (1 - \alpha) \phi_{g_\infty} \quad (3.28)$$

where ϕ is a generic quantity representing either mass fraction or temperature, and $0 \leq \alpha \leq 1$. The value of α was selected to best match

computations using the present model and the single drop calibration experiments discussed in the next section.

Drop-life-history calculations were carried out using a second-order Runge-Kutta algorithm.

3.3.2 Drop Transport Calibrations*

It is well-known that a priori calculations of drop-life histories are very uncertain, when using constant-average-property models, due to the large variation of properties in the flow field [1]. Calibration tests were undertaken in the post-flame region of a flat-flame burner in order to reduce this uncertainty. The test results were used to match measurements and predictions by selecting an optimum value of α in Eq. (3.28).

Test methods for the calibration tests, along with a tabulation of data, are provided in Appendix E. Single methanol drops, supported on a quartz fiber, were rapidly immersed in the post-flame region of the burner. The drops were backlighted and photographed, with timing marks placed on the motion picture film. The film was processed using a motion analyzer to yield drop size as a function of time.

Gas properties at the test drop location were found as follows: gas composition, by sampling and analysis with a gas chromatograph; gas temperature, using the radiation-corrected thermocouple described in Section 2.3.5; and gas velocity, by computations assuming one-dimensional flow (knowing the burner flow rate and cross-sectional area, as well as the burned-gas density from the other measurements).

Test conditions for the drop-life-history calibrations are summarized in Table 6. The burner was fueled with methane/air mixtures having various fuel-equivalence ratios; therefore, the test gases were representative of the turbulent flame. Drop diameters for the calibration tests were large, however, Reynolds numbers are comparable to the turbulent flame conditions, due to the low velocities of the flat-flame-burner gases. Finally, the flow in the flat-flame burner was laminar; eliminating uncertainties due to drop-turbulence interactions.

Predicted and measured drop-life histories are illustrated in Fig. 10. The period considered corresponds to steady-burning after initial drop heat up is complete. Test conditions were all for fuel equivalence ratios less than unity; therefore, predictions are shown for the limiting cases of envelope flames both present and absent. Envelope flames were observed for the test conditions; therefore, the data is matched to this limit. The results yielded an optimum value of $\alpha = 0.3$, in Eq. (3.28). This value is not a universal, since it depends on the assumptions of the drop transport analysis, the method

*The authors wish to acknowledge the help of J. T. Holl in carrying out these calibrations.

Table 6. Summary of Drop-Life-History Test Conditions

Fuel Equivalence Ratio	0.65	0.82	0.97
Initial Drop Diameter (μm)	2293	2786	2954
Gas Temperature (K)	1500	1690	1690
Gas Mass Fractions			
O ₂	0.076	0.038	0.000
N ₂	0.755	0.744	0.778
H ₂ O	0.077	0.098	0.099
CO	0.004	0.000	0.001
CO ₂	0.088	0.120	0.122
Initial Drop Re	19	21	28

^aMethanol drops supported in the post-flame region of a flat-flame burner fueled with methane-air mixtures.

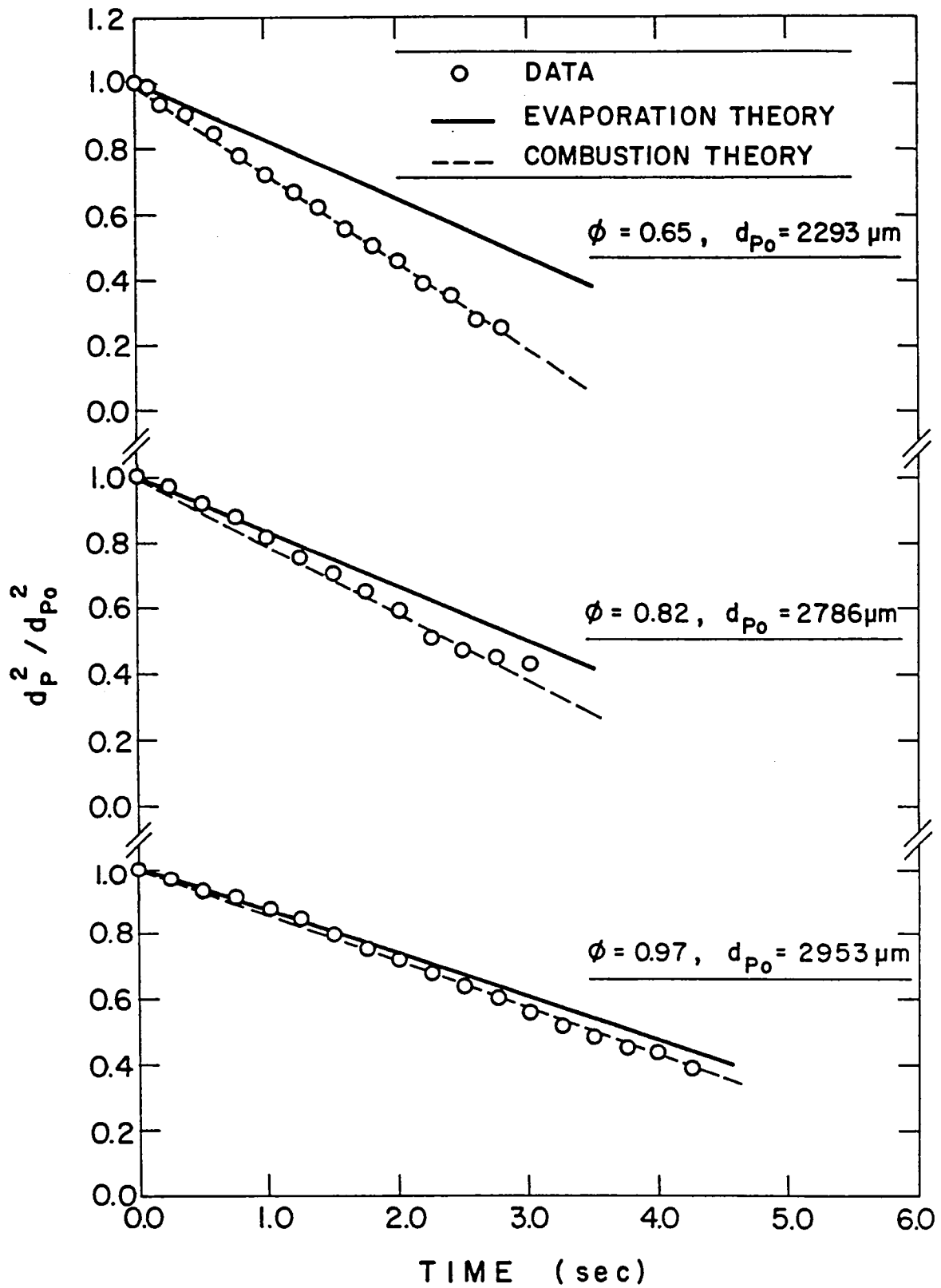


Fig. 10. Drop-life-history calibrations.

of computing average properties, and the correlation of transport properties in the calculations. Values of α in the range 0.3-1.0 have been found during past work [1,17,19,26,34,35,45]. The value selected here, however, provides excellent agreement between predictions and measurements in Fig. 10.

Differences between computations considering and ignoring envelope flames are not very large for the highest fuel equivalence ratio considered in Fig. 10 and, of course, are irrelevant for fuel equivalence ratios greater than unity where ambient oxygen concentrations are negligibly small, cf. Figs. 6 and 8. Differences between the two methods progressively increase, however, as the fuel equivalence ratio decreases, since the presence of the envelope flame enhances combustion both due to increased flame temperature (in comparison to the surroundings) and due to its consumption of fuel vapor before the edge of the flow field around the drop is reached. These trends are similar to those observed by Szekely and Faeth [45]. The greatest uncertainty, based on current knowledge, involves a reliable criterion for predicting the presence of envelope flames [1].

3.4 Deterministic Separated Flow Model

The most stringent assumption of the DSF model is that drops only interact with the mean flow; therefore, turbulent dispersion of drops and effects of turbulent fluctuations on drop transport properties are ignored. Neglecting turbulent dispersion implies that drops follow deterministic trajectories in the flow, prescribed by their initial conditions. Drops are generally much smaller than the smallest turbulent scales in the present flow [1]; therefore, the influence of turbulent fluctuations on drop transport properties pertains to drops interacting with relatively large eddies--from the perspective of the drop. Use of mean properties in this instance is only true when the transport rate is a linear function of property differences between the drop surface and its local surroundings. This is never strictly true, and is particularly in error for drag, which is quadratic in the slip velocity for Reynolds numbers typical of drops in sprays (values ca. 100).

While Favre-averages are convenient for computations of continuous-phase properties, only time-averaged properties are relevant for defining the flow along a drop trajectory. This represents no problem for scalar properties, since time-averaged scalar properties can be computed from Eq. (3.8).

Time-averaged mean gas velocity must also be known for trajectory computations with the DSF model. However, to obtain the time-averaged velocity from the computed Favre-averaged velocity, the correlation between fluctuating density and fluctuating velocity must be known, since [30], e.g.,

$$\bar{u} = \bar{u} - \overline{\rho' u'} / \bar{\rho} \quad (3.29)$$

Density fluctuations and velocity fluctuations are neither statistically independent nor perfectly correlated in jet diffusion flames;

therefore, an extension of the basic model of Section 3.2 would be required to predict $\rho'u'$. This was beyond the scope of the present study; therefore, we chose to assume statistical independence--setting Favre- and time-averaged velocities equal. Fortunately, existing evidence suggests that the two methods of averaging are not very different for jet flames, with differences of ca. 5% [22].

Initial conditions for the DSF model were defined at the burner exit,* where drop size, velocity, direction and number density were known as a function of position. At this location, drops were placed in n groups according to these properties, and the motion of each group was tracked through the flow field. This involved numerical integration of Eqs. (3.12)-(3.27), using the second-order algorithm in conjunction with mean gas properties found from the continuous-phase solution.

When calculating drop properties in the flow field, for comparison with measurements, the properties of each group were weighted to satisfy their initial number flux. The trajectories of 100 groups were computed in order to obtain a statistically-significant representation of drop-phase properties.

3.5 Stochastic Separated Flow Model

The DSF model considers only deterministic trajectories for drop groups. The stochastic separated flow (SSF) model, however, includes effects of turbulent fluctuations on drop dispersion and interphase momentum transport rates by using a technique proposed by Gosman and Ioannides [23] and subsequently developed in this laboratory [1-19].

The stochastic model involves computing the trajectories of a statistically-significant sample of individual drops as they move away from the injector and encounter a random distribution of turbulent eddies--utilizing Monte Carlo methods. The key elements of this approach are the methods for specifying the properties of each eddy and the time of interaction of a drop with a particular eddy.

Properties within a particular eddy were assumed to be uniform, but to change in a random fashion from eddy to eddy. The trajectory calculation was the same as the DSF model, involving solution of Eqs. (3.12)-(3.27). Mean-gas properties in these equations, however, are replaced by the instantaneous properties of each eddy.

The properties of each eddy were found at the start of drop-eddy interaction by making a random selection from the probability density function (PDF) of velocity. Velocity fluctuations were assumed to be isotropic with a Gaussian PDF having a standard deviation of $(2k/3)^{1/2}$ and mean components \bar{u} , \bar{v} , 0. This ignores the distinction between Favre- and time-averaged velocities (the latter being the quantity that should be sampled), similar to the DSF analysis where Favre- and time-averaged velocities were assumed to be the same. The

*Formally, $x/d = 1$.

cumulative distribution function for each velocity component was constructed and sampled. This involved randomly selecting three numbers in the range 0-1 and computing the velocity components for these three values of the cumulative distribution function. This corresponds to random choices of velocity which satisfy the assumed forms of the velocity PDF's.

The instantaneous scalar properties of each eddy were computed in a similar manner. Scalar properties are only a function of mixture fraction, under present assumptions; therefore, only a random selection of mixture fraction had to be made. Given the mixture fraction, the state relationships provided all scalar properties, e.g., Figs. 8 and 9. Only the time-averaged PDF of mixture fraction is relevant for sampling. This was constructed from the known Favre-averaged PDF at each point, by noting [30]

$$\rho(f) \bar{P}(f) = \bar{\rho} \bar{P}(f) \quad (3.30)$$

The time-averaged cumulative distribution function of f was then constructed and sampled to find the instantaneous value of f . A random number in the range 0-1 was selected and the instantaneous f became the value of f that yielded this value of the cumulative distribution function. Values of f chosen this way yield a random distribution which satisfies the clipped-Gaussian PDF.

Similar to past practice, a drop was assumed to interact with an eddy for a time which was the minimum of the eddy lifetime and the time required for the drop to traverse the eddy. The specification of eddy lifetime and size is somewhat ad hoc, however, present methods have been extensively calibrated and evaluated for particle laden jet flows and noncombusting sprays, yielding excellent results [1-19].

The characteristic size of an eddy was taken to be the dissipation length scale from the k - ϵ model, e.g.,

$$L_e = C_\mu^{3/4} k^{3/2} / \epsilon \quad (3.31)$$

The eddy lifetime was computed from this length scale and the velocity fluctuations, taken to be isotropic, as follows:

$$t_e = L_e / (2k/3)^{1/2} \quad (3.32)$$

Drops were assumed to interact with an eddy as long as the time of interaction, Δt , and the distance of interaction $|\Delta \vec{x}_p|$, satisfied the following criteria:

$$\Delta t \leq t_e \quad , \quad \left| \Delta \vec{x}_p \right| \leq L_e \quad (3.33)$$

Drop capture by an eddy corresponds to ending the interaction with the first criterion while a drop traverses an eddy when the interaction is ended with the second criterion.

The remaining computations are similar to the DSF model. More drop trajectories must be considered to obtain statistically significant drop properties than the DSF analysis (generally 5000-6000 trajectories were used). A by-product of the additional calculations, however, is that the SSF model yields both mean and fluctuating drop properties. This provides an additional test of model performance.

4. RESULTS AND DISCUSSION

4.1 Introduction

In the following, measurements of the turbulent test flame and the two test sprays will be described, cf. Table 2 for operating conditions. In addition, the DSF and SSF model predictions will be used to help interpret the measurements. Naturally, this also provides an opportunity to evaluate these models for reasonably well-defined test conditions.

Time-averaged mean and fluctuating velocities were measured but are compared to Favre-averaged predictions--for lack of an alternative without extending the continuous phase analysis. As noted earlier, these properties are not very different for turbulent jet flames; therefore, the distinction is not important in comparison to present experimental uncertainties [22].

Mean concentrations were measured by isokinetic sampling for the test flame [22]. While this was thought to yield Favre-averaged properties originally [30], recent work suggests that measurements are between Favre- and time-averaged properties [46]. In fact, the average obtained depends very much on the flow properties and response of the sample probe and its flow system--which is not known very well. Therefore, for lack of a definitive alternative, Favre-averaged predictions are compared with measurements of species concentrations. Differences on the order of 5% for mean concentrations can be expected for these two methods of averaging in jet flames [22]; therefore, the distinction is not large in view of experimental uncertainties.

Temperatures measured with small thermocouples having fast response, and time-averaged, yield time averages. However, large thermocouples yield values between time and Favre averages with currently unknown effects of radiation and radiation corrections on the average actually obtained. Since potential differences are less than uncertainties in the radiation correction [20], Favre averages will be compared with measurements in the following.

Drop velocities were particle-averaged over all sizes during the measurements. The following predictions were obtained by averaging in the same manner for consistency.

Drop number fluxes were time-averaged over all sizes (after correcting for the variation of capture area with drop size). The same procedure was used for computed results.

Slide impactors obtain time-averaged drop size distributions, as opposed to spatial averages yielded by flash photography methods [10-12,19]. This quantity, as well, was computed in a consistent manner for the predictions.

In the following, initial conditions will be described first, followed by a discussion of the properties of the test flame. Then the results for sprays will be considered. All data are tabulated in Appendix F.

4.2 Initial Conditions

Due to the LDA and burner configurations it was not possible to make measurements of mean and fluctuating phase velocities closer than $x/d = 1$; therefore, burner initial conditions were obtained at this position as discussed earlier. The burner flow was seeded, however, the hydrogen coflow was not; therefore, traverses in the radial direction were limited to $r/x \leq 0.6$, since seeding levels were too low (and results would be biased to the burner flow gas depending on mixing) at larger radial distances.

Figure 11 is an illustration of mean and fluctuating velocities of the burner gas. Mean velocities are relatively uniform for $r/x < 0.4$ and then decrease as the shear layer at the edge of the potential core is encountered. Velocity fluctuations and the turbulence kinetic energy are also relatively uniform in the core, but then increase due to turbulence production in the shear layer. The main difference between the present burner and that of Jeng [20] is that turbulence kinetic energy is more than an order of magnitude higher, probably as a result of the drop generator inducing disturbances in the burner flow.

Drop sizes were essentially constant at the burner exit, with initial diameters of 105 and 180 μm . Distributions of mean and fluctuating drop velocities and drop number fluxes across the burner exit are illustrated in Figs. 12 and 13 for the two sprays. Mean drop velocities are essentially constant (within 2%) over the region where they could be measured. Drop velocity fluctuations are on the order of 2% of the mean drop velocity of $d_{p0} = 105 \mu\text{m}$, primarily due to the operation of the drop generator. Drop velocity fluctuations are nearly constant over the exit, except near the shear layer for $d_{p0} = 105 \mu\text{m}$, where \bar{u}_p' are increasing (\bar{v}_p' and \bar{w}_p' to a lesser degree) in response to higher gas-phase turbulence levels. In contrast, drop number fluxes decrease rapidly with increasing radial position, since turbulent dispersion has had little time to act and the drop generator delivers the drops along the centerline. Few drops were observed for $r/x > 0.4$. The spray with the larger drops, $d_{p0} = 180 \mu\text{m}$, is less dispersed at this position, due to the larger inertia of these drops which makes them less responsive to turbulent dispersion.

4.3 Scalar Structure of the Test Flame

In this section, the scalar structure of the test flame will be discussed. The main features of this are comparison of present measurements with earlier work by Jeng and coworkers [20-22] for

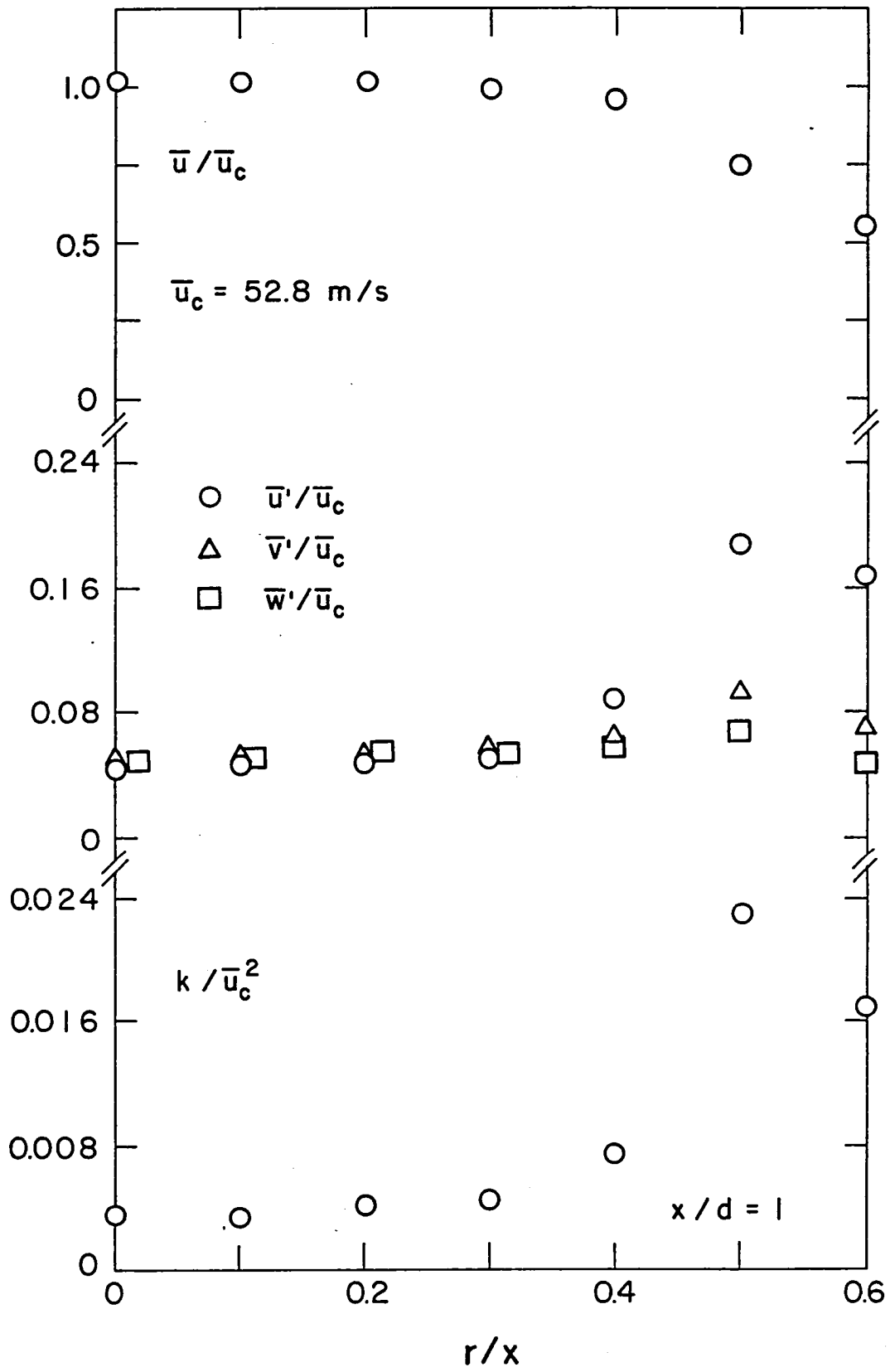


Fig. 11. Mean and fluctuating gas velocities at $x/d = 1$.

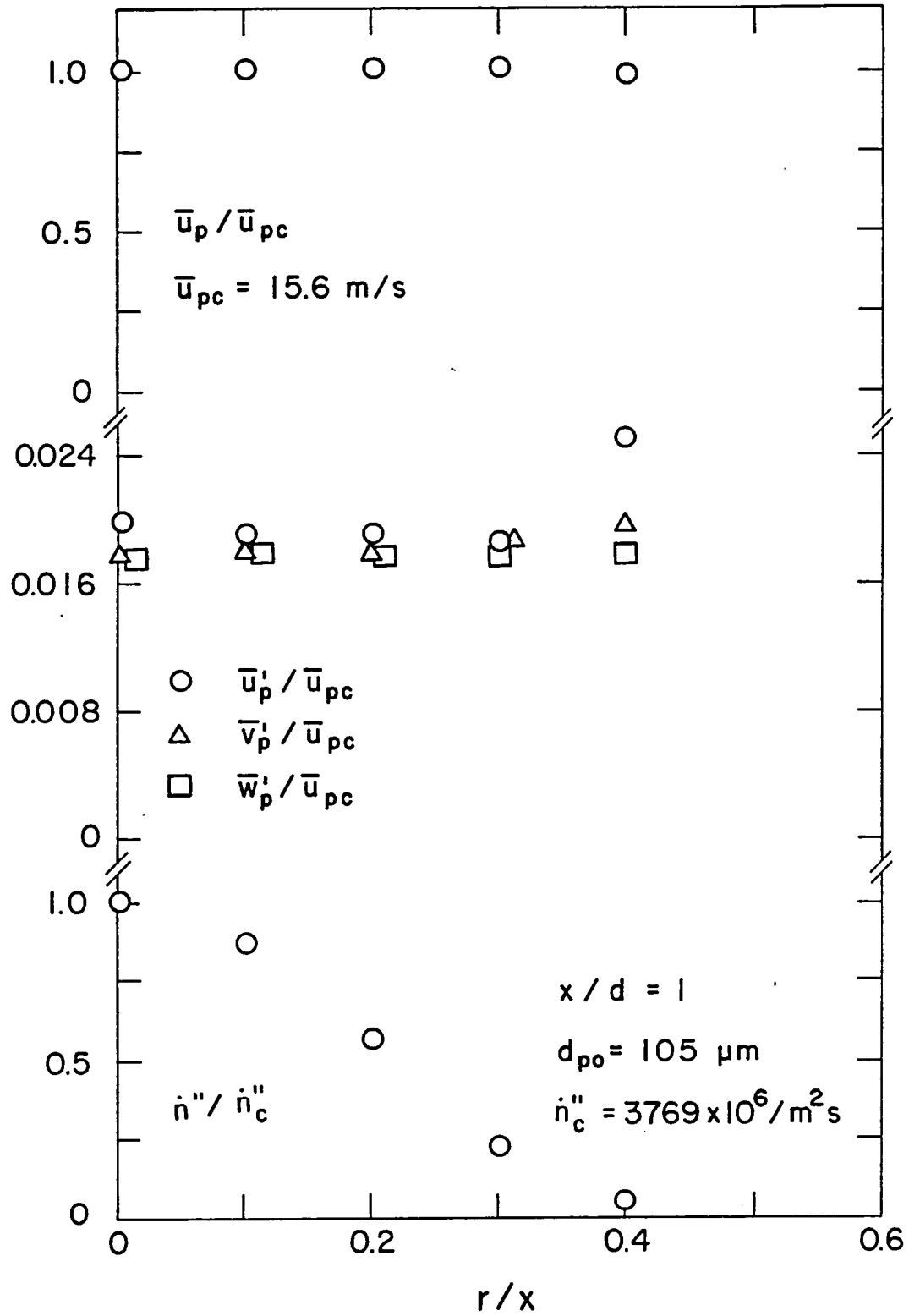


Fig. 12. Drop properties for $d_{po} = 105 \mu\text{m}$ at $x/d = 1$.

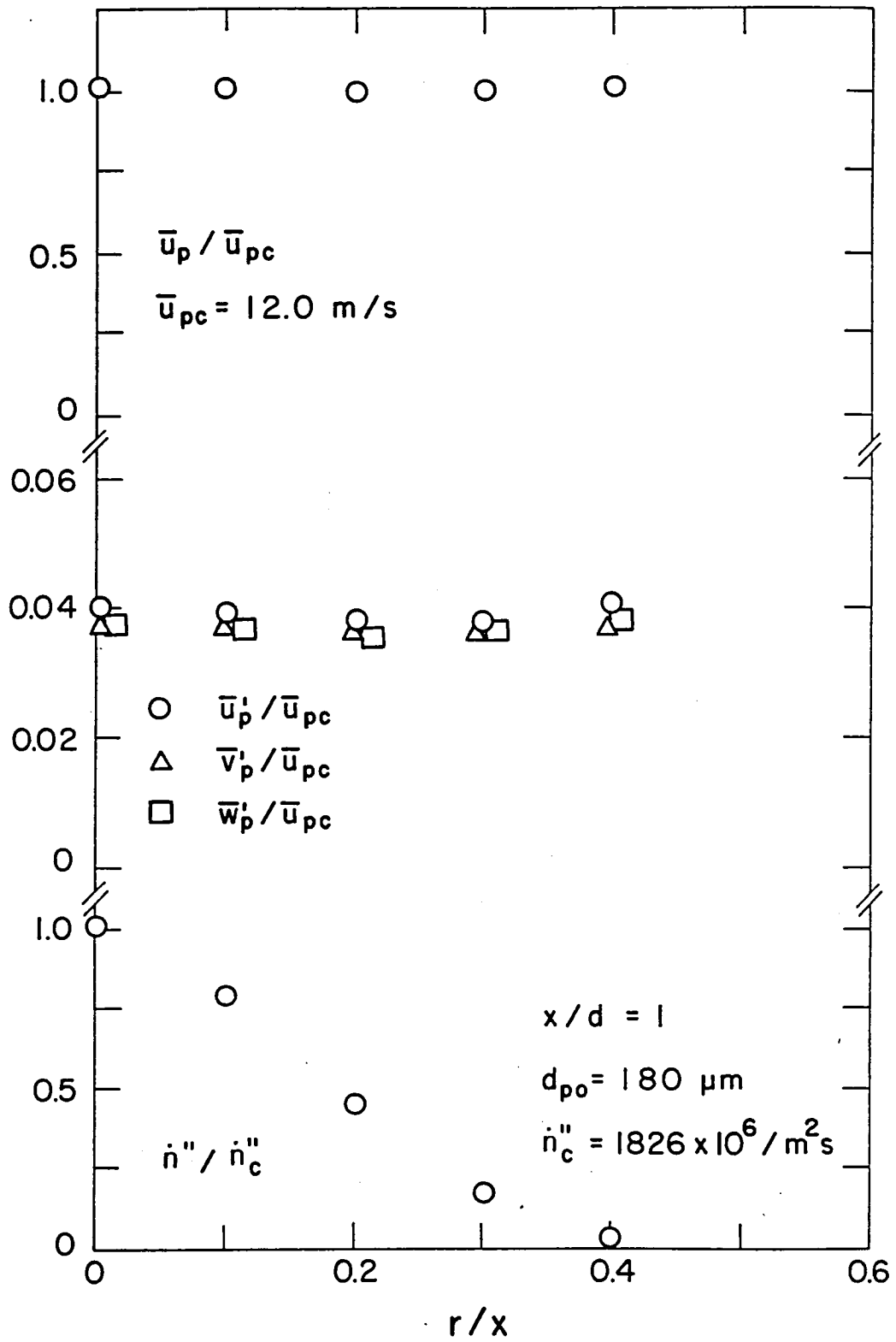


Fig. 13. Drop properties for $d_{po} = 180 \mu\text{m}$ at $x/d = 1$.

essentially the same flame. The comparison between continuous-phase predictions and the measurements will also be discussed. Mean and fluctuating velocities of the continuous phase will be considered subsequently, when spray properties are presented.

Figure 14 is an illustration of measured and predicted mean gas temperatures along the axis. Present measurements are shown along with the earlier results of Jeng and coworkers [20-22]. Both sets of measurements are virtually identical, indicating excellent reproducibility of the earlier work. This occurred in spite of increased turbulence intensities at the burner exit for the present flame, since the measurements were confined to $x/d \geq 20$, where mean properties are relatively insensitive to initial conditions. Predictions are also in reasonably good agreement with measurements, corresponding to earlier performance with essentially the same continuous-phase model. The computations of Jeng and coworkers [20-22] provide virtually the same mean temperature predictions along the axis as the present study. This implies that the increased turbulence intensity at the burner exit had little effect on the results in Fig. 14 as well.

In Figure 14, the maximum temperature along the axis is reached at $x/d = 100-120$. In the same region, the mean concentration of fuel approaches zero and we will refer to this as the flame tip. This is also roughly the mean axial extent of flame luminosity, although turbulent fluctuations cause the luminous flame region to extend up to 40% farther from the burner exit at times.

Radial profiles of mean gas-phase temperature, in the region of two-phase flow, $x/d \leq 100$, are illustrated in Fig. 15. Present measurements, the earlier results of Jeng and coworkers [20-22], and present predictions are shown. Radial distances in this, and all subsequent plots, are given as r/x , which is the radial similarity scale for turbulent jets, in order to indicate capabilities to predict flow widths directly. Near the burner exit, the maximum temperature position, which is representative of the flame position, is off-axis and only closes to the centerline near the flame tip. This is the normal structure for a turbulent diffusion flame or combusting spray [1]. Present measurements indicate a broader profile near the burner exit than Jeng et al. [21], probably due to the higher turbulence intensity at the burner exit. Predictions are in fair agreement with measurements.

Jeng and coworkers [20-22] completed composition measurements and compared them with predictions for the present flame. Since similar measurements were not made during this study, we will consider results drawn from Ref. [21], to provide a more complete picture of the flame structure and the performance of the continuous-phase analysis.

Predicted and measured variations of mean temperature and the mean mass fraction of major gas species (CH_4 , N_2 , O_2 , CO_2 , H_2O , CO and H_2) along the axis appear in Fig. 16. Predictions are shown for both the partial equilibrium and laminar flamelet state relationships, however,

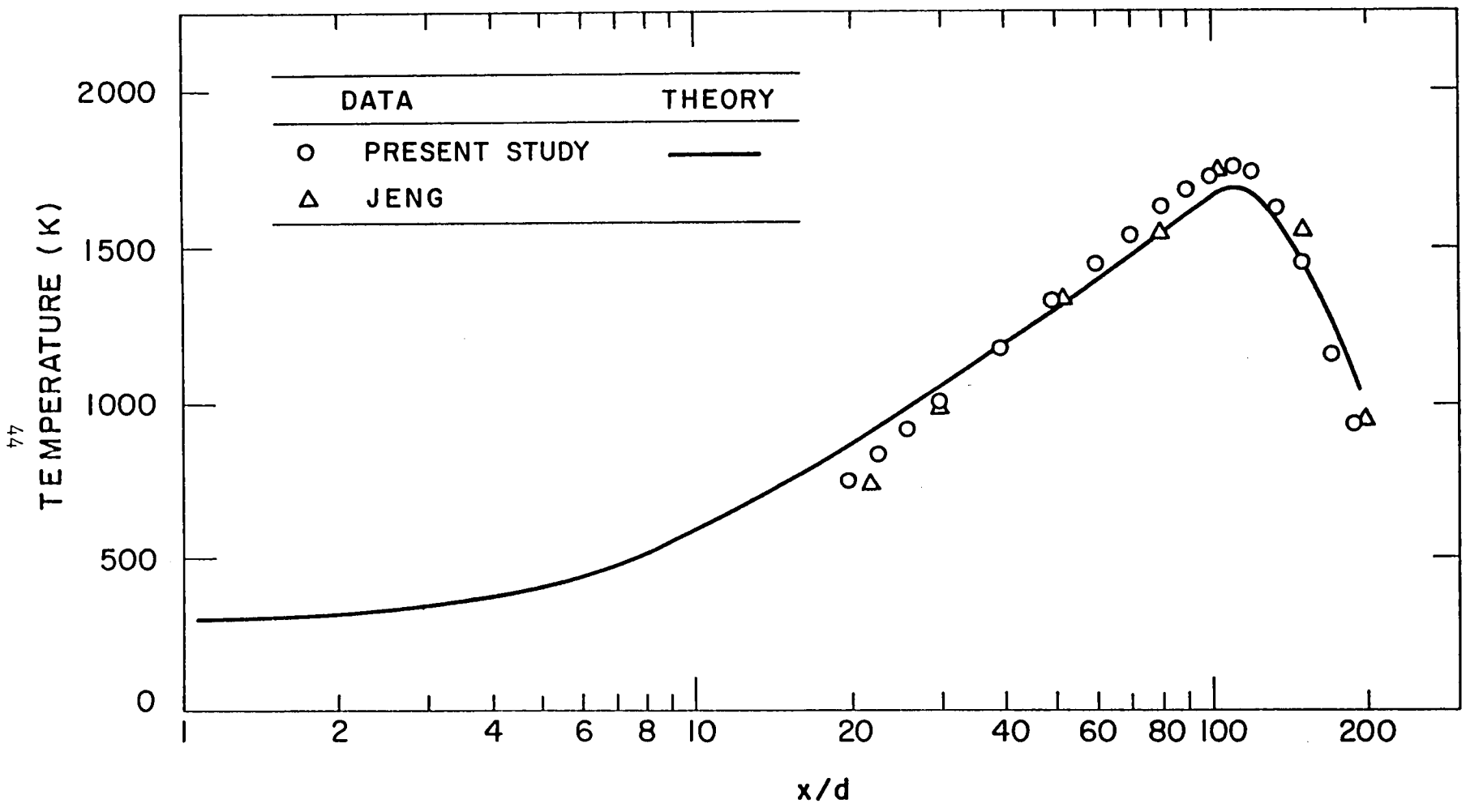


Fig. 14. Mean gas temperatures along the axis.

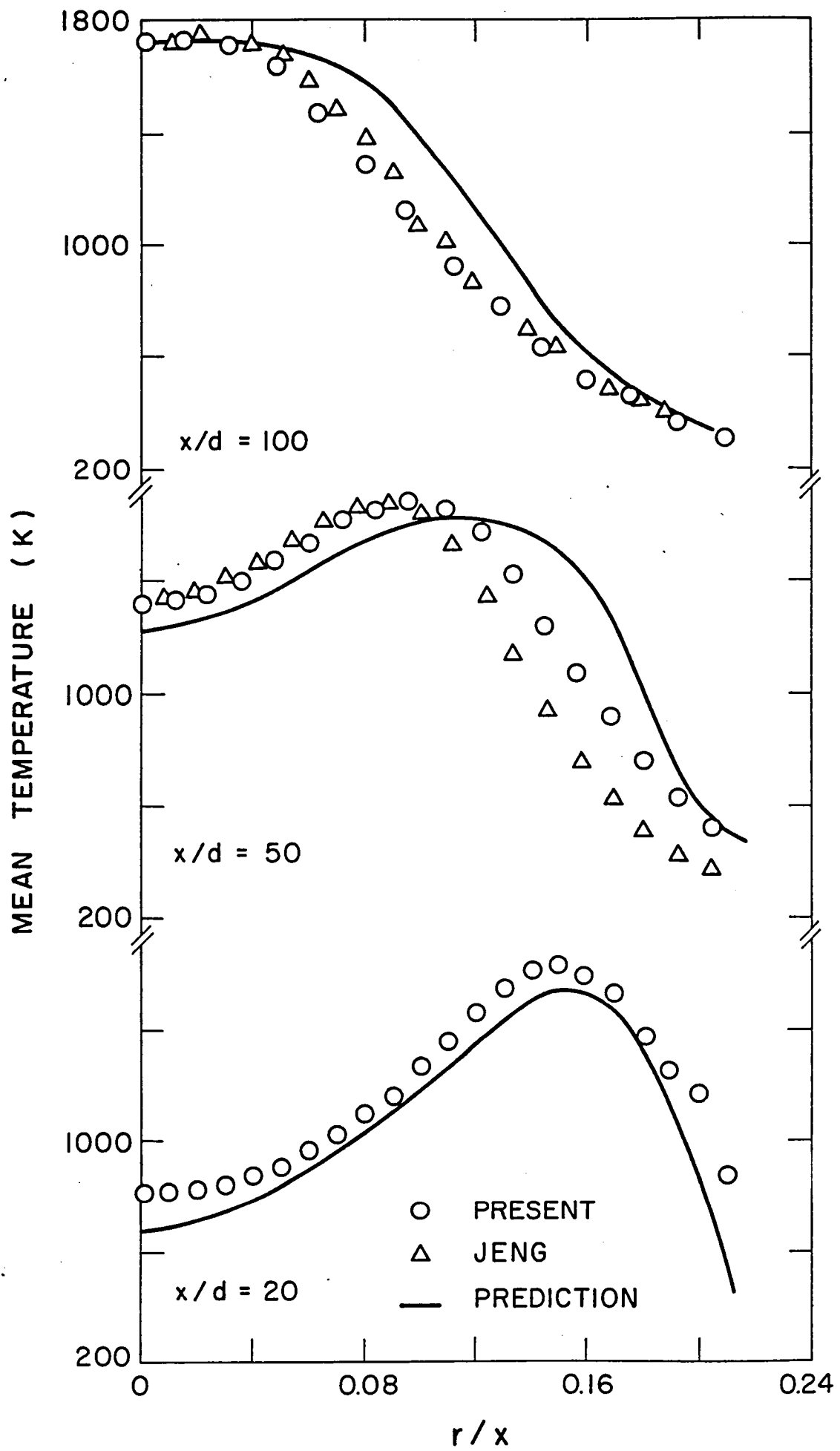


Fig. 15. Radial variation of mean gas temperature in the two-phase flow region.

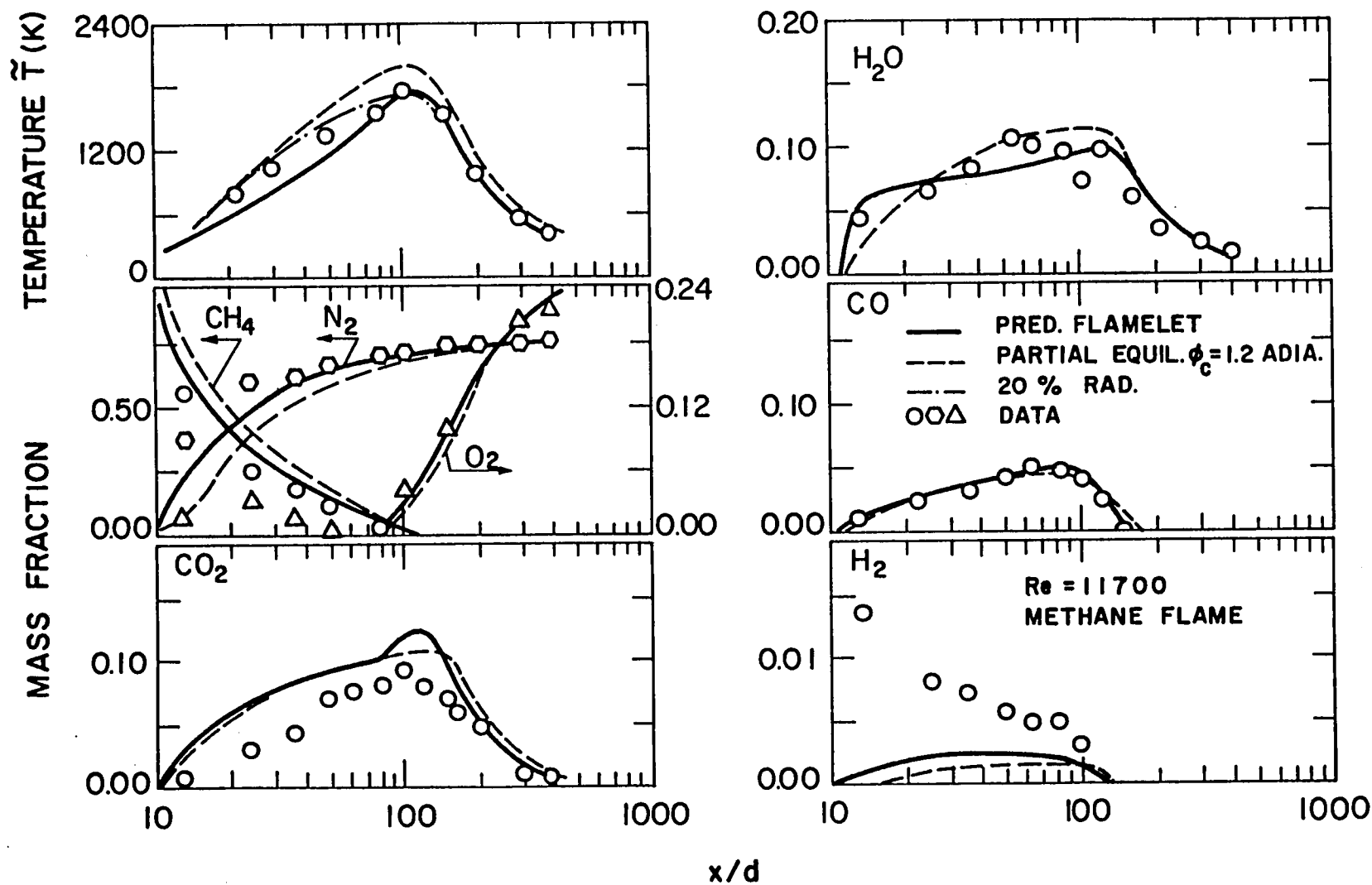


Fig. 16. Mean temperatures and species concentrations along the axis.
From Jeng and Faeth [22].

there is not much difference between these methods. The turbulent diffusion flame structure is evident with both mean fuel and oxygen concentrations overlapping somewhat near the flame tip, due to lack of complete mixing. The comparison between predictions and measurements is good, except for hydrogen concentrations which are underpredicted near the burner exit. This behavior is not a defect of the analysis, however, but is due to neglecting the presence of the hydrogen coflow required to attach the flame [21].

Radial variations of scalar properties, drawn from Ref. [21], are illustrated in Figs. 17 and 18 for axial stations $x/d = 52.2$ and 100. The comparison between predictions and measurements is fair, with a continued tendency to underestimate hydrogen concentrations, and to a certain extent, flow widths.

Comparison of predicted and measured scalar structure of the test flame, illustrated in Figs. 14-18, suggests reasonable capabilities for predicting flame structure. With this baseline established, we now proceed to consideration of the spray flames.

4.4 Structure of the Spray Flames

4.4.1 Mean Phase Velocities

The DSF analysis generally did not provide very good predictions for present test conditions. In order to avoid cluttering the figures, the DSF results will only be considered on a few plots, just to demonstrate its performance quantitatively. Similarly, the two versions of the SSF model, with and without envelope flames, yielded nearly the same results; therefore, only the latter result has been plotted, since it involves less empiricism.

Mean gas and drop velocities along the axis are illustrated in Fig. 19. Drop velocities for both sprays are shown along with SSF predictions ignoring envelope flames. The comparison between predictions and measurements is very good. Gas velocities are substantially greater than drop velocities at the burner exit, however, they rapidly decrease due to mixing with the surroundings. Near the injector, the drops have significant inertia and their velocities only gradually increase in response to the higher gas velocities. Near the tip of the flame (maximum temperature location at ca. $x/d = 100-120$, cf. Fig. 14), however, drop sizes are small and their velocities approach gas velocities. Drops in both sprays penetrate beyond the flame tip; therefore, the presence or absence of envelope flames should be a factor. However, this was found to have little effect on present computations. Use of the locally homogeneous flow (LHF) approximation, where slip between the phases is neglected [1], would be clearly inappropriate for present test conditions.

Radial profiles of mean phase velocities are illustrated in Fig. 20. The comparison between SSF model predictions and the measurements is good. Slip between the phases is most important for large drops near the injector and becomes small near the flame tip. Drop velocity measurements could only be undertaken where reasonable

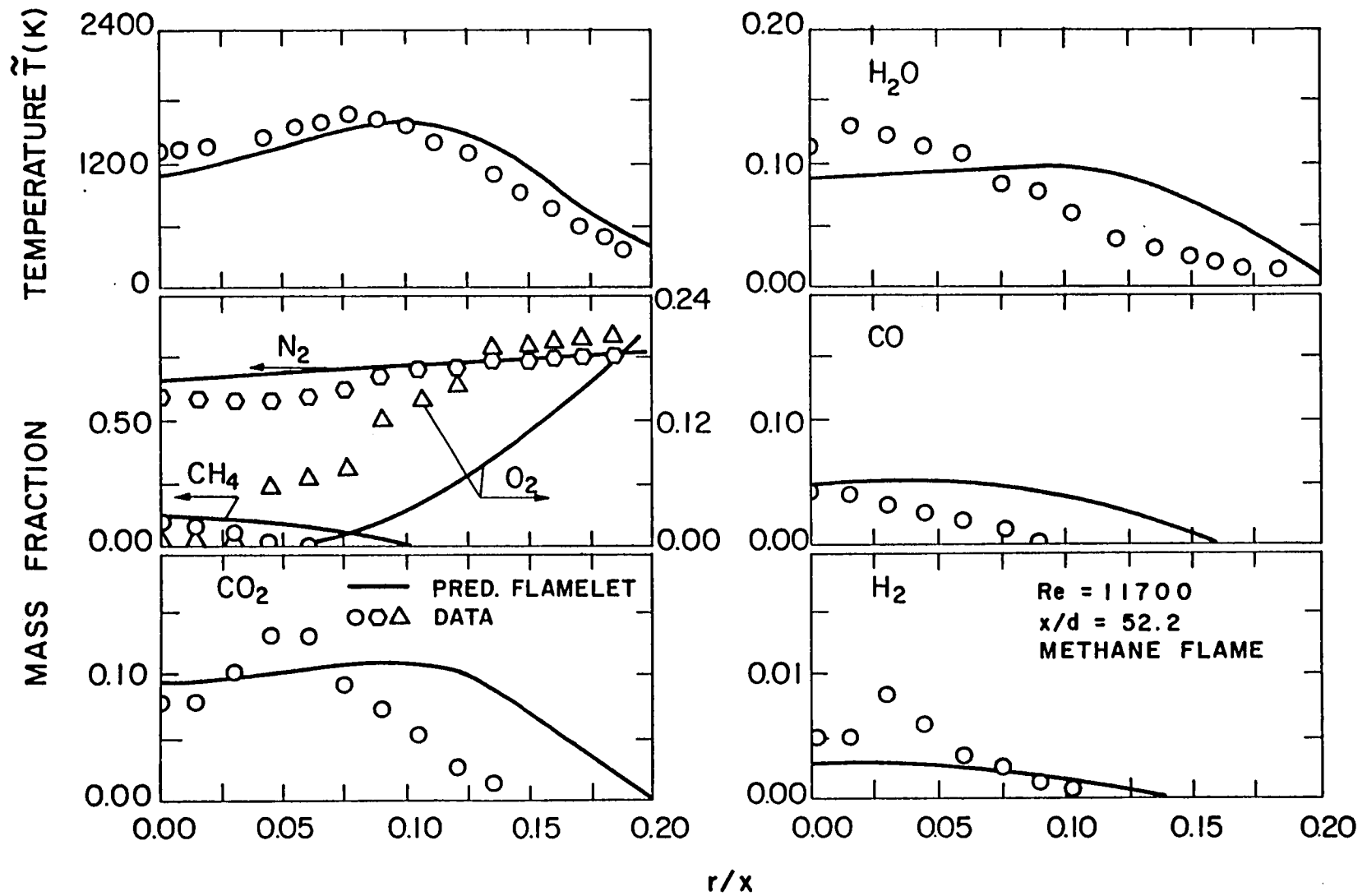


Fig. 17. Radial variation of mean temperature and species concentrations at $x/d = 52.2$. From Jeng and Faeth [22].

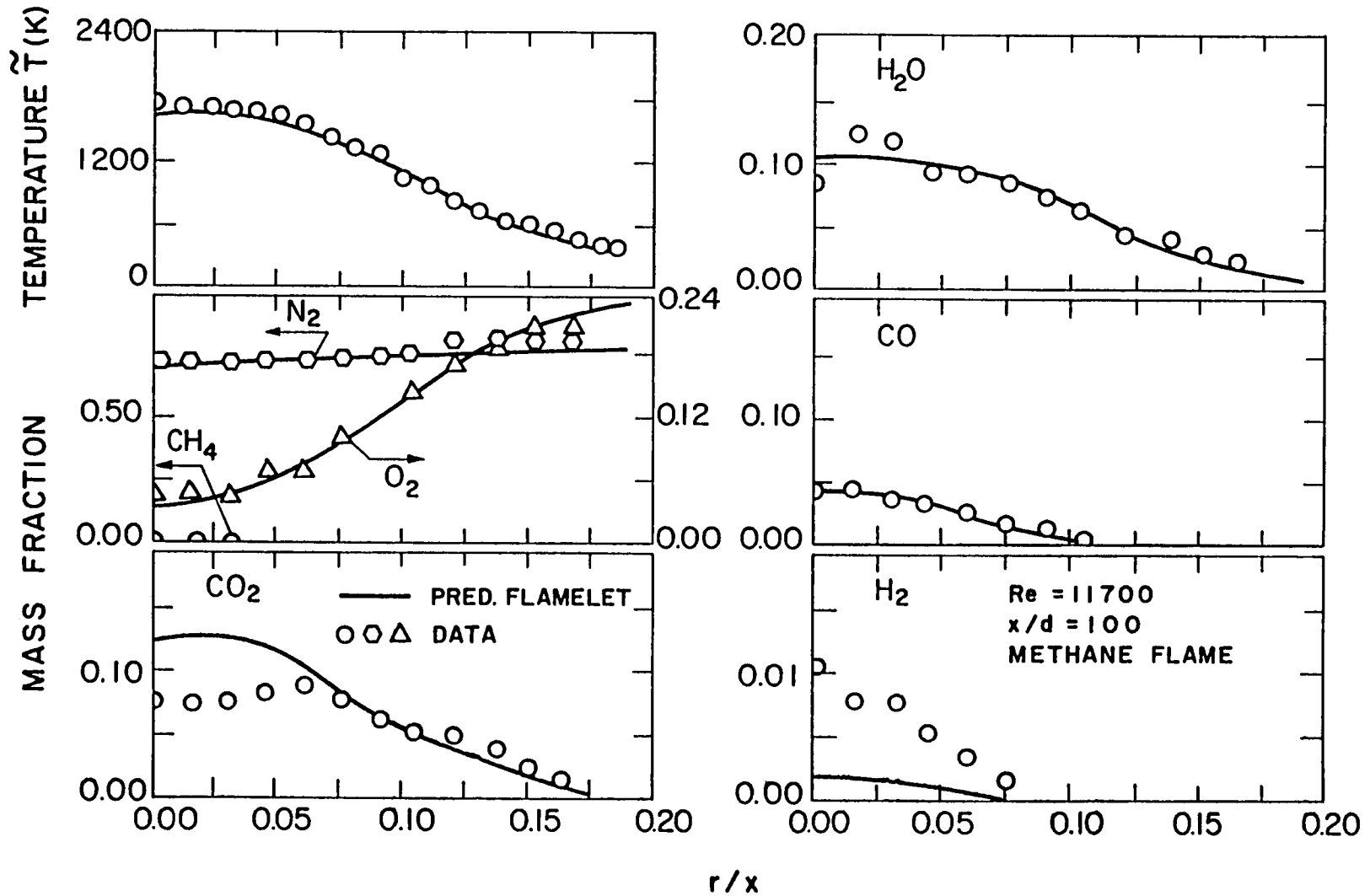


Fig. 18. Radial variation of mean temperature and species concentrations at $x/d = 100$. From Jeng and Faeth [22].

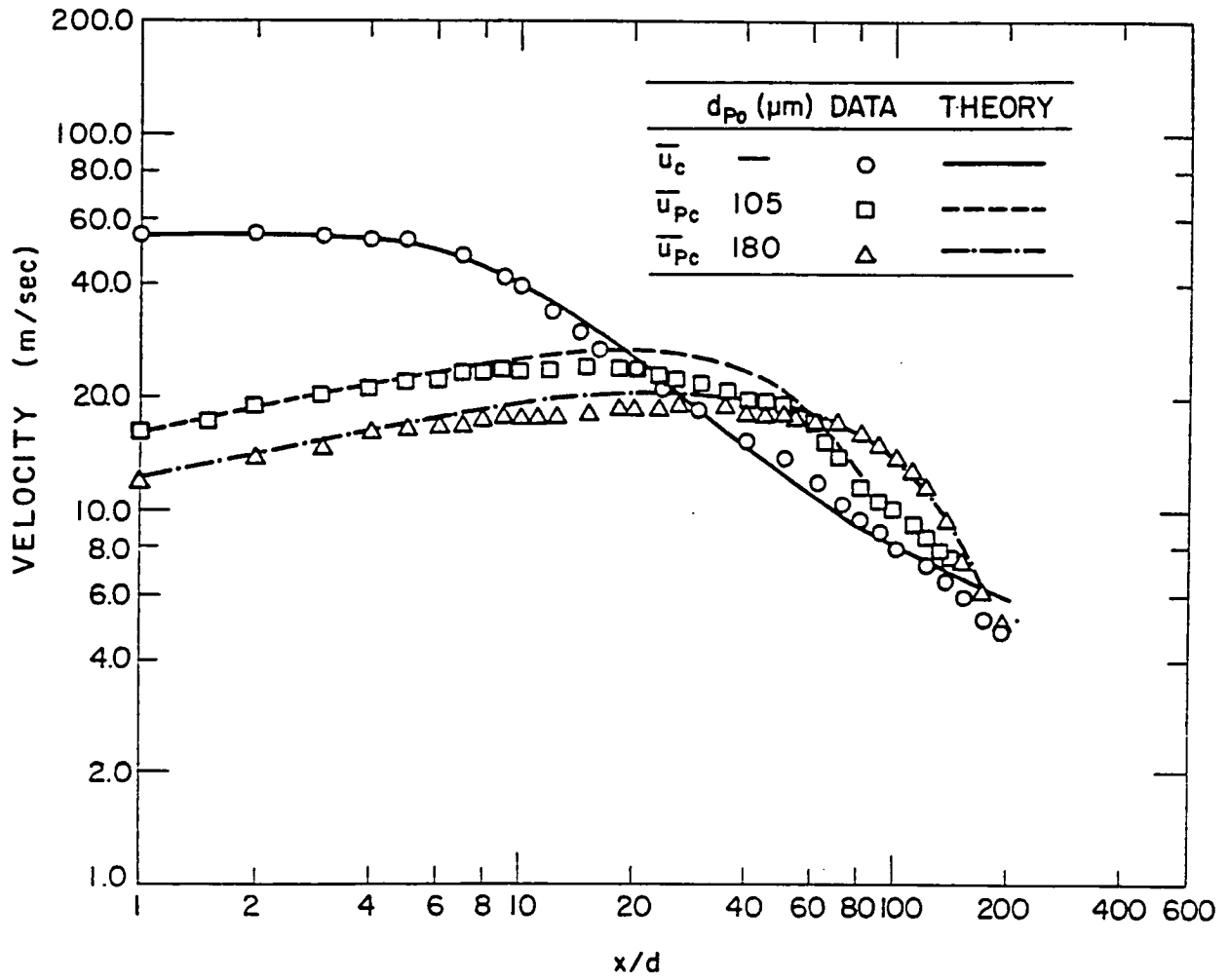


Fig. 19. Mean phase velocities along the axis.

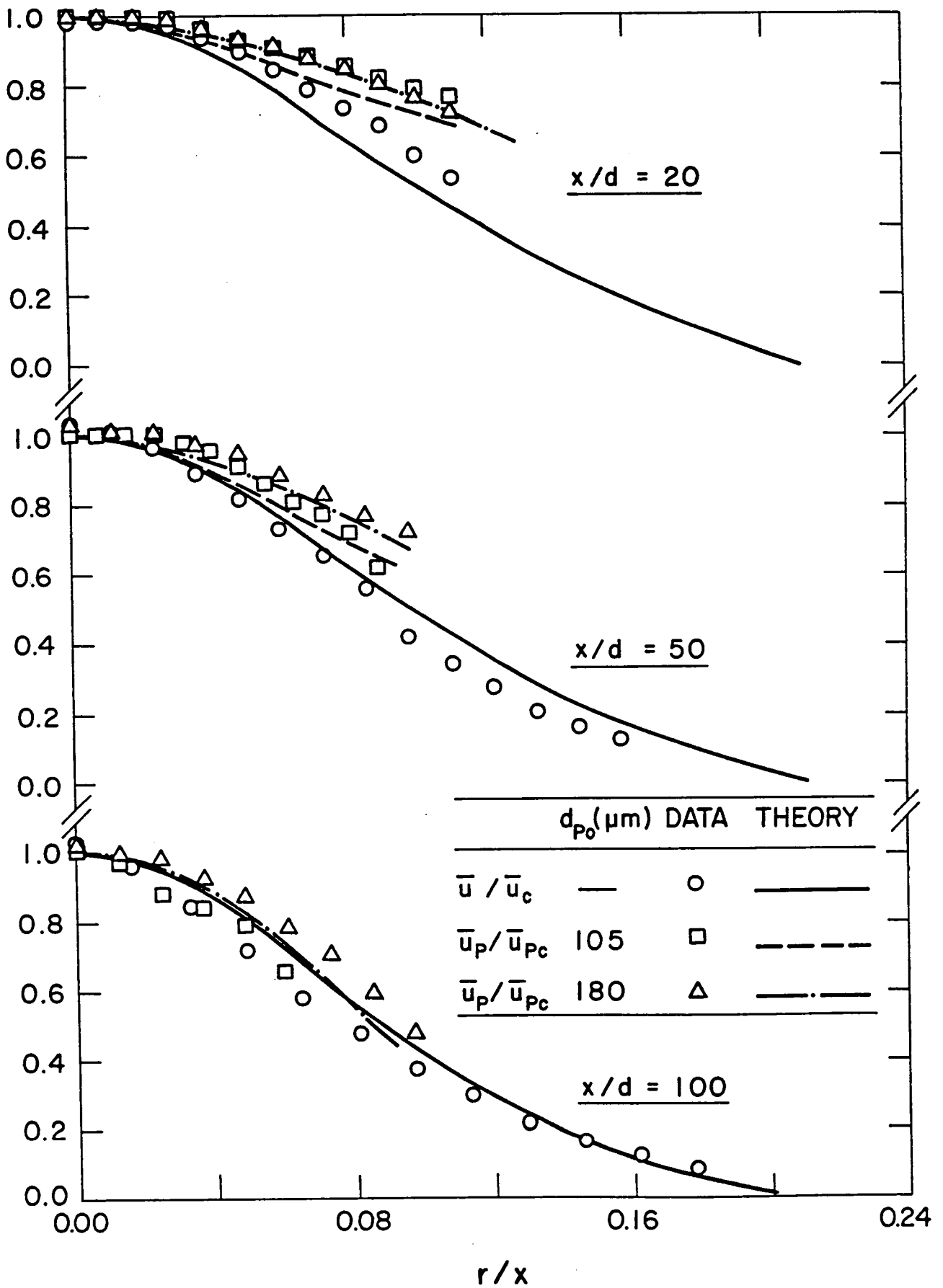


Fig. 20. Radial profiles of mean phase velocities.

numbers of drops were present; this region is roughly bounded by the flame zone since drop vaporization is high in this region, cf. Figs. 15, 17 and 18.

The overall picture that emerges from the measurements thus far is that drops are confined to the cool core of the flow and tend to evaporate quickly as the flame region is approached. Effects of slip are important in this core region, due to relatively large drop inertia. As the drops become small in the flame, however, they are more responsive and slip is less important. For present conditions, the large drops penetrate through the maximum temperature region to locations where oxygen is present.

4.4.2 Fluctuating Phase Velocities

Predicted and measured phase velocity fluctuations along the axis are illustrated in Fig. 21. Gas velocity fluctuations were estimated from the predictions assuming the anisotropy ratios generally associated with jets, e.g., $\bar{u}'^2:\bar{v}'^2 = k:k/2$ [47]. It is evident from the gas phase measurements illustrated in Fig. 21, that similar ratios were observed in the test flame. Predictions for the drop phase were found directly from the SSF analysis. Measured drop velocity fluctuations and the predictions were obtained by averaging overall drop sizes at a particular point; therefore, these values are higher than for any single size.

Predicted gas velocity fluctuations are generally within 20% of the measurements in Fig. 21, which is reasonably good in view of the relative simplicity of the continuous phase turbulence model. Velocity fluctuations decay slightly in the potential core, but then increase rapidly due to turbulence production when the shear layers merge to end the potential core region. Turbulence intensities reach a plateau as this initial development of turbulence properties ends for $x/d = 10-20$, but then increase once again as the flame tip is reached, ca. $x/d = 100$. In this region, and beyond, effects of buoyancy become important in the flow [20-22].

Drop velocity fluctuations illustrated in Fig. 21 behave somewhat differently than the gas phase. Radial drop velocity fluctuations are predicted reasonably well, which is important if turbulent dispersion of drops is to be represented accurately. Streamwise velocity fluctuations, however, are underestimated. This is similar to past observations with the SSF model and is felt to be due to the assumption of isotropic eddy properties within the SSF computations of drop/eddy interactions [1-19]. Extension of the analysis to consider anisotropy would be desirable, but would be most appropriate in conjunction with a multistress analysis of the continuous phase. This would require extensive modification of the present continuous phase analysis, and additional empiricism and model evaluation; therefore, this step was beyond the scope of the study.

Near the injector, the drop velocity fluctuations are small in comparison to gas velocity fluctuations for the results appearing in

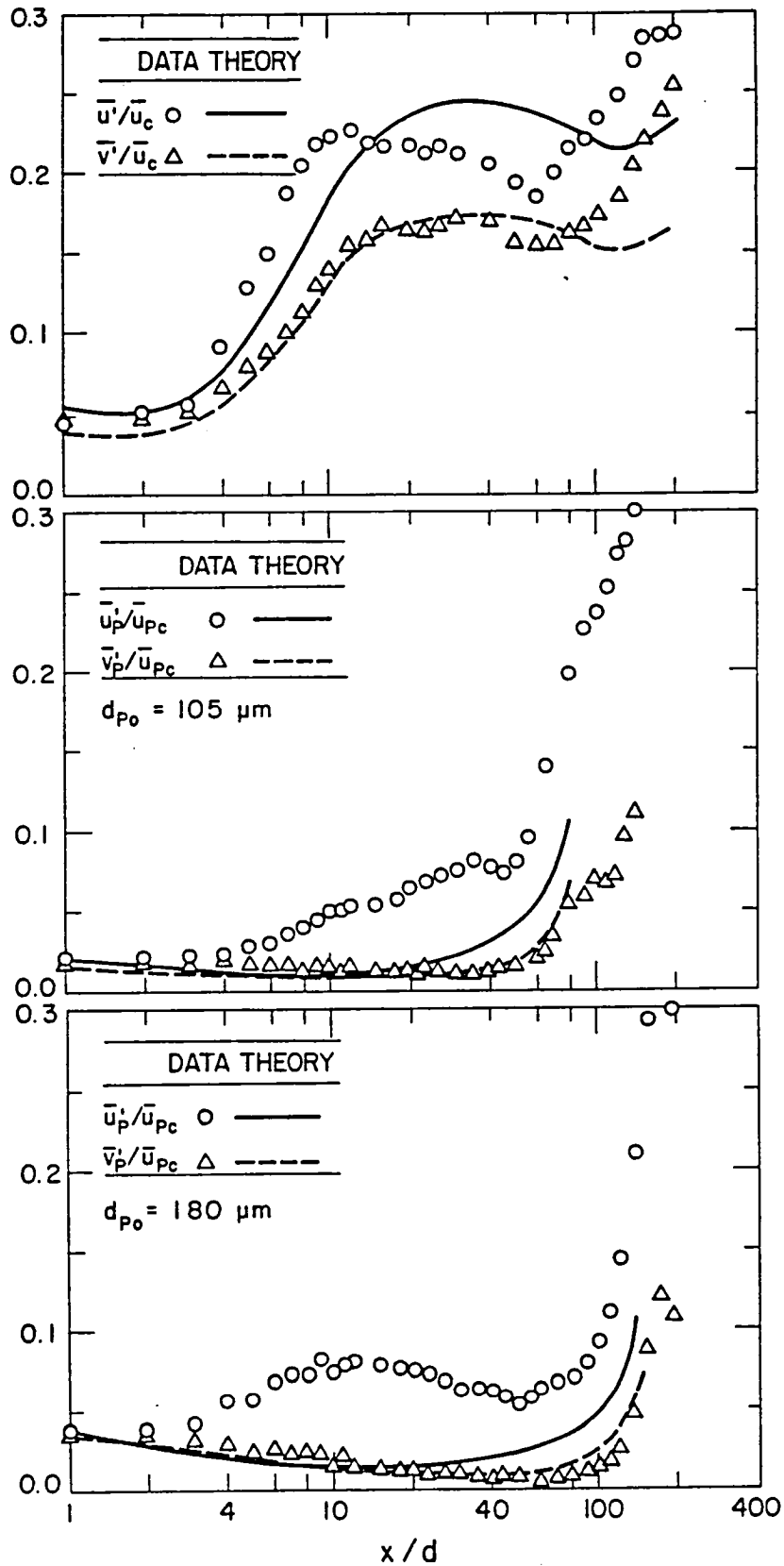


Fig. 21. Fluctuating phase velocities along the axis.

Fig. 21. This is due to the inertia of the drops, which limits their response to both mean and fluctuating gas-phase velocities. Near the flame tip, however, the drops become small due to evaporation and in the final stages of their lifetime, drop velocity fluctuations increase rapidly--approaching levels and degrees of anisotropy seen in the gas. Even under the assumption of isotropic eddy properties for computing drop/eddy interactions with the SSF model, predictions show anisotropy of drop velocity fluctuations. This behavior is due to effects of turbulent drop dispersion, which causes slower moving drops in the off-axis flow to reach the centerline. Averaging calculations over all drops sizes at a point also tends to increase predicted levels of anisotropy--behavior which is also a factor in the measurements.

Predicted and measured radial profiles of gas and drop velocity fluctuations are illustrated in Figs. 22-24. The comparison between predictions and measurements is reasonably good, except that streamwise drop velocity fluctuations are underestimated--as noted earlier. Another defect is that drops having an initial diameter of 105 μm were predicted to disappear prior to $x/d = 100$; therefore, no predictions can be shown for this position. In contrast, measurements showed that drops were present as shown in the figure.

The gas velocity fluctuations illustrated in Fig. 22 tend to be similar to observations in noncombusting jets [47]. Maximum fluctuations are observed off-axis, where turbulence production rates are highest, and decrease slightly as the axis is approached. For a jet in still air, velocity fluctuations decay continuously near the edge of the flow, where mean velocities are low. Turbulence levels at the axis tend to increase near the flame tip, however, due to effects of buoyancy.

In contrast, drop velocity fluctuations increase monotonically with increasing radial distance, cf. Figs. 23 and 24. This occurs since drops are smaller and more responsive near the edge of the two-phase flow region. Typical of the continuous phase, drop velocity fluctuations in the radial and tangential directions are nearly the same and are generally smaller than streamwise drop velocity fluctuations.

4.4.3 Drop Number Flux

Predicted and measured mean drop number fluxes along the axis are illustrated in Fig. 25 for both sprays. In this case, predictions are shown for both the DSF and SSF models (both for no envelope flames present). The SSF analysis is in quite good agreement with the measurements, except for a tendency to underestimate the length of the drop-containing region for $d_{p0} = 105 \mu\text{m}$, as noted earlier. This is very encouraging, since particle/drop fluxes are a sensitive indicator of the performance of dispersed flow models [6,10-12].

In contrast, the DSF model yields rather poor predictions of measured drop number fluxes in Fig. 25. The DSF approach vastly overestimates number fluxes along the axis, beyond the end of the

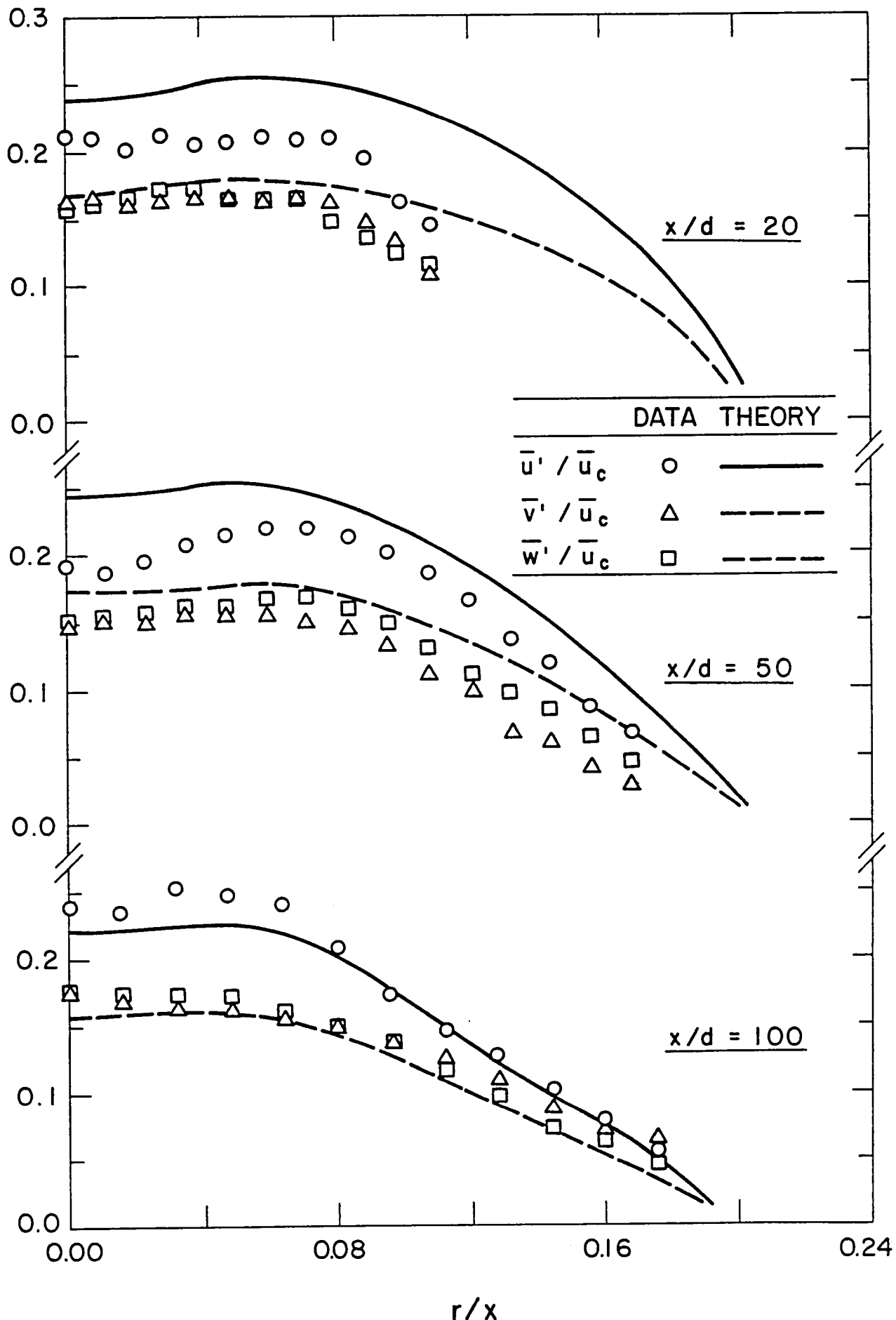


Fig. 22. Radial profiles of gas velocity fluctuations.

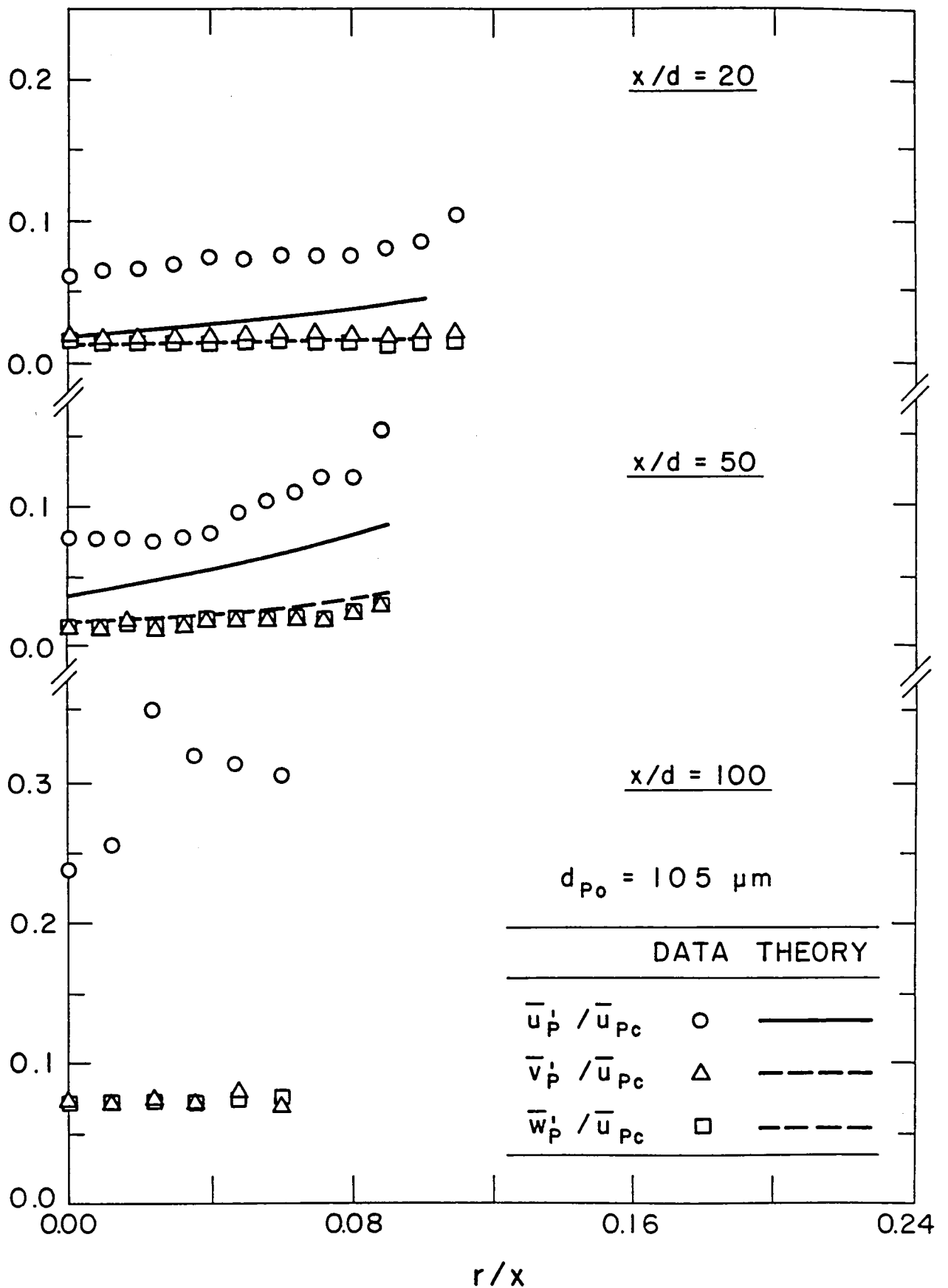


Fig. 23. Radial profiles of drop velocity fluctuations, $d_{p0} = 105 \mu\text{m}$.

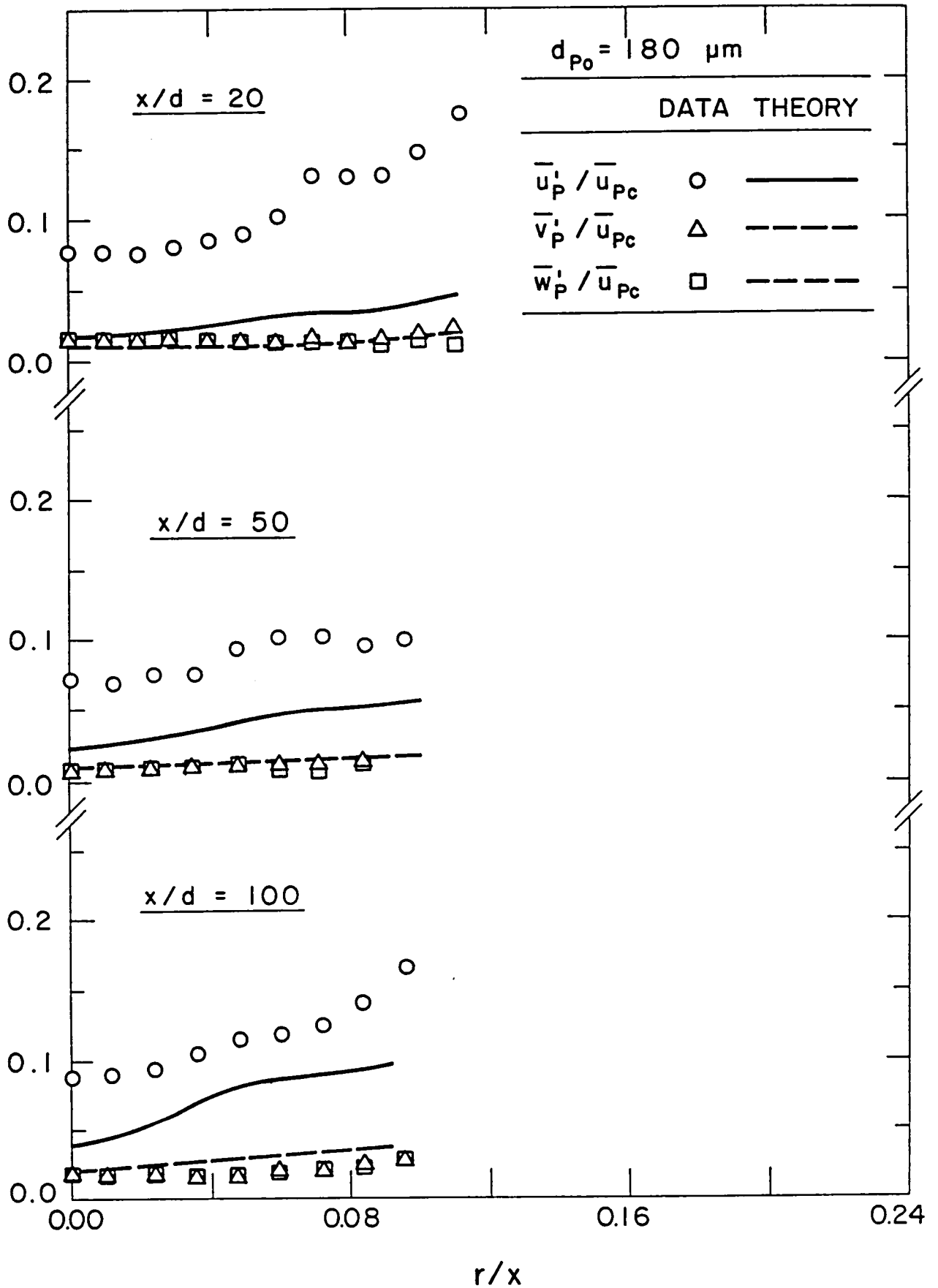


Fig. 24. Radial profiles of drop velocity fluctuations, $d_{po} = 180 \mu\text{m}$.

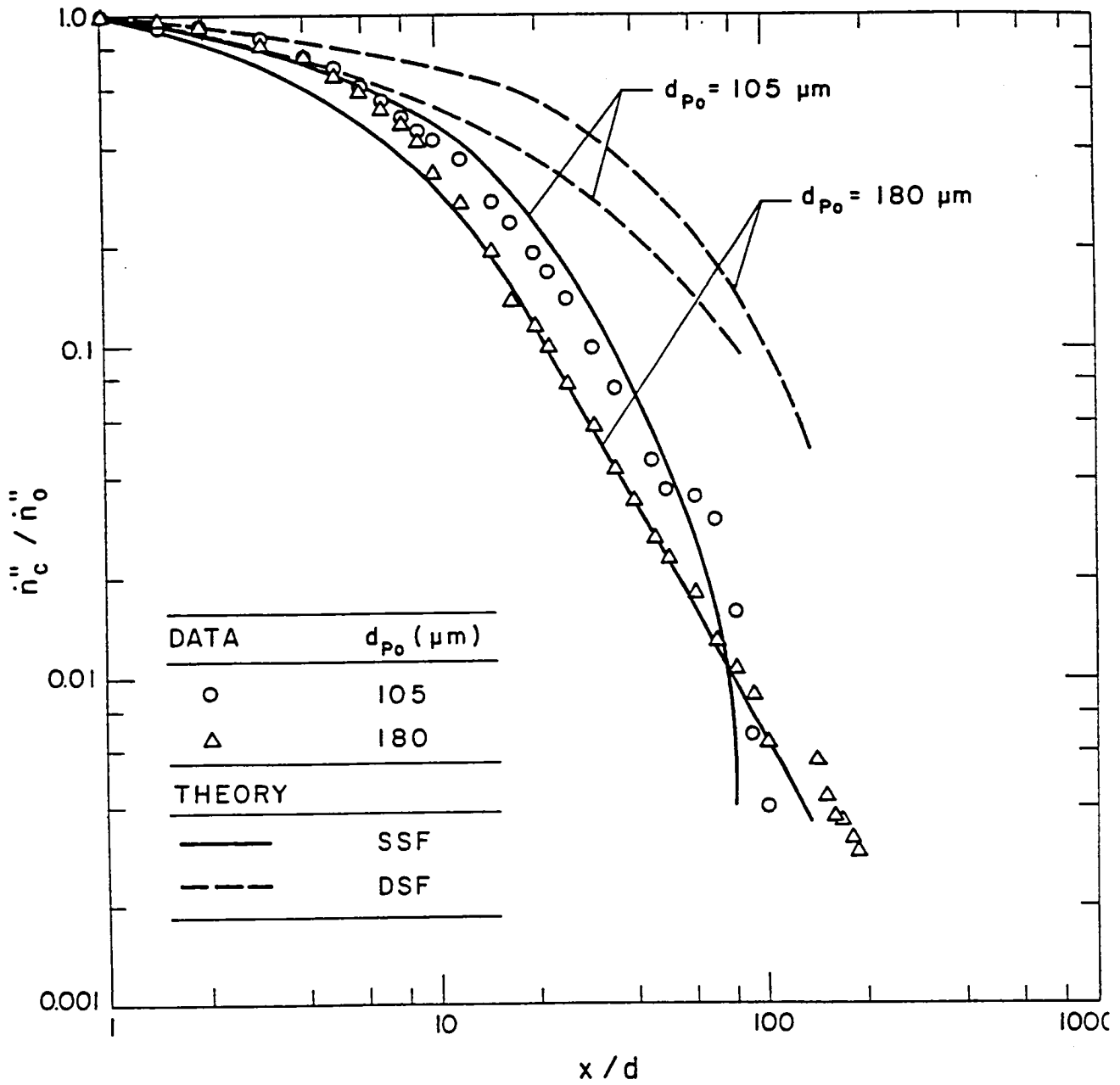


Fig. 25. Mean drop number fluxes along the axis.

potential core. The reasons for this behavior is that turbulent dispersion of drops is ignored by the DSF approach, while this phenomenon is clearly important for present test conditions. With the DSF approach, drops only move radially due to their initial radial velocity, or from radial drag due to the mean radial velocity of the flow. Both of these radial velocities are small in comparison to the radial gas-phase velocity fluctuations which are the prime contributor to effects of turbulent dispersion in this flow.*

A surprising, secondary feature of the data illustrated in Fig. 25, is that \hat{n}_g/\hat{n}_{g0} remains somewhat higher along the axis for the smaller initial drop size, in spite of effects of turbulent dispersion.** This is a result of turbulent dispersion from the initially wider number flux profile for the smaller size (cf. Figs. 12 and 13), allowing drops to diffuse to the centerline from initially off-axis positions. In contrast, the initially more concentrated large drops tend to diffuse predominantly outward in the radial direction and their concentration at the axis decreases more rapidly. This effect, due to turbulent dispersion, could hardly be anticipated (in fact, the DSF analysis gets the trend entirely wrong), but is a natural outcome of the SSF analysis when accurate initial conditions are available.

Predicted and measured radial profiles of mean drop number fluxes are illustrated in Fig. 26. Predictions are shown for both the DSF and SSF analyses, the former exhibiting poor comparison with measurements due to neglect of turbulent drop dispersion. The SSF analysis somewhat underestimates the radial spread of the drops, similar to its underestimation of streamwise drop penetration which was noted earlier. Mean drop velocities and radial drop velocity fluctuations are estimated reasonably well; therefore, this behavior is not felt to be primarily due to underestimation of turbulent dispersion. Since both the length and width of the two-phase flow region was underestimated, a more probable source of error is overestimation of drop gasification rates in the flame zone.

An interesting feature of the results illustrated in Fig. 26, is that the radial profile of drop number flux for $d_{p0} = 180 \mu\text{m}$ is somewhat broader than for $d_{p0} = 105 \mu\text{m}$. This behavior is not expected from turbulent dispersion considerations alone, where smaller drops would be expected to disperse more rapidly. In the present case, more rapid dispersion of small drops is counteracted by their more rapid

*Furthermore, the mean radial velocity is zero at an off-axis position (r/x ca. 0.08), stably, i.e., $\bar{v} < 0$ for r greater than this position and $\bar{v} > 0$ for r less than this position. This causes drops to accumulate at this radial location if the multiphase flow persists long enough [1], but the effect of accumulation is not large for present test conditions.

**Until the region near the flame tip where the smaller drops disappear more rapidly by evaporation.

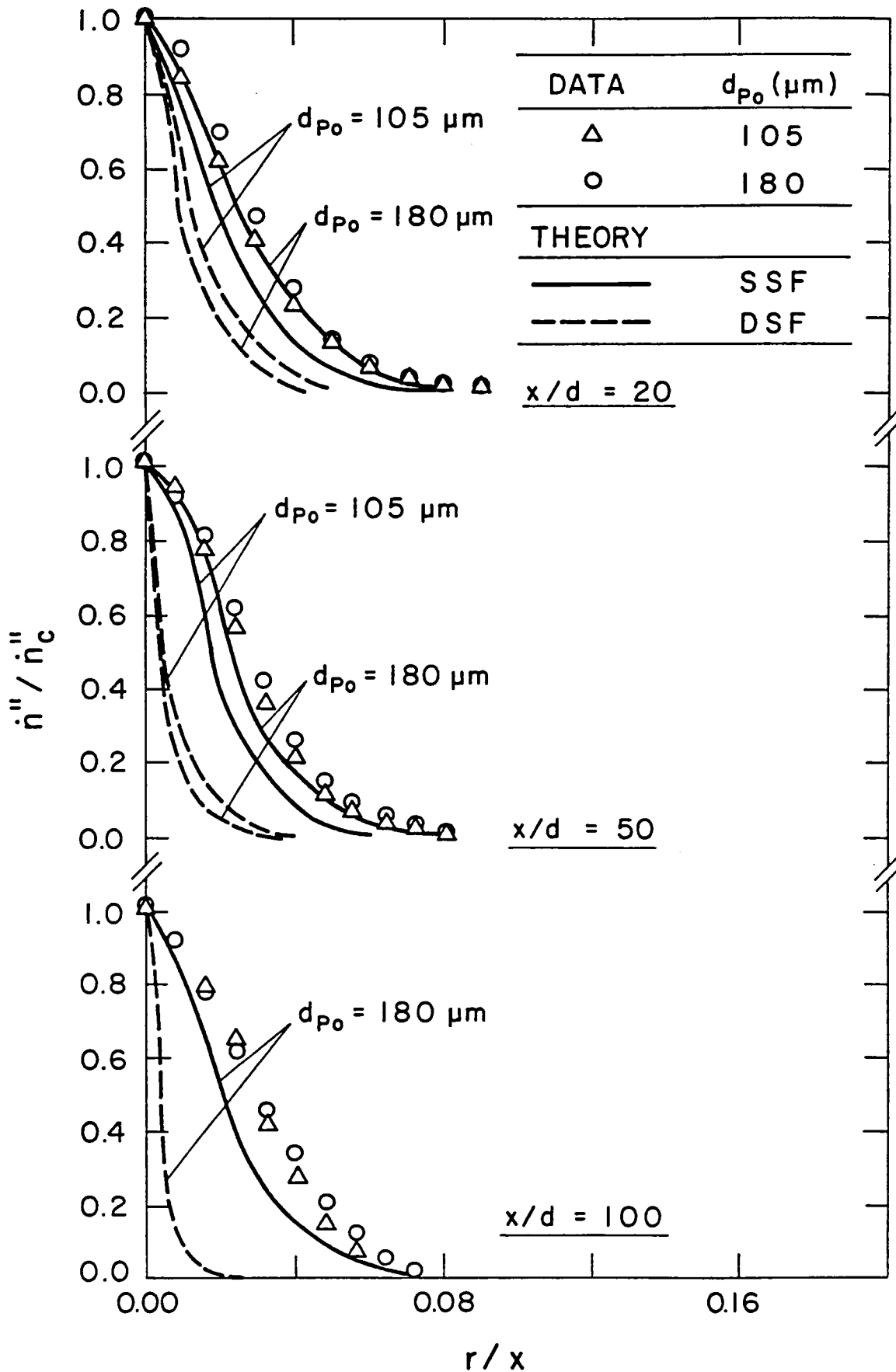


Fig. 26. Radial profiles of drop number flux.

evaporation and disappearance in the flame zone. This trend is represented reasonably well by the SSF predictions.

4.4.4 Drop-Size Distributions

Predicted (SSF analysis) and measured SMD along the axes of the two sprays are illustrated in Fig. 27. For the present, initially monodisperse, sprays, SMD decreases monotonically with increasing distance from the burner exit. This is not generally the case for polydisperse sprays, where more rapid evaporation and turbulent dispersion of small drops in the distribution generally causes the SMD to increase for a time along the axis [10-12]. The agreement between predictions and measurements is reasonably good for $d_{p0} = 180 \mu\text{m}$, but drop size is underestimated near the tip of the flame for $d_{p0} = 105 \mu\text{m}$, as noted earlier.

Predicted (SSF analysis) and measured radial profiles of SMD for the two sprays are illustrated in Fig. 28. Two positions are considered, $x/d = 50$ and 100 . Predictions are satisfactory at $x/d = 50$. At $x/d = 100$, however, drop sizes are overestimated near the edge of the flow for $d_{p0} = 180 \mu\text{m}$, while no drops are computed to be present for $d_{p0} = 105 \mu\text{m}$, in spite of observations to the contrary.

The discrepancies between predictions and measurements in both the streamwise and radial directions are largely associated with the region of the flame. Temperatures, and thus gasification rates, are highest in this region. Furthermore, drop vaporization rates increase rapidly with decreasing drop size, tending to make SMD a very sensitive indicator of model performance in this region. On balance, the present predictions are encouraging in view of the complexities of these spray-flame processes, however, additional consideration of drop transport in the region of a flame is needed to obtain more reliable predictions.

5. SUMMARY AND CONCLUSIONS

5.1 Summary

A combustng spray apparatus, operating at the limit of a dilute spray, was developed during this study. This arrangement involved a turbulent, methane-fueled diffusion flame burning in still air. Monodisperse streams of methanol drops were injected vertically upward along the axis of the flame at its base. The drop loading was sufficiently low so that flame properties were essentially unaffected by drop combustion. This configuration has a simple geometry, amenable to numerically-closed computations; initial and boundary conditions were well-defined; extensive information was available concerning the structure of the test flame; and results were available to calibrate drop transport analysis.

Test conditions were chosen to provide significant effects of finite interphase transport rates, turbulent dispersion of drops, and drop interactions with the flame zone. Two drop sizes were considered,

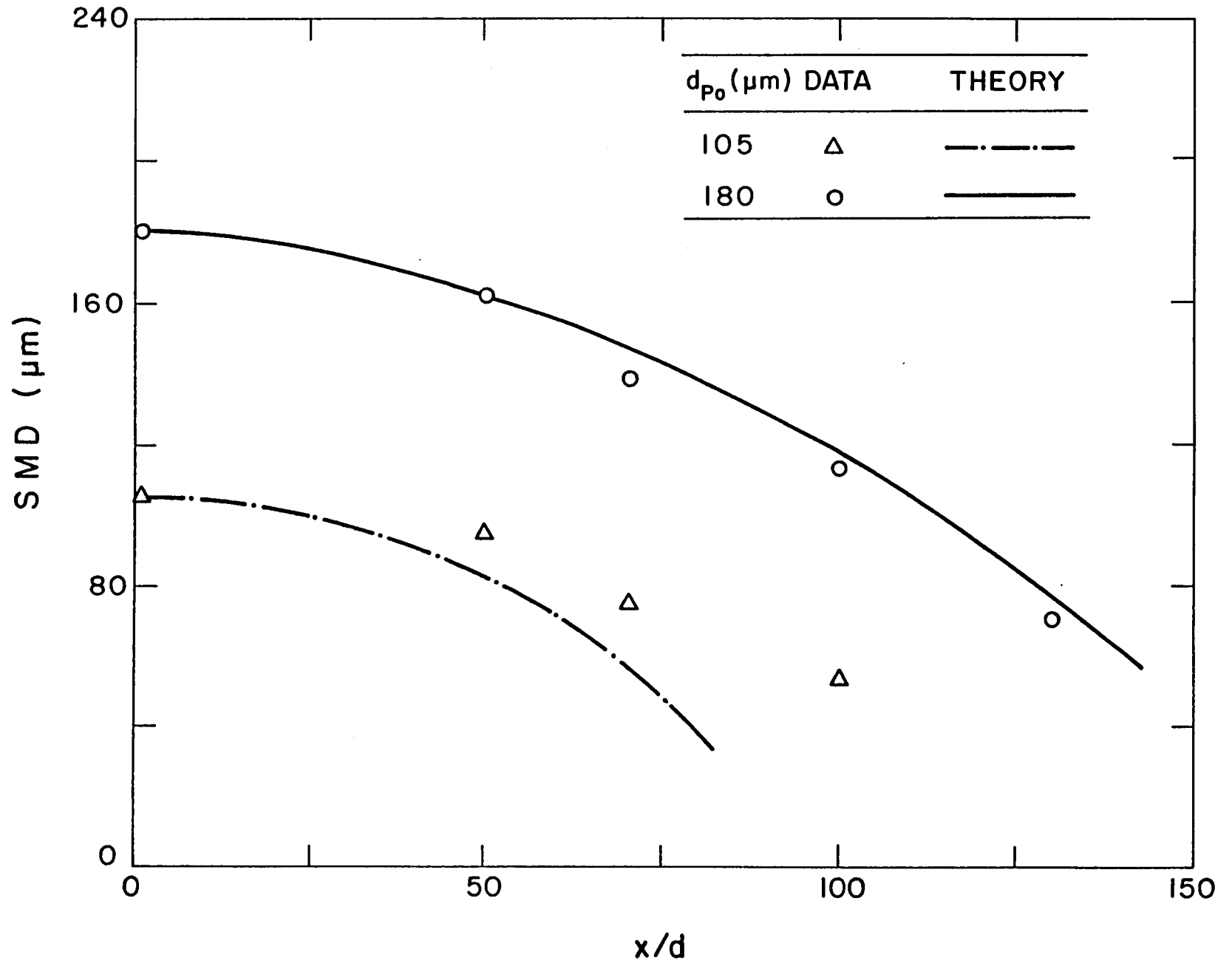


Fig. 27. SMD along the axis.

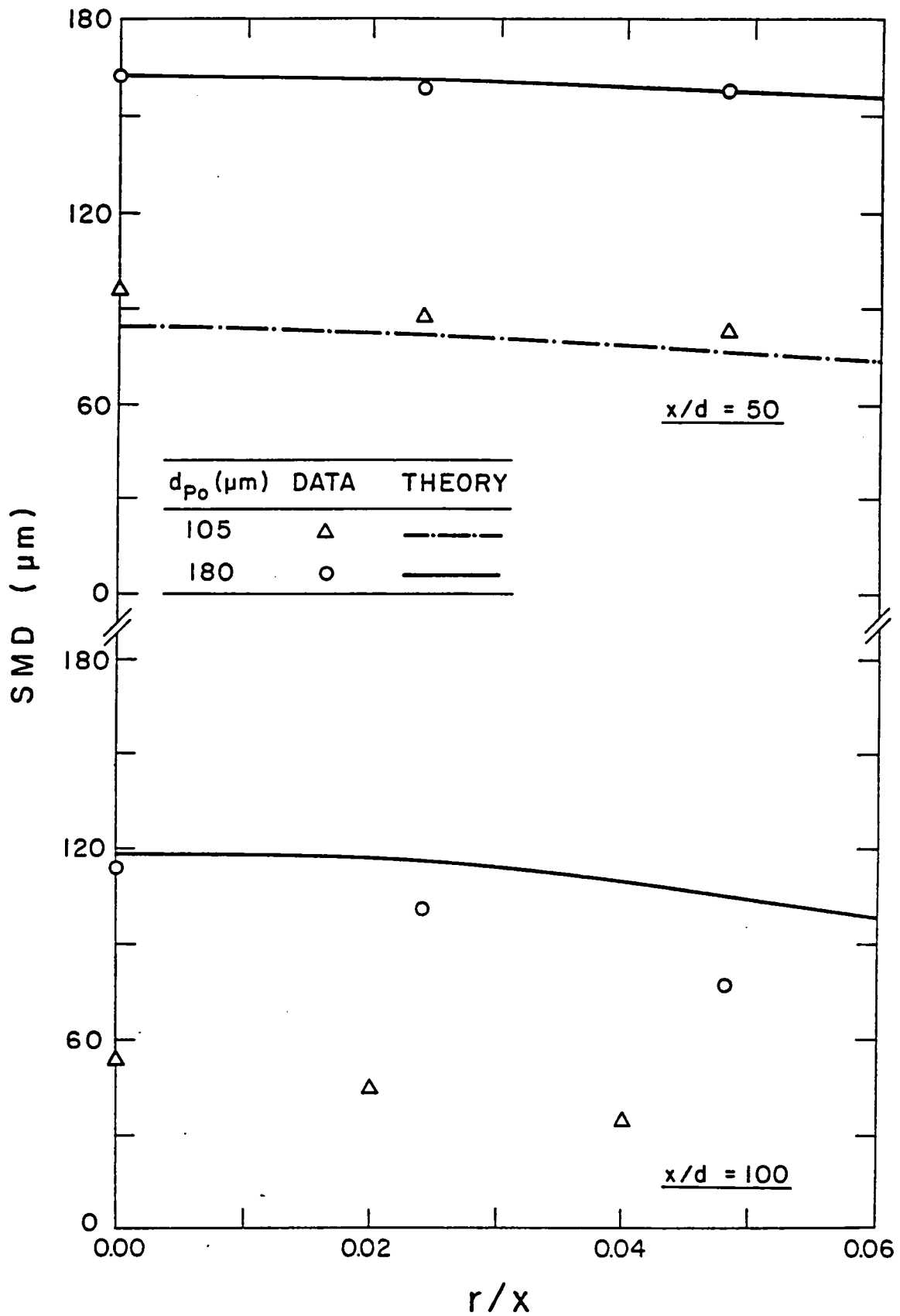


Fig. 28. Radial profiles of SMD.

having initial diameters of 105 and 180 μm . Present structure measurements included: mean and fluctuating phase velocities, mean drop number flux distributions, drop-size distributions, and mean gas temperatures. All structure measurements, as well as properties at the burner exit, are tabulated in Appendix F.

Data for calibrating transport of individual drops were obtained from single drops supported in the post-flame region of a laminar flat-flame burner. Burner reactants were methane and air; therefore, gas properties during the single drop tests were representative of the turbulent flame environment, but simplified, since effects of turbulence were absent. Drops in these tests had initial diameters in the range 2000-3000 μm . While these sizes were much greater than in the turbulent flame tests, drop Reynolds numbers for the calibration tests and the sprays were comparable.

Analysis of the combusting sprays was undertaken to help interpret the measurements and to initiate evaluation of models of the process. Two methods typical of current spray analysis were considered: (1) a deterministic separated flow (DSF) model, where effects of finite interphase transport rates are considered, but drop-turbulence interactions and turbulent dispersion of drops are ignored; and (2) a stochastic separated flow (SSF) model, where effects of finite interphase transport rates, drop-turbulence interactions, and turbulent dispersion of drops are considered using random sampling for turbulence properties in conjunction with random-walk computations for drop motion.

Analysis of the continuous phase for both spray models was based on a k - ϵ - g turbulence model, which provided a reasonably good description of the structure of the test flame during earlier work in this laboratory [20-22]. The governing equations were in Favre-averaged form. The conserved-scalar method was used to find scalar properties, along with the laminar flamelet method for relating scalar properties to mixture fraction in turbulent flames.

5.2 Conclusions

Major conclusions of the study are as follows:

1. The DSF model, which ignores drop-turbulence interactions, was not very successful for present test conditions. The main defect was a significant underestimation of drop spread rates due to neglect of turbulent dispersion of drops. In spite of its popularity [1], this approach appears to have limited value for analyzing practical combusting sprays.

2. The SSF model gave encouraging predictions of current test results, with all empirical parameters used in the turbulence model fixed (based on earlier measurements for noncombusting jets) and drop transport calculations calibrated by single-drop tests. Largest discrepancies involved streamwise drop velocity fluctuations, which were underestimated, and the transport rates of small drops in the flame zone, which were overestimated. Extension of current methods to consider anisotropic continuous-phase turbulence properties and further study of drop transport rates in flames appears warranted. Based on encouraging results for particle-laden jets [2-7], nonevaporating sprays [8-11], evaporating sprays [12] and now combusting sprays, the SSF methodology appears to be an effective method for analyzing turbulent sprays. Continued development of this method appears to be justified.
3. The distinction between the presence or absence of envelope flames did not modify predictions appreciably since drops primarily evaporated in the core of the flow where oxygen concentrations are low. Further study of envelope flame effects is needed, however, since present work is not definitive and drops penetrated the flame zone for present test conditions.
4. The present experiment proved to be useful for studying drop transport and dispersion in turbulent flames and should be considered by others. The parabolic flow is attractive for numerically-closed computations, initial conditions are readily measured, and flow properties are conducive to reasonably reliable measurements. Newly-available methods for simultaneous drop size and velocity measurements could be fruitfully exploited in this flow.

APPENDIX A

EXPERIMENTAL UNCERTAINTIES

A.1 Phase Velocities

There are two main sources of uncertainties in the LDA measurements of phase velocities: bias errors, and general experimental uncertainty. Each error source will be considered in the following.

Bias Errors

Bias errors in velocity determinations using LDA arise from several sources [48]: (1) directional ambiguity, due to the inability of a stationary or slowly translating fringe pattern to provide an indication of the direction in which particles are crossing the fringes; (2) directional bias, due to particles crossing the measuring volume at a small angle with respect to the plane of the fringes so that an insufficient number of fringes are crossed to be processed; (3) concentration bias, due to varying particle concentrations in components of a mixing flow; (4) velocity bias, due to the fact that for uniform seeding, more high velocity particles cross the measuring volume than low velocity particles; and (5) gradient bias, due to variations in flow velocity. Each of these sources of biasing are considered in the following.

The present tests employed frequency shifting which eliminated errors due to directional ambiguity. The effective frequency shift level, after electronic mixing, was set at each location so that even a particle moving upstream at the maximum local velocity would be crossed by fringes which move even faster in the upstream direction. Operated in this manner, frequency is a single-valued function of velocity over the range of interest and no directional ambiguity occurs [48].

Directional bias was also eliminated by frequency shifting. The worst case is a seeding particle moving somewhat upstream to the fringe plane while crossing the measuring volume. However, since the fringes are effectively moving upstream at velocities high enough to prevent directional ambiguity, sufficient fringe crossings were available at each point in the flow to yield a detectable signal (8-32 fringe crossings were used for processing).

Concentration bias was not a factor for drop velocities, since only drop velocities were sought and measured. Concentration bias can influence gas velocity measurements, if the burner and ambient gas are not seeded to the same degree. This was a problem near the burner exit, since the hydrogen coflow was not seeded, however, measurements in this region related primarily to burner gas properties so the effect does not materially influence present results. The tactic used to reduce effects of concentration bias was to seed both burner and ambient gas. Similar to past practice [1-18], the detector output was observed and ambient seeding was adjusted to eliminate any observed

effects of signal intermittency due to lack of particles in the ambient flow.

Velocity bias can occur when particles averages are used, since more high-velocity particles pass through the measuring volume per unit time. This effect was eliminated for gas velocities by operating the system at high signal rates (500-5000 Hz) and time-averaging the output, as discussed by Durst et al. [48]. Particle-averages were measured for drops; therefore, drop velocities have velocity bias. This represents no problem, however, since theoretical results were obtained in the same manner.

The final source of biasing is gradient biasing, which could introduce errors in present measurements. These biases can be estimated using the analysis reported by Kreid [49]. For this analysis, only velocity gradients in the radial direction are considered and all seeding particles crossing the measuring volume are assumed to be recorded--independent of any directional bias, which has already been shown to be small. The measuring volume is assumed to be small, so that higher-order terms in the Taylor series expansion of mean velocity (expanded from the center of the measuring volume) can be ignored. Then the difference between the measured mean and fluctuating velocities, \bar{u}_t and \bar{u}'_t , and the actual values of the flow, \bar{u} and \bar{u}' , are

$$|\bar{u}_t - \bar{u}| = \frac{\ell^2}{6} \frac{\partial^2 \bar{u}}{\partial r^2} \quad (\text{A.1})$$

$$|\bar{u}'_t{}^2 - \bar{u}'^2| = \frac{\ell^2}{3} \left(\frac{\partial \bar{u}}{\partial r} \right)^2 \quad (\text{A.2})$$

where ℓ is the half-width of the measuring volume in the radial direction.

Applying Eqs. (A.1) and (A.2), after estimating gradients from the measurements, indicates gradient broadening errors less than 1% for present tests--for both phases.

Jeng [20], extended considerations of gradient broadening to consider this effect for two orthogonal gradients--neglecting only the gradient in the streamwise direction, since it is small. He reached the same conclusion for the gas phase, e.g., gradient broadening errors were less than 1%.

Uncertainty Estimates

The uncertainty analysis procedures of Moffat [50] are adopted to estimate experimental uncertainties. In this case, we consider an output variable V , which is a function of several, n , measured variables, v_i , as follows:

$$V = V(v_1, v_2, \dots, v_n) \quad (\text{A.3})$$

The v_i are subject to uncertainties, Δv_i , and we wish to determine the resulting uncertainty in V , e.g., ΔV . The Δv_i and ΔV are defined somewhat arbitrarily, but consistently. They can be the expected standard deviation of these quantities or some percentage of the confidence interval for these quantities, e.g., the 95% confidence interval is most frequently chosen [50]. In the following, we will use the latter definition. Based on these definitions, Moffat [50] finds

$$\frac{\Delta V}{V} = \left[\sum_{i=1}^n \left(\frac{\partial \ln V}{\partial v_i} \Delta v_i \right)^2 \right]^{1/2} \quad (\text{A.4})$$

Equation (A.4) will be used to estimate relative uncertainties in the following.

In considering uncertainties in gas velocity measurements, we ignore positioning errors, since this only influences the position where points are plotted and this accuracy has been stated already. Furthermore, all orientations of the laser beams were measured with positions of the experiment and optics fixed. It is felt that optical alignment was sufficiently good so that rotation of the laser beams did not shift the location of the measuring volume significantly, e.g., the detector was fixed and optical alignment was optimized to maintain good signal-to-noise ratios at all beam angles. As a result, the mean velocity measurement only depends on the overall calibration factor, K , between the electrical signal and velocity and the time-averaged electrical signal itself, E , allowing for frequency shift, e.g.,

$$\bar{u} = K \bar{E} \quad (\text{A.5})$$

Applying Eq. (A.4) to Eq. (A.5) yields

$$\frac{\Delta \bar{u}}{\bar{u}} = \left[\left(\frac{\Delta K}{K} \right)^2 + \left(\frac{\Delta \bar{E}}{\bar{E}} \right)^2 \right]^{1/2} \quad (\text{A.6})$$

The overall calibration factor K was checked using a rotating disk and is estimated to have a relative uncertainty of 2%. The uncertainty of \bar{E} was estimated from measurements of several samples at a worst-case condition using representative operation procedures. The uncertainty is taken as two times the standard deviation of these samples (roughly the 95% confidence interval) to yield an estimate of 3%. Substituting these estimates into Eq. (A.6) then yields an uncertainty for mean velocities of 4%.

Similar considerations hold for velocity fluctuations, except that in this case processing differed since the true rms meter was in the circuit. Then

$$\bar{u}', \bar{v}', \bar{w}' = K (\bar{e}_u, \bar{e}_v, \bar{e}_w) \quad (\text{A.7})$$

where \bar{e}_i is the averaged output of the true rms meter. The uncertainty in K is unchanged while the worst-case estimate of the uncertainty in \bar{e}_i is 5%. This yields an uncertainty in individual velocity fluctuations of 5%.

Errors in quadratic quantities, like k are larger. In the case of k we have

$$k = \frac{1}{2} K^2 (e_u^2 + e_v^2 + e_w^2) \quad (\text{A.8})$$

Applying Eq. (A.4) to Eq. (A.8) then yields

$$\frac{\Delta k}{k} = 2 \left[\left(\frac{\Delta K}{K} \right)^2 + \frac{\bar{e}_u^2 \Delta e_u^2 + \bar{e}_v^2 \Delta e_v^2 + \bar{e}_w^2 \Delta e_w^2}{(\bar{e}_u^2 + \bar{e}_v^2 + \bar{e}_w^2)^2} \right]^{1/2} \quad (\text{A.9})$$

Based on the uncertainties in K and the \bar{e}_i , discussed above, the uncertainty in k is roughly 9%.

Considerations for drop velocities are similar to those of gas velocities, except the results for individual drops were summed to find appropriate averages. Based on several samples at typical operating conditions, the uncertainties in \bar{E} and \bar{e} were 3 and 5% (two times the standard deviation). This yields uncertainties in streamwise mean and fluctuating drop velocities of 4 and 5%, as before.

A.2 Drop-Size Distribution

Various characteristic sizes can be used to represent the distribution of drop sizes. They are, essentially, different moments of the drop-size distribution. For example, for a sample of n drops, we have

$$d_k^k = \sum_{i=1}^n d_i^k / n \quad (\text{A.10})$$

where d_i is the diameter of the i'th drop. Then d_1 is the number mean drop diameter, d_2 is the area mean drop diameter, etc.

Drop size data in this report is presented as the Sauter mean diameter, which is the drop size that has the same surface area to volume ratio as the spray as a whole, at the point sampled. Thus

$$\text{SMD} = 6V/A \quad (\text{A.11})$$

where

$$V = \pi n d_3^3/6 \quad ; \quad A = n \pi n d_2^2 \quad (\text{A.12})$$

To find the uncertainty in the SMD, we first apply Eq. (A.4) to Eq. (A.11) to yield

$$\frac{\Delta \text{SMD}}{\text{SMD}} = \left[\left(\frac{\Delta V}{V} \right)^2 + \left(\frac{\Delta A}{A} \right)^2 \right]^{1/2} \quad (\text{A.13})$$

The uncertainties in V and A are primarily due to the uncertainties in the diameter of each drop in the sample and the finite sample size. To find these quantities, we first take the partial derivatives of V and A with respect to d_i , obtaining the arguments of Eq. (A.4), as follows:

$$\frac{\Delta d_i}{V} \frac{\partial V}{\partial d_i} = \frac{3 d_i^2 \Delta d_i}{n d_3^3} \quad (\text{A.14})$$

$$\frac{\Delta d_i}{A} \frac{\partial A}{\partial d_i} = \frac{2 d_i \Delta d_i}{n d_2^2} \quad (\text{A.15})$$

The total uncertainties in V and A are obtained by summing the squares of Eqs. (A.14) and (A.15) over all drops in the sample

$$\left(\frac{\Delta V}{V} \right)^2 = \sum_{i=1}^n \left(\frac{3 d_i^2 \Delta d_i}{n d_3^3} \right)^2 \quad (\text{A.16})$$

$$\left(\frac{\Delta A}{A} \right)^2 = \sum_{i=1}^n \left(\frac{2 d_i \Delta d_i}{n d_2^2} \right)^2 \quad (\text{A.17})$$

During present work, drops were grouped into size ranges having the same width, thus the uncertainty Δd_i was constant, cf. data presented in Appendix F.5. Then noting the various mean diameters defined by Eq. (A.10) we have

$$\left(\frac{\Delta V}{V} \right)^2 = \frac{9}{n} \left(\frac{d_4}{d_1} \right)^4 \left(\frac{d_1}{d_3} \right)^6 \left(\frac{\Delta d_i}{d_1} \right)^2 \quad (\text{A.18})$$

$$\left(\frac{\Delta A}{A}\right)^2 = \frac{4}{n} \left(\frac{d_1}{d_2}\right)^2 \left(\frac{\Delta d_1}{d_1}\right)^2 \quad (\text{A.19})$$

Now, the present size distributions are only roughly Gaussian, due to the propensity for smaller drops in the distribution to evaporate more rapidly than large ones. However, for present purposes, it is reasonable to assume Gaussian distributions, whereupon, it can be shown that

$$\left(\frac{d_4}{d_1}\right)^4 \left(\frac{d_1}{d_3}\right)^6 \leq 1 \quad ; \quad \left(\frac{d_1}{d_2}\right)^2 \leq 1 \quad (\text{A.20})$$

Conservatively setting these quantities equal to unity and substituting Eqs. (A.18) and (A.19) into Eq. (A.13) yields the following expression for the uncertainty in SMD

$$\frac{\Delta \text{SMD}}{\text{SMD}} = \left(\frac{13}{n}\right)^{1/2} \left(\frac{\Delta d_1}{d_1}\right) \quad (\text{A.21})$$

During current tests, $n = 200$. The factor $(\Delta d_1/d_1)$ varied from values on the order of 0.01 at the burner exit to values as high as 0.33 near the end of drop life. Taking the latter condition for specification of the maximum uncertainty we find $\Delta \text{SMD}/\text{SMD} < 10\%$ from Eq. (A.21).

A.3 Drop Number Fluxes

Uncertainties in the drop number flux are due to finite-length drop counts, the calibration of the cross-sectional area of measurement as a function of drop size and the uncertainty of the drop-size distribution when the raw data was corrected. For much of the flow, the latter correction is small (cf. Appendix F.4) and can be related to the uncertainty in mean drop diameter; therefore, this approximations will be used here.

The basic expression for drop number flux, under the present approximation, is

$$\dot{n}'' = \dot{n}/A_F (d_p \text{ avg}) \quad (\text{A.22})$$

$A_F (d_p \text{ avg})$ is the flux area at the mean drop size

$$A_F (d_p \text{ avg}) = W (d_p \text{ avg}) L (d_p \text{ avg}) \quad (\text{A.23})$$

where W and L are found from the flux area calibrations described in Appendix B.2.

Applying Eq. (A.4) to Eqs. (A.22) and (A.23) yields the following expression for the uncertainty.

$$\frac{\Delta \dot{n}''}{\dot{n}''} = \left[\left(\frac{\Delta \dot{n}}{\dot{n}} \right)^2 + \left(\frac{\Delta W}{W} \right)^2 + \left(\frac{\Delta L}{L} \right)^2 + \left(\frac{\partial \ln A_F}{\partial \ln d_p} \frac{\Delta d_{p \text{ avg}}}{d_{p \text{ avg}}} \right)^2 \right]^{1/2} \quad (\text{A.24})$$

More than 1000 drops were generally counted; therefore, the uncertainty in \dot{n} is small--less than 0.1%--and can be ignored. The uncertainty in W and L is conservatively estimated to be the region of cut-off of the count signal near the edge of the measuring region as discussed in Appendix B.2. This is roughly 10% of the mean dimension. The parameter $\partial \ln A_F / \partial \ln d_p$ is roughly unity, from the present calibration measurements. The relative uncertainty in $d_{p \text{ avg}}$ (95% confidence) is given by

$$\Delta d_{p \text{ avg}} / d_{p \text{ avg}} = 2 \sigma_{d_p} / (d_{p \text{ avg}} n^{1/2}) \quad (\text{A.25})$$

where σ_{d_p} is the standard deviation of the drop-size distribution for n drops counted. From Appendix F.5, $\sigma_{d_p} / d_{p \text{ avg}}$ is never greater than 1/2 for the data reported here, while $n = 200$. Substituting these estimates into Eq. (A.24) yields an uncertainty (95% confidence) of less than 16% in the drop number flux measurements.

A.4 Mean Gas Temperatures

The uncertainty in mean gas temperature, to the scale plotted in the present report, is greatest in the region of flame. The measurement of the mean thermocouple EMF had an uncertainty less than 1% in this region; therefore, the uncertainty in the temperature measurement is dominated by the radiation correction.

The radiation correction is described in Appendix C. For present conditions, T_∞ has little influence on the estimate of radiation error and the Reynolds number of the junction was sufficiently high so that the heat transfer coefficient is dominated by forced convection. At this limit, use of Eq. (A.4) yields the following expression for the uncertainty in the radiation error estimate.

$$\frac{\Delta(T - T_{tc})}{(T - T_{tc})} = \left[\left(\frac{\Delta \epsilon}{\epsilon} \right)^2 + \left(\frac{\Delta \lambda_f}{\lambda_f} \right)^2 + \left(0.38 \frac{\Delta d_{tc}}{d_{tc}} \right)^2 + \left(0.62 \frac{\Delta u}{u} \right)^2 + \left(0.62 \frac{\Delta v_f}{v_f} \right)^2 + \left(4 \frac{\Delta T_{tc}}{T_{tc}} \right)^2 \right]^{1/2} \quad (\text{A.26})$$

where the small uncertainty in the Stephan-Boltzman constant has been ignored.

The uncertainty in thermocouple emissivity is large, due to the practical problems of preventing accumulations of soot on the probe, and is taken to be 100%. Uncertainties in other quantities are estimated as follows: gas properties, 20%; junction diameter, 10%; gas velocity, 20%; and junction temperature reading, 1%. Substituting these estimates into Eq. (A.26) yields an uncertainty in the radiation correction of 104%.

With a maximum radiation error correction of 57 K, at a mean temperature of 1700 K, the above uncertainty becomes roughly 5% of the difference between the indicated and ambient temperatures. Estimates at other points in the flow, where temperatures are reported here, indicate comparable levels of uncertainty.

APPENDIX B

DROP NUMBER FLUX MEASUREMENTS

B.1 Pulse Counter

The pulse counting device used for the drop number flux measurements was designed and fabricated by Electronic Design Services, College of Engineering, The Pennsylvania State University. The device was designed to count electrical impulses for any desired interval from 1 to 999s. The count value is displayed on a seven digit display as a decimal integer value. The device will count pulses for any electrical signal that ranges from 0 to -12 V and has a frequency range of 0-1 MHz. A threshold adjustment allows setting of a DC level from 0 to 2 V, which determines the minimum amplitude of a signal which will be accepted as a pulse. The device was designed as a micro-processor-based system.

The amplified signal from the photodetector was fed to the pulse counter. The threshold adjustment was set to the lowest value possible where no counts were registered with the drop generator off. Drops were then produced and their counts recorded, generally setting the time of counting to record roughly 1000 drops or to count for more than 100s--whichever was the limiting factor.

Complete description of the device requires the circuit diagram and the program used to control the micro-processor. In the interest of brevity, these details are not included in the present report, but can be obtained from the senior author (GMF) upon request.

B.2 Calibration of Measuring Area

Facility limitations required that scattered light signals be observed from the same plane as the light sheet, cf. Fig. 4. This was undesirable, to some extent, since the region of observation could not be strictly controlled by the detector aperture and depended on drop size more than would be the case for off-plane observations. As a result it was necessary to calibrate the measuring area as a function of drop size. The method of calibration and some typical results will be presented in the following.

The monodisperse drop generator was used to calibrate the measuring area of the drop number flux system. The exit of the generator tube was positioned a short distance below the measuring plane (4 mm). The generator was operated with a slow flow of dispersing gas so that the drop stream was essentially colinear. The generator was mounted on two orthogonal traversing systems, each fitted with dial gauges accurate to 25 μm . Varying the generator orifice and operating conditions yielded monodisperse drop streams having diameters in the range of interest for the drop number flux measurements (36-180 μm). The pulse-counter threshold and detector gain were set as described in Section B.1 and kept at this condition during calibration, since the calibration was influenced by these parameters. The calibration tests consisted of traversing the generator across the

measuring volume in the two directions and recording the drop pulse rate as a function of position.

Some typical results of the calibration are illustrated in Fig. B.1. Results for two different drop sizes and for traverses along and normal to the optical axis (both centered on the measuring volume) are shown. The observed counts drop off reasonably fast at the edge of the measuring volume, but the stronger scattering signal from the larger drops causes the threshold on the detector to be crossed at a larger distance from the center of the measuring volume. The region of decreasing signal represents the uncertainty in the cross-sectional area; this was generally less than $\pm 10\%$ of the mean dimension of observation. Off-axis traverses indicated that the measuring region was roughly rectangular and this was assumed for both the flux area calibration and the analysis of uncertainty of the flux measurements. The calibrations are not given here, since they are specific for the present gain and threshold settings and would be of little general value.

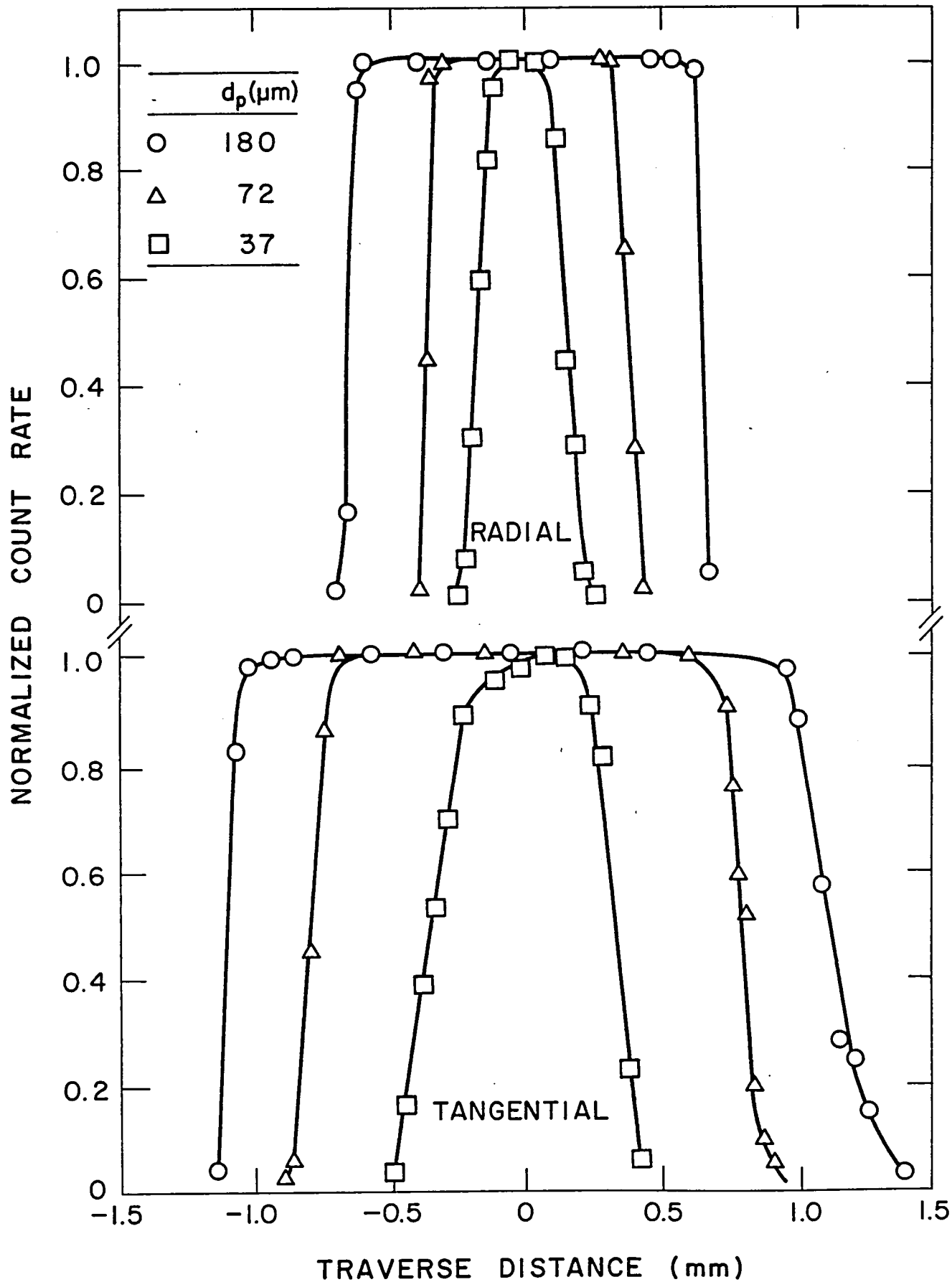


Fig. B.1. Drop number flux calibration.

APPENDIX C

CORRECTION OF TEMPERATURE MEASUREMENTS FOR RADIATION

Radiation errors for the thermocouple were estimated considering heat gain by convection from the local gas flow and heat loss by radiation to the room, through a transparent flame. This ignores radiation from the flame to the thermocouple, which tends to increase its indicated temperature from the estimates made here. We also neglect heat transfer to the thermocouple leads, since the present configuration had fine-wire leads, with relatively large length-to-diameter ratios, cf. Fig. 5.

Conservation of energy for the thermocouple lead yields

$$T = T_{tc} + (\epsilon\sigma/h)(T_{tc}^4 - T_{\infty}^4) \quad (C.1)$$

where ϵ is the thermocouple emissivity, σ is the Stefan-Boltzmann constant and h is the convection heat transfer coefficient to the bead of the junction.

The thermocouple junction was formed by butt-welding two 76 μm , Pt/Pt-10% Rh wires together. The junction was then coated with silica to minimize catalytic effects. The final diameter of the bead was measured with a microscope to be 225 μm .

The emissivity of the thermocouple bead was taken to be equal to the emissivity of platinum, given by Caldwell [51], as follows

$$\epsilon = 9.6 \times 10^{-5} T_{tc} + 0.056 \quad (C.2)$$

where T_{tc} is in K. The coating is essentially transparent to radiation.

The flame gases have a Prandtl number of nearly 0.7, since the mixture is dominated by nitrogen. In this case, the Nusselt number for a thermocouple bead can be obtained from the following formula from Becker and Yamazaki [52].

$$hd_{tc}/\lambda = 2 + 0.31 (ud_{tc}/\nu)^{0.62} \quad (C.3)$$

where d_{tc} is the bead diameter, u is the relative gas velocity, λ is the thermal conductivity and ν is the kinematic viscosity. Properties are evaluated at the average temperature of the thermal boundary layer, T_f .

Properties of the gas mixture were approximated as pure air, with density obtained under the assumption of an ideal gas. The gas viscosity was computed from [53]

$$\begin{aligned} \mu_f(\text{Ns/m}^2) = & 0.40201 + 0.74582 T_f - 0.57171 T_f^2 \\ & + 0.29928 T_f^3 - 0.62524 T_f^4 \end{aligned} \quad (\text{C.4})$$

where T_f is in K. The thermal conductivity was obtained from [52]

$$\lambda_f(\text{W/mK}) = 264.6 \times 10^{-5} T_f^{3/2} / (T_f + 245 \times 10^{-12}/T_f) \quad (\text{C.5})$$

where T_f is also in K.

Thermocouple errors were calculated using the measured mean velocities and temperatures at each location. The maximum magnitude of the correction was 57 K, at the maximum flame temperature location.

APPENDIX D

DROP TRANSPORT PROPERTIES

D.1 Mixture Thermal Conductivity

The thermal conductivity of the gaseous mixture was calculated with the Mason and Saxena formulation of the Wassiljewa equation, cited in Reid et al. [54]. For a mixture of N components:

$$\lambda_m = \sum_{i=1}^N \frac{X_i \lambda_i}{\sum_{j=1}^N X_j \phi_{ij}} \quad (D.1)$$

where

$$\phi_{ij} = \frac{1}{8^{1/2}} \left(1 + \frac{M_i}{M_j}\right)^{-1/2} \left[1 + \left(\frac{\mu_i}{\mu_j}\right)^{1/2} \left(\frac{M_j}{M_i}\right)^{1/4}\right]^2 \quad (D.2)$$

The thermal conductivity and viscosity for gases were obtained from Svehla [55]. Equations (D.1) and (D.2) were evaluated at the reference state defined by Eq. (3.28).

D.2 Mixture Viscosity

The viscosity calculations of the mixture employed the method of Wilke, cited by Reid et al. [54]. For a mixture of N components:

$$\mu_m = \sum_{i=1}^N \left[\frac{X_i \mu_i}{\sum_{j=1}^N X_j \phi_{ij}} \right] \quad (D.3)$$

where ϕ_{ij} is given by Eq. (D.2). The viscosity data used in the calculations was obtained in the same manner as described in Section D.1.

D.3 Mixture Mass Diffusivity

Since only fuel vapor diffuses through the stagnant mixture, the diffusion coefficient is given as [54]

$$D_{1m} = \left[\sum_{j=2}^N \frac{X_j}{D_{1j}} \right]^{-1} = D \quad (D.4)$$

Subscript 1 represents fuel vapor, and j indicates all other gases. Binary diffusivity calculations employed Chapman-Enskog theory along

with Lennard-Jones characteristic energy and length concept cited by Reid et al. [54]. Values of the characteristic energies and lengths were drawn from the same source and are summarized in Table D.1.

D.4 Mixture Specific Heat

The mixture specific heat was calculated as a mole fraction weighted average of the specific heats of each contributing species

$$C_p = \frac{\sum_{i=1}^N X_i \bar{C}_{p_i}}{M} \quad (D.5)$$

D.5 Properties of Methanol

The fundamental thermochemical properties of methanol are summarized in Table D.2. Values are drawn from the sources indicated in the table.

The vapor pressure relationship used for methanol was [54]:

$$\begin{aligned} \log_{10} p_v \text{ (mm Hg)} = & - 42.629 - 1186.2/T + 23.279 \log_{10} T \\ & - 35.082 (T/1000) + 17.578 (T/1000)^2 \end{aligned} \quad (D.6)$$

where T(K).

The heat of vaporization correlation used for methanol was [55]:

$$h_{fg} \text{ (kJ/kg)} = 1088 \left((T_{cr} - T)/(T_{cr} - T_r) \right)^{0.4} \quad (D.7)$$

where T(K) and $T_r = 337.9$ K.

The specific heat of liquid methanol was [55]

$$\begin{aligned} C_p \text{ (kJ/kgK)} = & 3.506 - 13.51 (T/1000) + 34.71 (T/1000)^2 \\ & + 0.7067 (T/1000)^3 \end{aligned} \quad (D.8)$$

where T(K).

Table D.1

Properties Used for Binary Diffusivity Calculations^a

Substance	σ' (Å ⁰)	ϵ'/k' (K)
H ₂ O	2.641	809.1
CO	3.690	91.7
CO ₂	3.941	195.2
N ₂	3.798	71.4
H ₂	2.827	59.7
O ₂	3.467	106.7
CH ₄	3.758	148.6
CH ₃ OH	3.626	481.8

^aTaken from Reid et al. [54].

Table D.2 Thermochemical Properties of Methanol

Property	Value	Source
Formula	CH ₃ OH	[54]
Molecular Weight	32.04	[54]
Normal Boiling Temperature (K)	337.8	[54]
Critical Temperature (K)	513.2	[54]
Critical Pressure (bar)	79.5	[54]
Critical Volume (m ³ /kg mole)	0.118	[54]
Liquid Specific Heat (kJ/kgK) ^a	2.54	[55]
Liquid Density (kg/m ³) ^a	790	[55]
Heat of Vaporization (kJ/kg) ^a	1088	[55]
Heat of Combustion (kJ/kg)	14094	[56]

^aAt 25°C.

APPENDIX E

DROP TRANSPORT CALIBRATION

E.1 Experimental Method

Drop transport calibration tests were conducted using the supported drop technique. The drop environment was created by a laminar flat-flame burner, using methane and air as reactants in order to simulate the turbulent flame environment. The drops were rapidly submerged in the post-flame region of the flat-flame burner and photographed as they evaporated. The films were then measured to yield drop size as a function of time.

A sketch of the flat-flame burner apparatus appears in Fig. E.1. The burner construction is described completely by Szekely [57]. Fuel gas and air flow rates were measured with rotameters which were calibrated by wet-test meters for each gas used. Fuel gases were mixed in a 1500 mm long, 10 mm inside diameter tube before entering the burner assembly. The burner was constructed of 51 mm nominal diameter, schedule 40, stainless steel welded pipe having a total length of 300 mm. After entering the base of the burner, the gases flowed up the length of the housing through two 50 mm thick layers of 3 mm diameter glass beads and one 50 mm thick layer of 2 mm diameter stainless steel beads. The bead layers were separated by 50 mm long void spaces, and were supported by 20 mesh stainless steel screens spot-welded to the sides of the burner housing. Stainless steel screens (100 mesh) were placed on top of each 20 mesh screen to ensure that no beads would fall through to the next layer. This burner design provided complete premixing of the burner gases, and supported a flat flame, roughly 2-3 mm thick, on the top layer of stainless steel beads. A quartz shroud on top of the burner prevented the burner gases from mixing with the ambient atmosphere.

Drops were mounted on quartz probes and then centered on the burner exit with the pneumatically-driven shield, illustrated in Fig. E.1, in place. Actuating the pneumatic cylinder withdrew the shield and started the evaporation process.

All flame conditions were characterized by determining the gas temperature, species concentrations and gas velocity at the drop position.

Gas temperatures were measured using Pt/Pt-10% Rh thermocouples with bead diameters of approximately 50 μm . The signal from these thermocouples was observed with an integrating digital voltmeter. The reading was then corrected for radiation losses as described in Appendix C.

Species concentrations were measured at the particle test location using a stainless steel water-cooled sampling probe having a 0.7 mm diameter sampling port. Water flow rate through the sampling probe was adjusted to maintain a probe temperature of about 340 K in order to

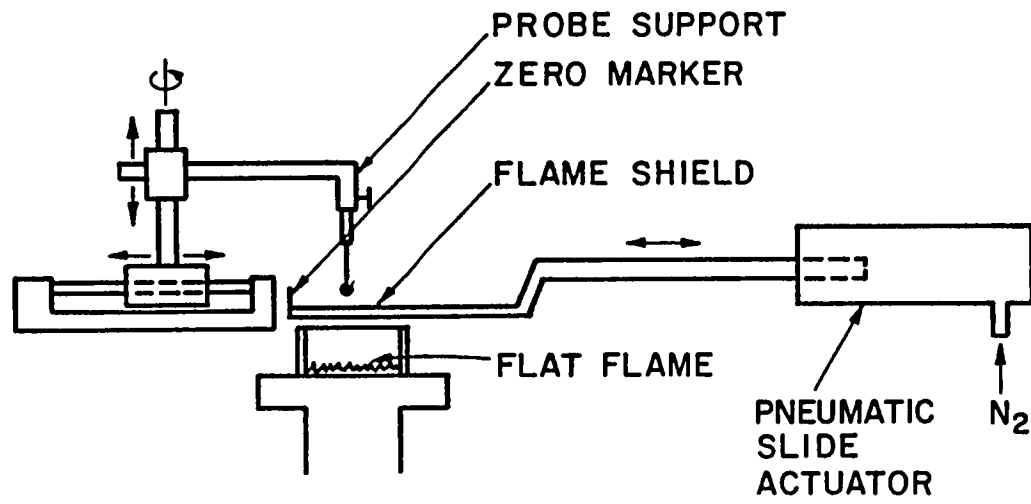


Fig. E.1. Flat-flame burner apparatus.

avoid condensation of water vapor inside the probe. Water vapor in the sample was removed farther downstream by an ice-bath condenser. The dry sample was collected in a 125 ml sampling bulb (Supelco, model 2-2161), which was connected to a Welch Scientific duo-seal vacuum pump, model 1450. Sample flow rates were controlled with a Whitey regulating valve and metered with a bubble meter to ensure nearly isokinetic sampling at the probe inlet. The sample was drawn through the septum of the sampling bulb into a 1.0 ml series C Pressure-Lock gas syringe, and was analyzed using a Varian model 3720 gas chromatograph. The gas chromatograph was fitted with a Supelco carbosieve S, 100/120 mesh, 2.1 m x 3.2 mm stainless steel column, and was temperature programmed to separate the product gases. An initial column temperature of 35°C was maintained for 4 minutes, and then increased to 175°C at a rate of 25°C/minute. The GC was calibrated with Scott gas mixtures of known concentrations ($\pm 2\%$) of nitrogen, oxygen, carbon monoxide and carbon dioxide. Helium was used as the carrier gas, having a flow rate of 0.4 ml/second. Product mole fractions were determined experimentally on a dry basis, and converted to a wet basis by conservation of element analysis. Species concentration measurements for all flame conditions used in this study were verified with the chemical equilibrium calculation code CEC76 [36].

Gas velocities at the test section were calculated assuming one-dimensional flow of an ideal gas at the measured gas temperature and composition. A summary of all flame conditions used in this study is provided in Table 6. The temperatures listed refer to the maximum temperatures measured for each flame condition. Average gas temperatures during testing were 1-2% lower than the values tabulated.

Drop diameters were measured as a function of residence time in the burner gases by means of a 16 mm motion picture camera (Redlake Locam, model 51), capable of resolution up to 2 milliseconds, but run at a film speed of roughly 200 pictures per second for present work. The camera was equipped with an LED timing marker (powered by an external timing pulse generator). Kodak plus-X reversal film was used for the tests. Drops were backlit with a 60 watt light bulb operated at input voltages which varied between 60-120 V. Photographs of an Edmund Scientific graticule provided the size calibrations for the particle diameter measurements. Particle sizes were obtained from the film records using a Vanguard/Bendix computer digitizing motion analyzer. Effective particle diameters were calculated as in past work by approximating the particles as ellipsoids [1]. This approximation was found to be quite reasonable for the present drops, with typical particle eccentricities ranging from 1.1-1.4.

E.2 Drop-Life-History Data

Table E.1 Drop Diameter Squared vs. Time:
 $d_{p0} = 2293 \mu\text{m}$, $\phi = 0.65$

Time(s)	$(d_p/d_{p0})^2$	Time(s)	$(d_p/d_{p0})^2$
0.00	1.00	1.40	0.62
0.10	0.98	1.60	0.54
0.20	0.94	1.80	0.50
0.40	0.90	2.00	0.46
0.60	0.84	2.20	0.39
0.80	0.78	2.40	0.35
1.00	0.71	2.60	0.28
1.20	0.67	2.80	0.24

Table E.2 Drop Diameter Squared vs. Time:
 $d_{p0} = 2786 \mu\text{m}$, $\phi = 0.82$

Time(s)	$(d_p/d_{p0})^2$	Time(s)	$(d_p/d_{p0})^2$
0.00	1.00	1.75	0.65
0.25	0.97	2.00	0.59
0.50	0.92	2.25	0.51
0.75	0.88	2.50	0.47
1.00	0.82	2.75	0.45
1.25	0.75	3.00	0.42
1.50	0.71		

Table E.3 Drop Diameter Squared vs. Time:
 $d_{p0} = 2953 \mu\text{m}$, $\phi = 0.97$

Time(s)	$(d_p/d_{p0})^2$	Time(s)	$(d_p/d_{p0})^2$
0.00	1.00	2.25	0.68
0.25	0.97	2.50	0.63
0.50	0.94	2.75	0.60
0.75	0.90	3.00	0.56
1.00	0.87	3.25	0.52
1.25	0.84	3.50	0.48
1.50	0.79	3.75	0.45
1.75	0.76	4.00	0.43
2.00	0.72	4.25	0.38

APPENDIX F

FLAME STRUCTURE DATA

F.1 Mean Gas Temperatures*

Table F.1.1 Mean Temperatures Along the Axis

x/d	\bar{T} (K)	x/d	\bar{T} (K)
20	782	90	1677
23	858	100	1719
26	935	110	1747
30	1016	120	1730
40	1188	135	1610
50	1325	150	1437
60	1444	170	1153
70	1534	190	939
80	1621	--	--

*All mean temperatures are corrected for radiation heat loss as described in Appendix C.

Table F.1.2 Mean Temperatures at $x/d = 20$

r/x	$\bar{T}(K)$	r/x	$\bar{T}(K)$
0.00	805	0.11	1342
0.01	809	0.12	1457
0.02	822	0.13	1552
0.03	840	0.14	1603
0.04	876	0.15	1619
0.05	905	0.16	1591
0.06	959	0.17	1525
0.07	1020	0.18	1364
0.08	1091	0.19	1248
0.09	1153	0.20	1062
0.10	1265	0.21	877

Table F.1.3 Mean Temperatures at $x/d = 50$

r/x	$\bar{T}(K)$	r/x	$\bar{T}(K)$
0.000	1324	0.108	1642
0.012	1333	0.120	1568
0.024	1360	0.132	1413
0.036	1403	0.144	1232
0.048	1461	0.156	1074
0.060	1537	0.168	932
0.072	1603	0.180	755
0.084	1652	0.192	628
0.096	1678	0.204	518

Table F.1.4 Mean Temperatures at $x/d = 100$

r/x	$\bar{T}(K)$	r/x	$\bar{T}(K)$
0.000	1729	0.112	915
0.016	1727	0.128	783
0.032	1702	0.144	625
0.048	1621	0.160	516
0.064	1475	0.176	462
0.080	1297	0.192	378
0.096	1115	0.208	300

F.2 Gas Velocities

Table F.2.1 Gas Velocities (m/s) Along the Axis

x/d	\bar{u}_c	\bar{u}'_c	\bar{v}'_c	x/d	\bar{u}_c	\bar{u}'_c	\bar{v}'_c
1	52.80	2.43	2.53	26	18.82	4.08	3.16
2	53.30	2.77	2.61	30	17.59	3.74	3.04
3	53.30	2.98	2.77	40	15.07	3.10	2.56
4	51.80	4.77	3.52	50	13.19	2.57	2.09
5	51.20	6.66	4.15	60	11.63	2.15	1.81
6	48.90	7.34	4.35	70	10.20	2.04	1.59
7	46.60	8.76	4.75	80	9.23	2.00	1.50
8	43.80	9.02	5.08	90	8.55	1.88	1.42
9	40.20	8.80	5.31	100	7.76	1.81	1.36
10	38.20	8.52	5.39	120	7.00	1.73	1.30
12	32.80	7.45	5.18	135	6.23	1.67	1.28
14	29.00	6.35	4.61	150	5.70	1.62	1.26
16	25.20	5.49	4.21	170	5.08	1.45	1.21
20	22.90	4.99	3.76	190	4.64	1.33	1.18
23	20.79	4.41	3.44	--	--	--	--

Table F.2.2 Gas Velocities, $x/d = 1$

r/x	\bar{u}/\bar{u}_c	$\overline{u'v'}/\bar{u}_c^2$	\bar{u}'/\bar{u}_c	\bar{v}'/\bar{u}_c	\bar{w}'/\bar{u}_c	k/\bar{u}_c^2
0.00	1.000	--	0.040	0.051	0.053	0.0035
0.10	1.001	--	0.044	0.049	0.054	0.0036
0.20	1.004	--	0.047	0.055	0.054	0.0041
0.30	0.998	--	0.051	0.055	0.056	0.0044
0.40	0.960	--	0.089	0.062	0.057	0.0075
0.50	0.743	--	0.184	0.090	0.064	0.0230
0.60	0.552	--	0.162	0.070	0.044	0.0165

Table F.2.3 Gas Velocities, $x/d = 20$

r/x	\bar{u}/\bar{u}_c	$\overline{u'v'}/\bar{u}_c^2$	\bar{u}'/\bar{u}_c	\bar{v}'/\bar{u}_c	\bar{w}'/\bar{u}_c	k/\bar{u}_c^2
0.00	1.000	0.0000	0.209	0.161	0.158	0.0473
0.01	0.999	0.0024	0.206	0.163	0.160	0.0473
0.02	0.992	0.0029	0.199	0.157	0.165	0.0457
0.03	0.960	0.0045	0.210	0.161	0.171	0.0496
0.04	0.931	0.0063	0.202	0.162	0.173	0.0485
0.05	0.889	0.0083	0.205	0.163	0.165	0.0479
0.06	0.839	0.0095	0.209	0.160	0.164	0.0481
0.07	0.780	0.0101	0.209	0.163	0.165	0.0487
0.08	0.721	0.0080	0.208	0.162	0.145	0.0453
0.09	0.675	0.0070	0.194	0.147	0.135	0.0387
0.10	0.597	0.0060	0.160	0.131	0.126	0.0293
0.11	0.530	0.0043	0.144	0.108	0.177	0.0230

Table F.2.4 Gas Velocities, $x/d = 50$

r/x	\bar{u}/\bar{u}_c	$\overline{u'v'}/\bar{u}_c^2$	\bar{u}'/\bar{u}_c	\bar{v}'/\bar{u}_c	\bar{w}'/\bar{u}_c	k/\bar{u}_c^2
0.000	1.000	0.0000	0.187	0.148	0.150	0.0397
0.012	0.994	0.0033	0.185	0.147	0.152	0.0395
0.024	0.949	0.0061	0.193	0.150	0.158	0.0424
0.036	0.877	0.0095	0.207	0.154	0.163	0.0466
0.048	0.804	0.0109	0.215	0.156	0.165	0.0489
0.060	0.724	0.0112	0.219	0.154	0.167	0.0498
0.072	0.641	0.0106	0.219	0.151	0.169	0.0497
0.084	0.551	0.0084	0.214	0.147	0.160	0.0465
0.096	0.406	0.0076	0.203	0.133	0.151	0.0408
0.108	0.340	0.0060	0.187	0.113	0.131	0.0324
0.120	0.271	0.0047	0.165	0.102	0.112	0.0251
0.132	0.201	0.0046	0.139	0.070	0.099	0.0176
0.144	0.160	0.0028	0.119	0.062	0.086	0.0127
0.156	0.123	0.0020	0.088	0.044	0.066	0.0070
0.168	0.091	0.0015	0.070	0.032	0.050	0.0042

Table F.2.5 Gas Velocities, $x/d = 100$

r/x	\bar{u}/\bar{u}_c	$\overline{u'v'}/\bar{u}_c^2$	\bar{u}'/\bar{u}_c	\bar{v}'/\bar{u}_c	\bar{w}'/\bar{u}_c	k/\bar{u}_c^2
0.000	1.000	0.0000	0.238	0.174	0.173	0.0584
0.016	0.958	0.0066	0.234	0.169	0.174	0.0568
0.032	0.841	0.0110	0.251	0.166	0.175	0.0606
0.048	0.715	0.0139	0.248	0.164	0.174	0.0590
0.064	0.575	0.0143	0.239	0.156	0.164	0.0540
0.080	0.471	0.0120	0.209	0.149	0.150	0.0442
0.096	0.372	0.0105	0.173	0.140	0.138	0.0343
0.112	0.295	0.0084	0.146	0.126	0.119	0.0257
0.128	0.213	0.0059	0.129	0.111	0.100	0.0195
0.144	0.161	0.0042	0.103	0.091	0.076	0.0123
0.160	0.125	0.0016	0.080	0.074	0.065	0.0081
0.176	0.092	0.0007	0.059	0.064	0.050	0.0050

F.3 Drop Velocities

Table F.3.1 Drop Velocities (m/s) Along the Axis, $d_{p0} = 105 \mu\text{m}$

x/d	\bar{u}'_p	\bar{u}'_p	\bar{v}'_p	x/d	\bar{u}'_p	\bar{u}'_p	\bar{v}'_p
1	15.62	0.309	0.273	30	21.26	1.585	0.262
2	16.92	0.347	0.283	35	20.45	1.625	0.237
3	18.21	0.397	0.305	40	19.54	1.493	0.239
4	19.40	0.440	0.329	45	19.25	1.414	0.261
5	20.27	0.532	0.324	50	18.71	1.518	0.275
6	20.97	0.616	0.329	55	16.89	1.616	0.302
7	21.65	0.783	0.329	60	15.70	1.603	0.336
8	22.13	0.879	0.322	65	14.53	2.009	0.361
9	22.34	0.990	0.338	70	13.17	2.013	0.458
10	22.57	1.134	0.339	80	11.16	2.187	0.602
11	22.94	1.141	0.332	90	10.52	2.367	0.621
12	23.24	1.202	0.347	100	9.99	2.357	0.693
15	23.52	1.259	0.345	110	9.34	2.360	0.621
18	23.37	1.350	0.351	120	8.26	2.255	0.586
20	23.26	1.476	0.340	130	7.76	2.020	0.755
23	22.67	1.537	0.311	140	6.56	2.010	0.725
26	22.06	1.548	0.278	--	--	--	--

Table F.3.2 Drop Velocities (m/s) Along the Axis, $d_{p0} = 180 \mu\text{m}$

x/d	\bar{u}_p	\bar{u}'_p	\bar{v}'_p	x/d	\bar{u}_p	\bar{u}'_p	\bar{v}'_p
1	11.96	0.477	0.440	30	17.82	1.110	0.196
2	13.17	0.541	0.501	35	17.79	1.140	0.186
3	14.30	0.623	0.488	40	17.72	1.090	0.143
4	15.50	0.906	0.497	44	17.62	1.030	0.139
5	16.05	0.952	0.420	50	17.52	1.055	0.117
6	16.54	1.140	0.417	54	17.37	0.990	0.104
7	16.83	1.240	0.441	60	17.07	1.055	0.112
8	17.05	1.273	0.434	70	16.46	1.105	0.116
9	17.24	1.440	0.411	80	15.78	1.145	0.153
10	17.36	1.300	0.336	90	14.39	1.150	0.168
11	17.62	1.410	0.402	100	13.62	1.260	0.202
12	17.48	1.440	0.328	110	12.60	1.390	0.226
15	17.64	1.390	0.281	120	11.32	1.617	0.290
18	17.74	1.350	0.271	135	9.19	1.930	0.440
20	17.77	1.340	0.240	150	7.18	2.090	0.636
23	17.79	1.280	0.191	170	5.98	1.960	0.715
26	17.78	1.210	0.219	190	4.93	1.470	0.527

Table F.3.3 Drop Velocities: $d_{p0} = 105 \mu\text{m}$, $x/d = 1$

r/x	\bar{u}_p/\bar{u}_{pc}	\bar{u}'_p/\bar{u}_{pc}	\bar{v}'_p/\bar{u}_{pc}	\bar{w}'_p/\bar{u}_{pc}
0.0	1.000	0.0198	0.0175	0.0172
0.1	1.001	0.0192	0.0177	0.0172
0.2	1.004	0.0189	0.0177	0.0174
0.3	1.008	0.0186	0.0184	0.0175
0.4	0.996	0.0252	0.0195	0.0177
-0.1	1.012	0.0186	0.0172	0.0169
-0.2	1.014	0.0175	0.0169	0.0163
-0.3	1.015	0.0176	0.0175	0.0171
-0.4	1.007	0.0235	0.0190	0.0181

Table F.3.4 Drop Velocities: $d_{p0} = 105 \mu\text{m}$, $x/d = 20$

r/x	\bar{u}_p/\bar{u}_{pc}	\bar{u}'_p/\bar{u}_{pc}	\bar{v}'_p/\bar{u}_{pc}	\bar{w}'_p/\bar{u}_{pc}
0.00	1.000	0.0597	0.0151	0.0151
0.01	0.993	0.0643	0.0145	0.0141
0.02	0.981	0.0656	0.0148	0.0138
0.03	0.963	0.0682	0.0148	0.0139
0.04	0.943	0.0730	0.0152	0.0139
0.05	0.921	0.0718	0.0155	0.0135
0.06	0.896	0.0715	0.0155	0.0136
0.07	0.876	0.0738	0.0157	0.0137
0.08	0.849	0.0749	0.0162	0.0133
0.09	0.815	0.0806	0.0152	0.0133
0.10	0.782	0.0837	0.0172	0.0131
0.11	0.770	0.1030	0.0188	0.0136

Table F.3.5 Drop Velocities: $d_{p0} = 105 \mu\text{m}$, $x/d = 50$

r/x	\bar{u}_p/\bar{u}_{pc}	\bar{u}'_p/\bar{u}_{pc}	\bar{v}'_p/\bar{u}_{pc}	\bar{w}'_p/\bar{u}_{pc}
0.000	1.000	0.0775	0.0117	0.0116
0.008	0.995	0.0771	0.0113	0.0114
0.016	0.995	0.0766	0.0117	0.0119
0.024	0.991	0.0738	0.0124	0.0130
0.032	0.973	0.0770	0.0129	0.0139
0.040	0.953	0.0794	0.0147	0.0159
0.048	0.901	0.0936	0.0146	0.0168
0.056	0.851	0.1014	0.0171	0.0178
0.064	0.808	0.1092	0.0188	0.0207
0.072	0.764	0.1199	0.0186	0.0201
0.080	0.720	0.1193	0.0228	0.0229
0.088	0.619	0.1520	0.0289	0.0309

Table F.3.6 Drop Velocities: $d_{p0} = 105 \mu\text{m}$, $x/d = 100$

r/x	\bar{u}_p/\bar{u}_{pc}	\bar{u}'_p/\bar{u}_{pc}	\bar{v}'_p/\bar{u}_{pc}	\bar{w}'_p/\bar{u}_{pc}
0.000	1.000	0.236	0.0716	0.0694
0.012	0.980	0.256	0.0714	0.0714
0.024	0.871	0.353	0.0756	0.0736
0.036	0.839	0.319	0.0698	0.0705
0.048	0.785	0.313	0.0788	0.0757
0.060	0.656	0.302	0.0684	0.0785

Table F.3.7 Drop Velocities: $d_{p0} = 180 \mu\text{m}$, $x/d = 1$

r/x	\bar{u}_p/\bar{u}_{pc}	\bar{u}'_p/\bar{u}_{pc}	\bar{v}'_p/\bar{u}_{pc}	\bar{w}'_p/\bar{u}_{pc}
0.0	1.000	0.040	0.037	0.037
0.1	1.001	0.039	0.037	0.036
0.2	1.001	0.038	0.037	0.035
0.3	1.003	0.038	0.037	0.037
0.4	1.005	0.041	0.037	0.038

Table F.3.8 Drop Velocities: $d_{p0} = 180 \mu\text{m}$, $x/d = 20$

r/x	\bar{u}_p / \bar{u}_{pc}	$\bar{u}'_p / \bar{u}_{pc}$	$\bar{v}'_p / \bar{u}_{pc}$	$\bar{w}'_p / \bar{u}_{pc}$
0.00	1.000	0.074	0.012	0.012
0.01	0.999	0.074	0.012	0.012
0.02	0.987	0.073	0.011	0.011
0.03	0.973	0.078	0.012	0.011
0.04	0.949	0.084	0.012	0.011
0.05	0.909	0.087	0.012	0.011
0.06	0.885	0.101	0.012	0.012
0.07	0.858	0.130	0.013	0.012
0.08	0.822	0.127	0.013	0.011
0.09	0.788	0.130	0.014	0.011
0.10	0.756	0.149	0.019	0.012
0.11	0.706	0.177	0.024	0.012

Table F.3.9 Drop Velocities: $d_{p0} = 180 \mu\text{m}$, $x/d = 50$

r/x	\bar{u}_p / \bar{u}_{pc}	$\bar{u}'_p / \bar{u}_{pc}$	$\bar{v}'_p / \bar{u}_{pc}$	$\bar{w}'_p / \bar{u}_{pc}$
0.000	1.000	0.071	0.009	0.010
0.012	0.996	0.069	0.009	0.0097
0.024	0.981	0.075	0.009	0.0096
0.036	0.959	0.075	0.010	0.010
0.048	0.927	0.092	0.010	0.0097
0.060	0.870	0.102	0.012	0.010
0.072	0.819	0.103	0.015	0.011
0.084	0.761	0.097	0.015	0.012
0.096	0.715	0.100	--	--

Table F.3.10 Drop Velocities: $d_{p0} = 180 \mu\text{m}$, $x/d = 100$

r/x	\bar{u}_p/\bar{u}_{pc}	\bar{u}'_p/\bar{u}_{pc}	\bar{v}'_p/\bar{u}_{pc}	\bar{w}'_p/\bar{u}_{pc}
0.000	1.000	0.089	0.016	0.015
0.012	0.983	0.091	0.015	0.016
0.024	0.966	0.095	0.015	0.015
0.036	0.919	0.107	0.016	0.016
0.048	0.870	0.116	0.017	0.018
0.060	0.778	0.120	0.018	0.019
0.072	0.694	0.128	0.022	0.021
0.084	0.585	0.144	0.027	0.023
0.096	0.470	0.167	0.030	0.025

F.4 Drop Number Fluxes

Table F.4.1 Drop Number Fluxes (\dot{n}_C/\dot{n}_{CO}^*)
 Along Axis, $d_{p0} = 105 \mu\text{m}^*$

x/d	Uncorrected	Corrected	x/d	Uncorrected	Corrected
1.0	1.000	1.000	20	0.177	0.190
1.5	0.943	0.945	22	0.156	0.169
2	0.929	0.932	25	0.126	0.138
3	0.853	0.859	30	0.0882	0.0987
4	0.756	0.764	35	0.0645	0.0737
5	0.683	0.693	40	0.0489	0.0570
6	0.608	0.619	45	0.0377	0.0449
7	0.541	0.553	50	0.0305	0.0372
8	0.471	0.483	60	0.0224	0.0356
9	0.442	0.455	70	0.0139	0.0300
10	0.409	0.423	80	0.00636	0.0164
12	0.351	0.365	90	0.00206	0.00656
15	0.258	0.272	100	0.000963	0.00401
17	0.223	0.237	--	--	--

* $\dot{n}_{CO}^* = 3769 \times 10^6$ counts/m²s. Uncorrected values are raw data while corrected values allow for area bias.

Table F.4.2 Drop Number Fluxes ($\dot{n}_C^*/\dot{n}_{CO}^*$)
 Along Axis, $d_{p0} = 180 \mu\text{m}^*$

x/d	Uncorrected	Corrected	x/d	Uncorrected	Corrected
1.0	1.000	1.000	35	0.042	0.043
1.5	0.949	0.949	40	0.033	0.034
2	0.902	0.903	45	0.025	0.026
3	0.812	0.813	50	0.0224	0.0233
4	0.749	0.751	60	0.0159	0.0170
5	0.648	0.650	70	0.0121	0.0133
6	0.584	0.586	80	0.0097	0.0108
7	0.509	0.511	90	0.0079	0.0090
8	0.459	0.461	100	0.0053	0.0061
9	0.432	0.435	110	0.0042	0.0062
10	0.327	0.329	120	0.0033	0.0069
12	0.266	0.268	130	0.0024	0.0075
15	0.195	0.197	140	0.0017	0.0056
17	0.134	0.136	150	0.0012	0.0043
20	0.113	0.115	160	0.00095	0.0037
22	0.097	0.099	170	0.00084	0.0036
25	0.076	0.077	180	0.00072	0.0033
30	0.055	0.056	190	0.00055	0.0029

* $\dot{n}_{CO}^* = 1826 \times 10^6$ counts/m²s. Uncorrected values are raw data while corrected values allow for area bias.

Table F.4.3 Drop Number Fluxes (\dot{n}''/\dot{n}''_0), $d_{p0} = 105 \mu\text{m}^*$

x/d	Uncorrected	Corrected	r/x	Uncorrected	Corrected
<u>x/d = 1</u>					
0.0	1.000	--	0.3	0.223	--
0.1	0.871	--	0.4	0.055	--
0.2	0.567	--	--	--	--
<u>x/d = 20</u>					
0.00	1.000	--	0.05	0.131	--
0.01	0.839	--	0.06	0.059	--
0.02	0.614	--	0.07	0.027	--
0.03	0.400	--	0.08	0.011	--
0.04	0.236	--	0.09	0.0034	--
<u>x/d = 50</u>					
0.000	1.000	1.000	0.048	0.0848	0.115
0.008	0.884	0.934	0.056	0.0449	0.0658
0.016	0.687	0.770	0.064	0.0216	0.0344
0.024	0.470	0.560	0.072	0.0106	0.0181
0.032	0.287	0.357	0.080	0.0056	0.0101
0.040	0.164	0.213	--	--	--
<u>x/d = 100</u>					
0.000	1.000	1.000	0.040	0.107	0.265
0.016	0.620	0.793	0.048	0.044	0.156
0.024	0.432	0.652	0.056	0.0122	0.0766
0.032	0.220	0.413	--	--	--

*Uncorrected values are raw data while corrected values allow for area bias.

Table F.4.4 Drop Number Fluxes (\dot{n}''/\dot{n}''_0), $d_{p0} = 180 \mu\text{m}^*$

x/d	Uncorrected	Corrected	r/x	Uncorrected	Corrected
<u>$x/d = 1$</u>					
0.0	1.000	--	0.3	0.179	--
0.1	0.790	--	0.4	0.039	--
0.2	0.441	--	--	--	--
<u>$x/d = 20$</u>					
0.00	1.000	--	0.05	0.136	--
0.01	0.913	--	0.06	0.069	--
0.02	0.685	--	0.07	0.036	--
0.03	0.460	--	0.08	0.017	--
0.04	0.263	--	0.09	0.0078	--
<u>$x/d = 50$</u>					
0.000	1.000	1.000	0.048	0.148	0.150
0.008	0.911	0.914	0.056	0.085	0.086
0.016	0.796	0.801	0.064	0.043	0.043
0.024	0.611	0.617	0.072	0.021	0.021
0.032	0.414	0.418	0.080	0.0099	0.010
0.040	0.252	0.254	--	--	--
<u>$x/d = 100$</u>					
0.000	1.000	1.000	0.040	0.180	0.337
0.008	0.879	0.912	0.048	0.088	0.200
0.016	0.683	0.776	0.056	0.049	0.120
0.024	0.484	0.607	0.064	0.018	0.048
0.032	0.304	0.457	0.072	0.008	0.023

*Uncorrected values are raw data while corrected values allow for area bias.

F.5 Drop Size Distributions

Table F.5.1 Axial Variation of SMD (μm)

x/d	SMD	x/d	SMD
<u>$d_{p0} = 105 \mu\text{m}$</u>			
1	105.0	100	53.4
50	95.6	130	39.8
70	75.0	--	--
<u>$d_{p0} = 180 \mu\text{m}$</u>			
1	180.0	100	113.5
50	161.9	130	70.1
70	138.0	--	--

Table F.5.2 Radial Variation of SMD (μm)

$d_{p0} = 105 \mu\text{m}$		$d_{p0} = 180 \mu\text{m}$	
r/x	SMD	r/x	SMD
<u>$x/d = 50$</u>			
0.00	95.6	0.00	161.9
0.024	87.4	0.024	157.8
0.048	82.9	0.048	157.6
<u>$x/d = 100$</u>			
0.00	53.4	0.00	113.5
0.024	44.3	0.024	101.8
0.048	34.6	0.048	77.7

Table F.5.3 Drop-Size Distributions, $d_{p0} = 105 \mu\text{m}$

Range (μm)	Fraction	Range (μm)	Fraction	Range (μm)	Fraction
<u>$x/d = 50, r/x = 0.000$</u>		<u>$x/d = 50, r/x = 0.024$</u>		<u>$x/d = 50, r/x = 0.048$</u>	
66.6-74.9	0.0409	58.9-67.3	0.0962	51.5-60.1	0.0762
74.9-83.2	0.1170	67.3-75.7	0.1058	60.1-68.6	0.1333
83.2-91.5	0.1988	75.7-84.1	0.2212	68.6-77.2	0.2190
91.5-99.9	0.3216	84.1-92.5	0.2692	77.2-85.8	0.2667
99.9-108.2	0.3216	92.5-100.9	0.3079	85.8-94.4	0.1714
<u>$x/d = 100, r/x = 0.000$</u>		<u>$x/d = 100, r/x = 0.024$</u>		<u>$x/d = 100, r/x = 0.048$</u>	
9.2-18.3	0.0069	9.2-18.4	0.1377	0.0-9.3	0.0769
18.3-27.5	0.1310	18.4-27.6	0.1957	9.3-18.6	0.1978
27.5-36.6	0.2897	27.1-36.8	0.2319	18.6-27.9	0.3516
36.6-45.8	0.2690	36.8-46.0	0.2391	27.9-37.2	0.1868
45.8-54.9	0.1172	46.0-55.3	0.1304	37.2-46.5	0.1538
54.9-64.1	0.0621	55.3-64.5	0.0435	46.5-55.8	0.0330
64.1-73.2	0.0621	64.5-73.7	0.0217	--	--
73.2-82.4	0.0621	--	--	--	--
<u>$x/d = 70, r/x = 0.000$</u>		<u>$x/d = 130, r/x = 0.000$</u>			
26.5-35.3	0.0041	0-9.3	0.096		
35.3-44.1	0.0617	9.3-18.6	0.144		
44.1-52.9	0.1646	18.6-27.9	0.160		
52.9-61.8	0.1523	27.9-37.2	0.232		
61.8-70.6	0.1564	37.2-46.5	0.264		
70.6-79.4	0.1687	46.5-55.8	0.104		
79.4-88.2	0.1728	--	--		
88.2-97.1	0.1193	--	--		

Table F.5.4 Drop Size Distributions, $d_{p0} = 180 \mu\text{m}$

Range (μm)	Fraction	Range (μm)	Fraction	Range (μm)	Fraction
<u>$x/d = 50, r/x = 0.000$</u>		<u>$x/d = 50, r/x = 0.024$</u>		<u>$x/d = 50, r/x = 0.048$</u>	
135.0-143.2	0.0413	126.6-135.0	0.0155	128.1-136.6	0.0579
143.4-151.9	0.1157	135.0-143.4	0.1395	136.6-145.1	0.1405
151.9-160.3	0.2149	143.4-151.9	0.1938	145.1-153.7	0.2149
160.3-168.7	0.4793	151.9-160.3	0.2481	153.7-162.2	0.2397
168.7-177.2	0.1488	160.3-168.7	0.2636	162.2-170.7	0.2645
--	--	168.7-177.2	0.1395	170.7-179.3	0.0826
<u>$x/d = 100, r/x = 0.000$</u>		<u>$x/d = 100, r/x = 0.024$</u>		<u>$x/d = 100, r/x = 0.048$</u>	
78.9-87.7	0.0504	44.0-52.8	0.0494	17.9-26.8	0.0505
87.7-96.4	0.1513	52.6-61.6	0.0617	26.8-35.8	0.0707
96.4-105.2	0.1849	61.6-70.4	0.0247	35.8-44.7	0.0606
105.2-114.0	0.2101	70.4-79.2	0.0988	44.7-53.6	0.0707
114.0-122.7	0.2269	79.2-87.9	0.1358	53.6-62.6	0.1414
122.7-131.5	0.1092	87.9-96.7	0.2346	62.6-71.5	0.2020
131.5-140.3	0.0504	96.7-105.5	0.1235	71.5-80.4	0.1818
140.3-149.0	0.0168	105.5-114.3	0.1235	80.4-89.4	0.0909
--	--	114.3-123.1	0.0494	89.4-98.3	0.0707
--	--	123.1-131.9	0.0741	98.3-107.3	0.0404
--	--	131.9-140.7	0.0247	107.3-116.2	0.0202
<u>$x/d = 70, r/x = 0.000$</u>		<u>$x/d = 130, r/x = 0.000$</u>			
94.4-103.0	0.0081	9.1-18.3	0.0316		
103.0-111.5	0.0484	18.3-27.5	0.0526		
111.5-120.1	0.0645	27.5-36.6	0.0737		
120.1-128.7	0.1210	36.6-45.8	0.0842		
128.7-137.3	0.2500	45.8-54.9	0.1684		
137.3-145.9	0.3145	54.9-64.1	0.1263		
145.9-154.4	0.1452	64.1-73.2	0.2316		
154.4-163.0	0.0484	73.2-84.2	0.1474		
--	--	84.2-91.5	0.0316		
--	--	91.5-100.7	0.0526		

REFERENCES

1. Faeth, G. M., "Evaporation and Combustion of Sprays," Prog. in Energy and Combust. Sci., Vol. 9, 1983, pp. 1-76.
2. Faeth, G. M., "Recent Advances in Modeling Particle Transport Properties and Dispersion in Turbulent Flow," Proceedings of the ASME-JSME Thermal Engineering Conference, Vol. 2, ASME, New York, 1983, pp. 517-534.
3. Shuen, J-S., Chen, L-D. and Faeth, G. M., "Evaluation of a Stochastic Model of Particle Dispersion in a Turbulent Round Jet," AICHE J., Vol. 29, 1983, pp. 167-170.
4. Shuen, J-S., Chen, L-D. and Faeth, G. M., "Predictions of the Structure of Turbulent Particle-Laden Jets," AIAA J., Vol. 21, 1983, pp. 1483-1484.
5. Shuen, J-S., Chen, L-D. and Faeth, G. M., "Predictions of the Structure of Turbulent, Particle-Laden, Round Jets," AIAA Paper No. 83-0066, 1983.
6. Shuen, J-S., Solomon, A.S.P., Zhang, Q-F. and Faeth, G. M., "Structure of Particle-Laden Jets: Measurements and Predictions," AIAA Paper No. 84-0038, 1984; also AIAA J., in press.
7. Zhang, Q-F., Shuen, J-S., Solomon, A.S.P. and Faeth, G. M., "Structure of Ducted Particle-Laden Turbulent Jets," AIAA J., in press.
8. Solomon, A.S.P., Shuen, J-S., Zhang, Q-F. and Faeth, G. M., "Measurements and Predictions for Nonevaporating Sprays in a Quiescent Environment," AIAA Paper No. 83-0151, 1983.
9. Solomon, A.S.P., Shuen, J-S., Zhang, Q-F. and Faeth, G. M., "Structure of Nonevaporating Sprays: Measurements and Predictions," AIAA Paper No. 84-0125, 1984.
10. Solomon, A.S.P., Shuen, J-S., Zhang, Q-F. and Faeth, G. M., "Structure of Nonevaporating Sprays: I. Near-Injector Conditions and Mean Properties," AIAA J., in press.
11. Solomon, A.S.P., Shuen, J-S., Zhang, Q-F. and Faeth, G. M., "Structure of Nonevaporating Sprays: II. Drop and Turbulence Properties," AIAA J., in press.
12. Solomon, A.S.P., Shuen, J-S., Zhang, Q-F. and Faeth, G. M., "Measurements and Predictions of the Structure of Evaporating Sprays," 22nd ASME/AICHE National Heat Transfer Conference, Niagara Falls, NY, 1984; also, J. Heat Transfer, in press.
13. Shuen, J-S., Solomon, A.S.P. and Faeth, G. M., "Drop-Turbulence Interactions in a Diffusion Flame," AIAA Paper No. 85-0319, 1985.

14. Shuen, J-S., Solomon, A.S.P., Zhang, Q-F. and Faeth, G. M., "The Structure of Particle-Laden Jets and Nonevaporating Sprays," NASA CR-168059, 1983.
15. Shuen, J-S., Solomon, A.S.P., Zhang, Q-F. and Faeth, G. M., "A Theoretical and Experimental Study of Turbulent Particle-Laden Jets," NASA CR-168293, 1983.
16. Solomon, A.S.P., Shuen, J-S., Zhang, Q-F. and Faeth, G. M., "A Theoretical and Experimental Study of Turbulent Nonevaporating Sprays," NASA CR-174668, 1984.
17. Solomon, A.S.P., Shuen, J-S., Zhang, Q-F. and Faeth, G. M., "A Theoretical and Experimental Study of Turbulent Evaporating Sprays," NASA CR-174760, 1984.
18. Shuen, J-S., "A Theoretical and Experimental Investigation of Dilute Particle-Laden Turbulent Gas Jets," Ph.D. Thesis, The Pennsylvania State University, University Park, PA, 1984.
19. Solomon, A.S.P., "A Theoretical and Experimental Investigation of Turbulent Sprays," Ph.D. Thesis, The Pennsylvania State University, University Park, PA, 1984.
20. Jeng, S-M., "An Investigation of Structure and Radiation Properties of Turbulent Buoyant Diffusion Flames," Ph.D. Thesis, The Pennsylvania State University, University Park, PA, 1984.
21. Jeng, S-M., Chen, L-D. and Faeth, G. M., "The Structure of Buoyant Methane and Propane Diffusion Flames," Nineteenth Symposium (International) on Combustion, The Combustion Institute, Pittsburgh, 1982, pp. 1077-1085.
22. Jeng, S-M. and Faeth, G. M., "Species Concentrations and Turbulence Properties in Buoyant Methane Diffusion Flames," J. Heat Trans., in press.
23. Gosman, A. D. and Ioannides, E., "Aspects of Computer Simulation of Liquid-Fueled Combustors," AIAA Paper No. 81-0323, 1981.
24. Smith, R. H. and Wang, C-T., "Contracting Cones Giving Uniform Throat Speeds," J. Aero. Sci., Vol. 11, 1944, pp. 356-360.
25. Glass, M. and Kennedy, I. M., "An Improved Seeding Method for High-Temperature Laser Doppler Velocimetry," Comb. Flame, Vol. 29, 1977, pp. 333-335.
26. Shearer, A. J., Tamura, H. and Faeth, G. M., "Evaluation of a Locally Homogeneous Flow Model of Spray Evaporation," J. of Energy, Vol. 3, September-October 1979, pp. 271-278.

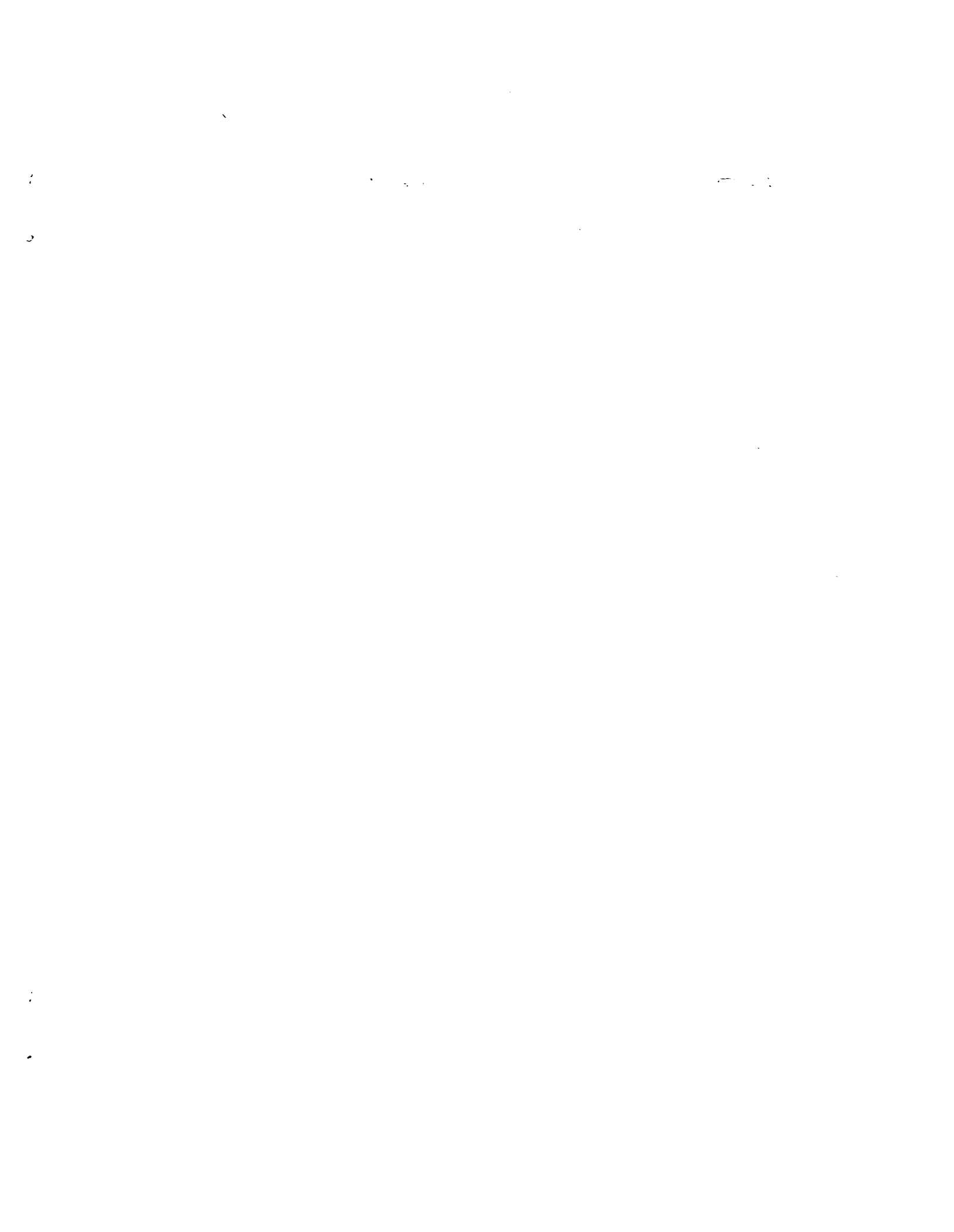
27. May, K. R., "The Measurement of Airborne Droplets by the Magnesium Oxide Method," J. Sci. Inst., Vol. 27, 1950, pp. 128-130.
- 28., Ranz, W. F., "Principles of Inertial Impaction," Engineering Research Bulletin, B-66, The Pennsylvania State University, University Park, PA, 1956.
29. Lockwood, F. C. and Naguib, A. S., "The Prediction of the Fluctuations in the Properties of Free, Round Jet, Turbulent, Diffusion Flames," Comb. Flame, Vol. 24, 1975, pp. 109-124.
30. Bilger, R. W., "Turbulent Jet Diffusion Flames," Prog. Energy Combust. Sci., Vol. 1, pp. 87-109, 1976.
31. Bilger, R. W., "Reaction Rates in Diffusion Flames," Comb. Flame, Vol. 30, 1977, pp. 277-284.
32. Liew, S. K., Bray, K.N.C. and Moss, J. B., "A Flamelet Model of Turbulent Non-Premixed Combustion," Comb. Sci. Tech., Vol. 27, 1981, pp. 69-73.
33. Jeng, S-M. and Faeth, G. M., "Scalar Properties in Turbulent Propane Diffusion Flames," J. Heat Trans., in press.
34. Mao, C-P., Szekely, G. A., Jr. and Faeth, G. M., "Evaluation of a Locally Homogeneous Flow Model of Spray Combustion," J. of Energy, Vol. 4, March-April 1980, pp. 78-87.
35. Mao, C-P., Wakamatsu, Y. and Faeth, G. M., "A Simplified Model of High Pressure Spray Combustion," Eighteenth Symposium (International) on Combustion, The Combustion Institute, Pittsburgh, 1981, pp. 337-347.
36. Gordon, S. and McBride, B. J., "Computer Program for Calculation of Complex Chemical Equilibrium Compositions, Rocket Performance, Incident and Reflected Shocks, and Chapman-Gouget Detonations, NASA SP-273, 1971.
37. Jeng, S-M., Lai, M-C. and Faeth, G. M., "Nonluminous Radiation in Turbulent Buoyant Axisymmetric Flames," Comb. Sci. Tech., in press.
38. Jeng, S-M. and Faeth, G. M., "Radiative Heat Fluxes Near Turbulent Buoyant Methane Diffusion Flames," J. Heat Transfer, in press.
39. Tsuji, H. and Yamaoka, I., "The Counterflow Diffusion Flames in the Forward Stagnation Region of a Porous Cylinder," Eleventh Symposium (International) on Combustion, The Combustion Institute, Pittsburgh, pp. 970-984, 1967.
40. Tsuji, H. and Yamaoka, I., "The Structure of Counterflow Diffusion Flames in the Forward Stagnation Region of a Porous Cylinder,"

Twelfth Symposium (International) on Combustion, The Combustion Institute, Pittsburgh, pp. 997-1005, 1969.

41. Tsuji, H. and Yamaoka, F., "Structure Analysis of Counterflow Diffusion Flames in the Forward Stagnation Region of a Porous Cylinder," Thirteenth Symposium (International) on Combustion, The Combustion Institute, Pittsburgh, 1971, pp. 723-731.
42. Mitchell, R. E., Sarofim, A. F. and Clomberg, L. A., "Experimental and Numerical Investigation of Confined Laminar Diffusion Flames," Combustion and Flame, Vol. 37, pp. 227-244, 1980.
43. Lai, M-C., Jeng, S-M. and Faeth, G. M., "Turbulent Wall Flows and Flames," Annual Report under USDC Grant NB81NADA2044, The Pennsylvania State University, University Park, PA, 1984.
44. Spalding, D. B., GENMIX: A General Computer Program for Two-Dimensional Parabolic Phenomena, Pergamon Press, Oxford, 1978.
45. Szekely, G. A., Jr. and Faeth, G. M., "Effects of Envelope Flames on Drop Gasification Rates in Turbulent Diffusion Flames," Comb. Flame, Vol. 11, pp. 255-259, 1983.
46. Drake, M. C., Bilger, R. W. and Stårner, S. H., "Raman Measurements and Conserved Scalar Modeling in Turbulent Diffusion Flames," Nineteenth Symposium (International) on Combustion, The Combustion Institute, Pittsburgh, pp. 459-467, 1982.
47. Hinze, J. O., Turbulence, Second Edition, McGraw-Hill, New York, pp. 520-558, 1975.
48. Durst, F., Melling, A. and Whitelaw, J. H., Principles and Practice of Laser-Doppler Anemometry, Academic Press, London, 1976.
49. Kreid, D. K., "Laser-Doppler Velocimeter Measurements in Nonuniform Flow: Error Estimates," Applied Optics, Vol. 13, pp. 1872-1881, 1974.
50. Moffat, R. J., "Contributions to the Theory of Single-Sample Uncertainty Analysis," J. Fluids Engrg., Vol. 104, pp. 250-258, 1982.
51. Caldwell, F. R., "Thermocouple Material," Temperature, Its Measurement and Control in Science and Industry, (C. M. Herzfield, ed.), Vol. 3, Part 2, Reinhold, New York, pp. 81-134, 1962.
52. Becker, H. A. and Yamazaki, S., "Entrainment, Momentum Flux and Temperature in Vertical Free Turbulent Diffusion Flames," Comb. Flame, Vol. 33, pp. 123-148, 1976.
53. Rohsenow, W. M. and Hartnett, J. P., Handbook of Heat Transfer, McGraw-Hill, New York, 1973.

54. Reid, R. C., Prausnitz, J. M. and Sherwood, T. K., The Properties of Gases and Liquids, Third Edition, McGraw-Hill, New York, 1977.
55. Svehla, R. A., "Estimated Viscosities and Thermal Conductivities of Gases at High Temperatures," NASA Technical Report R-132, 1962.
56. Anon., Technical Data Book--Petroleum Refining, Third Edition, American Petroleum Institute, Washington, DC, 1976.
57. Wark, K., Thermodynamics, 3ed., McGraw-Hill Book Co., New York, pp. 833-834, 1977.
58. Szekely, G. A., Jr., "Experimental Evaluation of a Carbon Slurry Droplet Combustion Model," Ph.D. Thesis, The Pennsylvania State University, University Park, PA, 1982.

1. Report No. NASA CR-174838		2. Government Accession No.		3. Recipient's Catalog No.	
4. Title and Subtitle The Structure of Dilute Combusting Sprays				5. Report Date January 1985	
				6. Performing Organization Code	
7. Author(s) J-S. Shuen, A.S.P. Solomon, and G.M. Faeth				8. Performing Organization Report No. None	
				10. Work Unit No.	
9. Performing Organization Name and Address The Pennsylvania State University Mechanical Engineering Building University Park, Pennsylvania 16802				11. Contract or Grant No. NAG 3-190	
				13. Type of Report and Period Covered Contractor Report	
12. Sponsoring Agency Name and Address National Aeronautics and Space Administration Washington, D.C. 20546				14. Sponsoring Agency Code 505-31-42	
15. Supplementary Notes Final report. Project Manager, Robert R. Tacina, Altitude Wind Tunnel Project Office, NASA Lewis Research Center, Cleveland, Ohio 44135.					
16. Abstract An experimental and theoretical study of drop processes in a turbulent flame is described. The experiments involved a monodisperse (105 and 180 μm initial diameter) stream of methanol drops injected at the base of a turbulent methane-fueled diffusion flame burning in still air. The following measurements were made: mean and fluctuating phase velocities, mean drop number flux, drop-size distributions and mean gas-phase temperatures. Measurements were compared with predictions of two separated flow models: (1) deterministic separated flow, where drop-turbulence interactions are ignored; and (2) stochastic separated flow, where drop-turbulence interactions are considered using random-walk computations. The stochastic separated flow analysis yielded best agreement with measurements, since it provides for turbulent dispersion of drops which was important for present test conditions (and probably for most combusting sprays as well). Distinguishing the presence or absence of envelope flames around the drops, however, was relatively unimportant for present test conditions, since the drops spent most of their lifetime in fuel-rich regions of the flow where this distinction is irrelevant.					
17. Key Words (Suggested by Author(s)) Spray modeling Turbulence interactions Combustor			18. Distribution Statement Unclassified - unlimited STAR Category 07		
19. Security Classif. (of this report) Unclassified		20. Security Classif. (of this page) Unclassified		21. No. of pages 122	22. Price* A06



National Aeronautics and
Space Administration

Washington, D.C.
20546

Official Business

Penalty for Private Use, \$300

SPECIAL FOURTH CLASS MAIL
BOOK



3 1176 00188 6192

NASA-451



NASA

POSTMASTER: If Undeliverable (Section 158
Postal Manual) Do Not Return
